DEVELOPMENT OF ELECTROPHYSIOLOGY CHARACTERIZATION TOOLS FOR LIPID MEMBRANES

By

JOYCE EL BEYROUTHY

(Under the Direction of Eric Freeman)

ABSTRACT

Droplet interface bilayers (DIBs) are stabilized water-in-oil emulsions developed as a simplified replica of cellular membranes. They represent the primary architecture of these biological systems: a double layer of phospholipids. Phospholipids are amphiphilic molecules, where their hydrophobic fatty acid chains are electrically insulating compared to their hydrophilic headgroups holding electrical charges. This profile facilitates their self-assembly property forming a lipid monolayer at a polar-nonpolar interface and defining its electrostatic properties. For DIBs, these monolayers are formed on the surrounding surface of aqueous droplets in an oil reservoir. The lipid membrane is then formed at the adhered interface of two lipid-coated droplets.

DIBs equilibrium is described by the balance of surface tensions and membrane electrophysiology. In fact, surface tension is a dominant force in emulsion systems and the balance between monolayer and membrane tensions governs the favorability of membrane formation influencing its size and activities. Furthermore, DIBs are semi-permeable

allowing for the variable and controllable formation of conductive pathways, whereas the difference in dielectric permittivity between the insulating hydrophobic inner region and the electrically charged outer surfaces leads to a capacitor-like behavior. Thus, DIBs are electrically analogous to a capacitor and a resistor in parallel. This well-established representation of lipid membranes is the basis for the electrical characterization techniques developed herein, while advantageously utilizing the complexity of DIB systems.

In this dissertation, novel membrane electrophysiology characterization techniques are developed and implemented based on these soft membranous systems. First, the effect of membrane electrocompression on lipids packing is investigated through advanced energy calculations. Then, tracking changes in cross-membrane electrostatics allows for the real-time characterization of nanoparticles surface interaction prior to membrane deterioration. Finally, an unprecedented multiphysics model simulates the response of networks of membranes under electrical manipulations. This dissertation re-enforces DIBs advantages in studying membrane mechanics, specifically through their coupled electrical-emulsion properties.

INDEX WORDS: Droplet interface bilayer, Electrophysiology, Electrical characterization, Membrane electrostatics, Membrane biophysics.

# DEVELOPMENT OF ELECTROPHYSIOLOGY CHARACTERIZATION TOOLS FOR LIPID MEMBRANES

by

JOYCE EL BEYROUTHY

B.E., Lebanese American University, Lebanon, 2016

M.S., The University of Georgia, 2018

A Dissertation Submitted to The Graduate Faculty of The University of Georgia in Partial Fulfilment of The Requirements of The Degree

DOCTOR OF PHILOSOPHY

ATHENS, GA

2022

DEVELOPEMNT OF ELECTROPHYSIOLOGY CHARACTERIZATION TOOLS

FOR LIPID MEMBRANES

by

JOYCE EL BEYROUTHY

Major Professor: Eric Freeman

Committee: Donald Leo

Leidong Mao

Hitesh Handa

Electronic Version Approved:

Ron Walcott

Dean of the Graduate School

The University of Georgia

May 2022

# DEDICATION

To my husband Blake, for teaching me to believe in myself and to celebrate the little moments in life. To my sister Jessica, for showing me that women can have it all. To my dad Bernard, for being my example in discipline and hard work. To my mom Sylva, for teaching me kindness and strength. To my brother-in-law Johnny, for showing me that with patience and persistence no problem can't be solved.

ACKOWLEDGEMENTS

First and foremost, thank you Dr. Eric Freeman for your guidance, support, and patience. This journey would not have happened if you didn’t take a chance on me and guided me through it. Thank you for being cheerful during successful times and thank you for being supportive and optimistic during low times. I am very grateful I had you as my advisor.

I would also like to thank my committee membranes, Dean Leo, Prof, Mao and Prof. Handa, thank you for your constant support and guidance. Our discussions turned simple ideas into meaningful and impactful projects.

TABLE OF CONTENT

Page

LIST OF TABLES

Page

LIST OF FIGURES

Page

forming molecule–peptides, polymers, or others–integrates across the membrane leaflets, ions transporting channels are created and the gross membrane conductance is increased. This can be detected by applying a constant DC voltage and monitoring the membrane-generated current. (c) Adopted from *"Makhoul-Mansour, M.M., et al., Photopolymerized microdomains in both lipid leaflets establish diffusive transport pathways across biomimetic membranes. Soft matter, 2019. 15(43): p. 8718-8727".* Example of current behavior upon increase in membrane conductance. Conductance here is induced by the presence of channel-forming photopolymerizable phospholipids in DIBs generating defects in the membrane .....37

**Figure 2. 9:** (a) With zero intramembrane electric field, the membrane is at its relaxed state with an initial geometry suitable for the system's equilibrium. (b) When an electrical field is applied, the membrane undergoes electrocompression-reduction in thickness due to attractive coulomb forces and if the setup allows electrowetting-increase in membrane area due to a reduction in surface tension. (c) Reproduced from *"Gross, L.C., et al., Determining membrane capacitance by dynamic control of droplet interface bilayer area. Langmuir, 2011. 27(23): p. 14335-42."* Specific capacitance and thickness of membranes composed of the same phospholipids, but with varying alkane chain length shows the solvent effect on membrane properties. (d) Reproduced from *"El-Beyrouthy, J., et al., A new approach for investigating the response of lipid membranes to electrocompression by coupling droplet mechanics and membrane biophysics. Journal of the Royal Society Interface, 2019. 16(161): p. 20190652".* Specific capacitance with respect to voltage for different solvents showing the latter's effect on the membrane's elasticity. (e) Adapted from *"El-Beyrouthy, J., et al., A new approach for investigating the response of lipid membranes to*

# CHAPTER 1

# INTRODUCTION

Cell membranes are protective barriers embracing the cellular organisms, separating the intracellular components from the extracellular environment and controlling cytoplasmic exchanges [1]. Thus, this semi-permeable envelop defines critical cellular properties and leads various cytoplasmic activities [2]. Since membranes define the physical boundaries of cellular organisms, they also dictate overall tissue properties and facilitate cell-to-cell communication [2, 3], mainly through exoplasmic receptors and across-membrane conductive channels [4]. Thus, understanding the mechanics of the cell membrane is crucial for understanding living systems and maintaining their growth, while these understandings are also utilized in pharmaceutical advancements [5, 6], synthetic biology applications [7, 8], and the development of bio-inspired materials [9, 10].

The traditional description of the cell membrane abides to the fluid mosaic model [11, 12]. This model predicts that the cell membrane is primarily structured as a double layer of phospholipids, holding within its lipid sheets various sterols and proteins essential to the membrane functionalities. In addition, the model explains that these biomolecules freely rearrange and readjust their position within the membrane enabling fulfilment of its current activity. Based on this model, researchers adopted a simplified replica of the cell membrane utilized in studying its properties and mechanics in a controllable and adjustable environment. The model membrane is then a double layer of phospholipids mimicking the

primary architecture of its biological analogue [12-14]. This lipid bilayer is artificially formed by utilizing the self-assembly property of phospholipids [15, 16]. In fact, these charged molecules are amphiphilic and form organized lipid sheets in the presence of a hydrophilic-hydrophobic interface [10]. This supported the development of various membrane-forming methodologies over the last few decades [10]. The interest in characterizing model membranes is growing in popularity due to their unlimited advantages in understanding biological events [17-21], and applications in materials and bio-inspired engineering [22-26].

Electrophysiology is a popular and well-established concept utilized for lipid membrane characterization [27-31]. Fundamentally, it utilizes the membrane electrical representation and tracks changes in these properties under various stimuli translating them into membrane mechanics and biophysical understandings [10]. In fact, due to the amphiphilic and electrically charged nature of phospholipid molecules, lipid membranes are electrically modeled as a capacitor and a resistor in parallel [27, 32]. The membrane capacitance arises from the difference in dielectric permittivity between the inner and outer layers of the planar membrane, whereas its conductance mirrors the cross-membrane permeability. Additionally, the lipid bilayer possess localized electric fields defining the transmembrane potential distribution [27]. These properties are commonly intertwined with the specific model membrane formed and are studied to obtain lipid membrane structural and dynamic properties [10].

In this dissertation, the development and implementation of advanced membrane characterization tools are presented based on membrane electrophysiology. First, the model membrane utilized herein is the droplet interface bilayer, or the DIB [33-35]. This specific

model membrane is formed at the interface of two adhered aqueous droplets in an oil reservoir and is unique in its emulsive nature, adding additional layers to the membrane electrical representation [29, 36]. This dissertation deepens the understandings of the intertwined electrophysiology and emulsion system dynamics and utilizes them for advancements in membrane characterization techniques. In fact, direct correlations between droplet mechanics and membrane electrophysiology are utilized as fundamental building blocks for investigating membrane mechanical structure and biophysical activities.

The work showcased herein influences the field of model membranes through advancements in their electrophysiology characterization tools. This includes an improved DIB formation setup that allows for the simultaneous measurements of membrane electrical and surface energies. This allowed for the investigation of adjustments in lipids lateral arrangement under membrane electrocompression. Furthermore, real-time characterization of nanoparticles surface interaction leading and prior to membrane permeabilization are hidden in traditional electrophysiology but exposed herein. Lastly, this work includes the development of a new multiphysics model for membrane networks able to simulate their response under an electric signal while considering asymmetric configurations of the various membranes. Next, each chapter of this dissertation is briefly introduced via an illustrative abstract focusing on its objective and main outcomes.

**Illustrative abstract of Chapter 2**

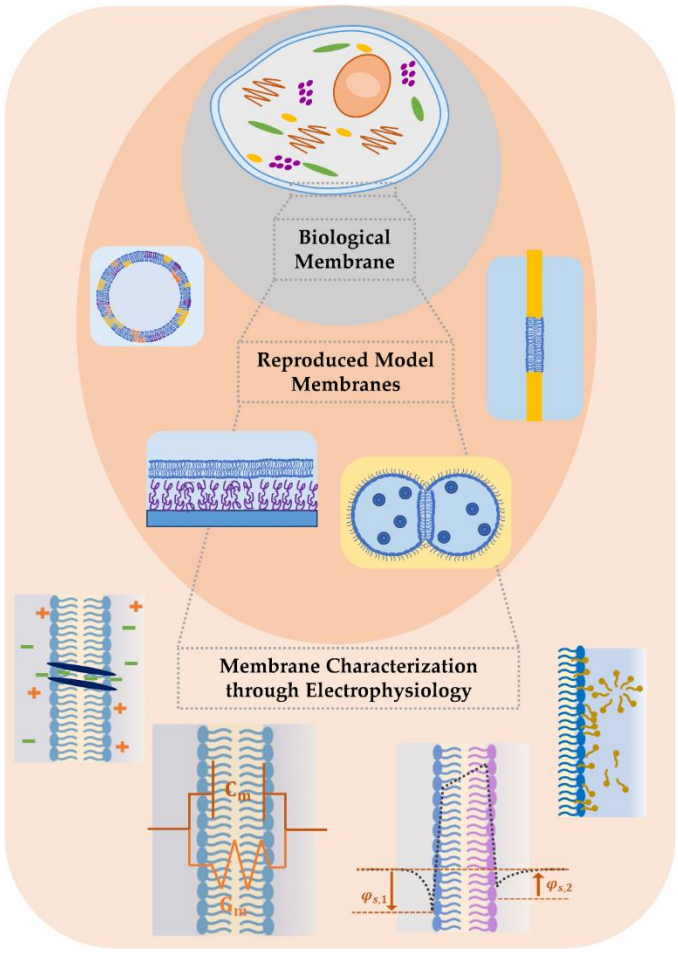


Figure 1. 1: Model membranes are double layers of phospholipids replicating the primary structure of biological membranes in an adjustable format. The self-assembly property of phospholipids drives them to form lipid sheets at a hydrophobic-hydrophilic interface. This property is the foundation of various model membrane forming methodologies. Upon formation, each membrane possesses specific properties and constraints guiding its electrophysiology characterization. The literature investigates the lipid membrane electrical representation and presents various tools for the studies of membrane-protein interactions, membrane equilibrium structure and dynamic mechanics and other phenomena of interest [10].

Chapter 2 presents a fully comprehensive literature review detailing the various methodologies for model membrane formation. Each methodology for reproducing lipid bilayers leads to different membrane electrical properties and constraints, which are highlighted in this chapter. The second part of the chapter focuses on describing well-

established electrophysiology understandings utilized to characterize model membranes. The highlight of this comprehensive review relies on linking the end properties and constraints of each model membrane to the unique advantages or limitations it provides for each characterization technique, as illustrated in Figure 1. 1. This review summarizes the highlights of membrane electrophysiology for the past decades and may be utilized as a comparison tool for newly developed concepts.

**Illustrative abstract of Chapter 3**

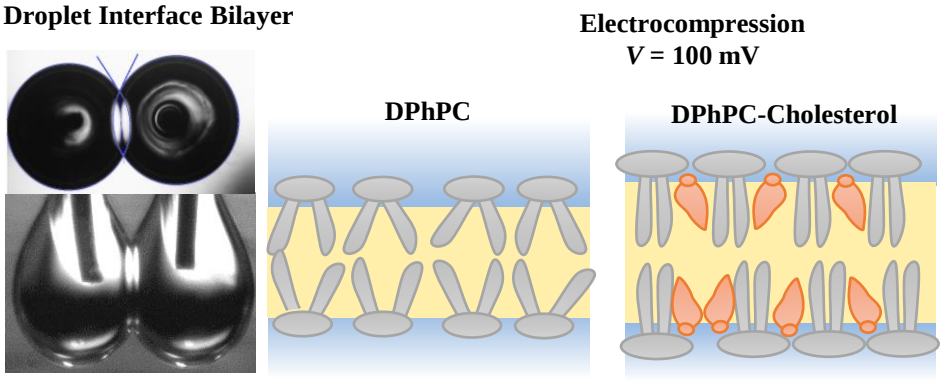


Figure 1. 2: Examining the bottom and side view of the droplet interface bilayer leads to simultaneous measurements of the membrane electrical and surface tension forces. Tracking the changes in these two energy terms under a changing electric field for various lipid frustrations allows for understanding transverse and lateral changes in lipid membranes under electrocompression [37].

Chapter 3 presents a new methodology for quantifying the effects of lipid frustration in model membranes under electrocompression by coupling droplet mechanics and membrane biophysics. This chapter demonstrates an advanced DIB characterization setup, allowing for the measurement of dynamic changes in membrane electrical and surface tension forces, through the simultaneous observation of droplets wetting area and contact angle, as seen in Figure 1. 2, previously considered a challenge. Membrane area measurement allows for dynamic calculations of the dielectric stress and the resulting

membrane thinning, whereas the droplets contact angle enables calculations of the membrane surface tension. Balancing these energies under an applied electric field leads to novel understandings of the lipids lateral structure under transverse electrocompression. In fact, membranes with varying lipid frustrations were utilized and the results highlight that an additional energy term is produced during membrane compression, reflecting changes in the lateral membrane structure, which inversely scales with the lipids packing and membrane rigidity.

**Illustrative abstract of Chapter 4**

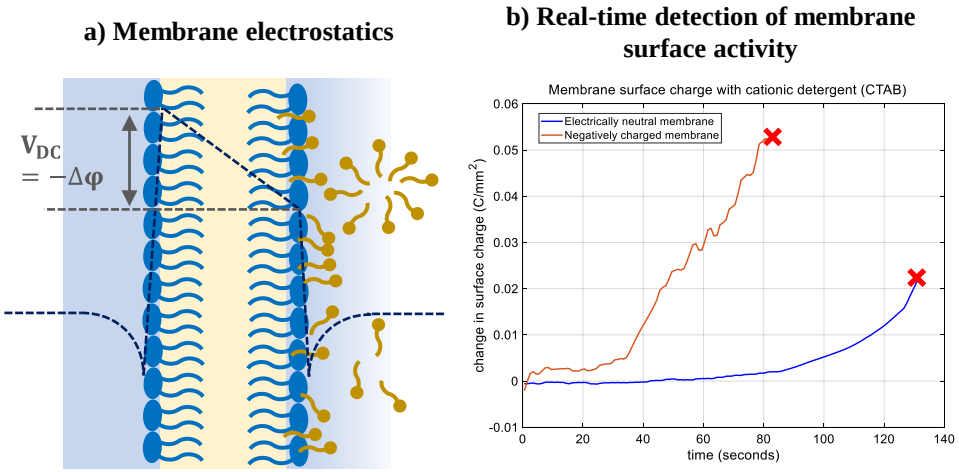


Figure 1. 3: a) Lipid membranes possess localized electric fields that dictate the cross-membrane potential profile. This profile is evenly distributed when both leaflets are symmetric in their structure. However, when an asymmetry occurs in between the leaflets, such as one-sided accumulation of a membrane-active nanoparticle, this distribution shifts leading to a membrane potential offset. b) Tracking changes in this offset allows for studying the mechanics of membrane permeabilization prior and leading to membrane disruption. This is made possible using DIB mechanoelectricity property and results include different detergent-driven solubilization mechanics for electrically neutral and anionic membranes.

Chapter 4 presents a novel membrane surface characterization technique based on the DIB's mechanoelectricity property [38]. DIB's fluidic nature allows for harmonic oscillations of membrane surface area through mechanical displacement of the droplets.

This leads to the generation of a mechanoelectric current, which is negligible until there is a composition mismatch between the membrane leaflets such as one-sided accumulation of membrane-active agents, as seen in Figure 1. 3 (a). The voltage needed to compensate for the generated current is then translated into changes in cross-membrane surface charge. A customized instrumentation and control system allow for real-time reading of this voltage and thus of nanoparticles surface interactions. In this work, the study of initial attachment and insertion mechanics are tracked in real-time prior to initial signals of membrane permeabilization, as seen in Figure 1. 3 (b). This further enhances the capabilities of traditional electrophysiology studies through utilizing the fluidic nature of DIB membranes.

**Illustrative abstract of Chapter 5**

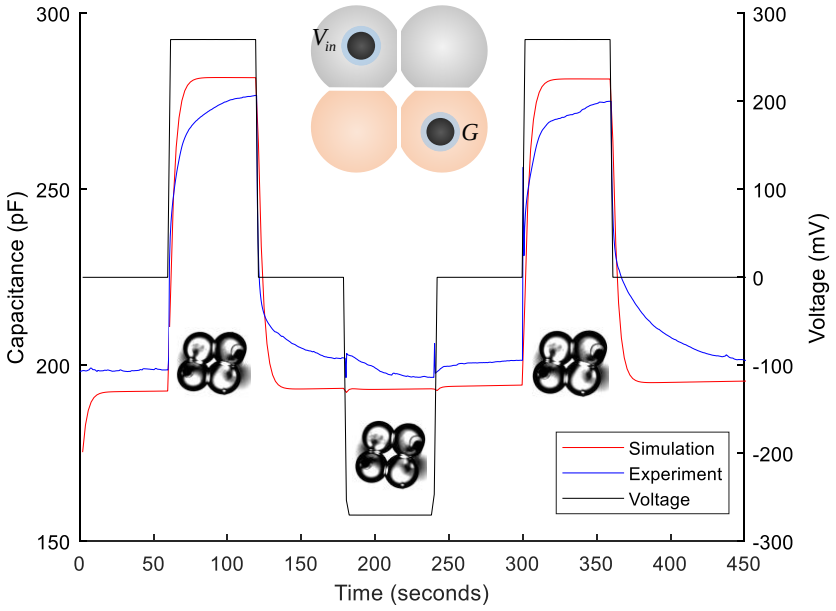


Figure 1. 4: Simulated and experimental behavior of a four-droplets asymmetric network under electrowetting. Asymmetric network is formed by having different phospholipids dispersed in different droplets. This leads to uneven distribution of the total electric field upon the application of a cross-network potential, allowing for directional compaction in

the network. Comparing the experimental results to those obtained from the model validates its accuracy.

Chapter 5 describes a new multiphysics model simulating the electrowetting response of DIB networks, highlighting the directional compaction in asymmetric networks. Electrowetting is the established response of a single DIB under electrical input. It relies on the minimization of the system's total energy considering surface tension and electrical stress. This concept is utilized and expanded to estimate the behavior of a network of DIBs, symmetric and asymmetric, in response to an applied electric field. This chapter explains the development of this multiphysics model, and the simulations are validated through experimental comparisons as seen in Figure 1. 4.

## References


1. Lodish, H. and A. Berk, *Molecular cell biology*. Vol. 3.
2. Grecco, H.E., M. Schmick, and P.I.J.C. Bastiaens, *Signaling from the living plasma membrane.* 2011. **144**(6): p. 897-909.
3. Levental, I., K. Levental, and K. Simons, *The Differentiation of the Plasma Membrane*. 2013, Federation of American Societies for Experimental Biology.
4. Nagasawa, H., et al., *Involvement of membrane signaling in the bystander effect in irradiated cells.* 2002. **62**(9): p. 2531-2534.
5. Sharma, A. and U.S. Sharma, *Liposomes in drug delivery: progress and limitations.* International journal of pharmaceutics, 1997. **154**(2): p. 123-140.
6. Landon, C.D., et al., *Nanoscale drug delivery and hyperthermia: the materials design and preclinical and clinical testing of low temperature-sensitive liposomes used in combination with mild hyperthermia in the treatment of local cancer.* The open nanomedicine journal, 2011. **3**: p. 38.
7. Kamiya, K.J.M., *Development of artificial cell models using microfluidic technology and synthetic biology*. 2020. **11**(6): p. 559.
8. Bhattacharya, A., et al., *A minimal biochemical route towards de novo formation of synthetic phospholipid membranes.* 2019. **10**(1): p. 1-8.
9. Tien, H.T. and A.J.E.A. Ottova, *Supported planar lipid bilayers (s-BLMs) as electrochemical biosensors.* 1998. **43**(23): p. 3587-3610.
10. El-Beyrouthy, J. and E. Freeman, *Characterizing the Structure and Interactions of Model Lipid Membranes Using Electrophysiology.* 2021. **11**(5): p. 319.
11. Singer, S.J. and G.L.J.S. Nicolson, *The fluid mosaic model of the structure of cell membranes.* 1972. **175**(4023): p. 720-731.
12. Jacobson, K., E.D. Sheets, and R.J.S. Simson, *Revisiting the fluid mosaic model of membranes.* 1995. **268**(5216): p. 1441-1443.
13. Fox, C.F.J.S.A., *The structure of cell membranes.* 1972. **226**(2): p. 30-39.
14. Mueller, P., et al., *Reconstitution of cell membrane structure in vitro and its transformation into an excitable system.* 1962. **194**(4832): p. 979-980.
15. Israelachvili, J.N., D.J. Mitchell, and B.W.J.B.e.B.A.-B. Ninham, *Theory of self-assembly of lipid bilayers and vesicles.* 1977. **470**(2): p. 185-201.
16. Salamon, Z., et al., *Assembly and molecular organization of self-assembled lipid bilayers on solid substrates monitored by surface plasmon resonance spectroscopy.* 1994. **1195**(2): p. 267-275.
17. Ding, B. and Z.J.T.j.o.p.c.B. Chen, *Molecular interactions between cell penetrating peptide Pep-1 and model cell membranes.* 2012. **116**(8): p. 2545-2552.
18. Soblosky, L., A. Ramamoorthy, and Z. Chen, *Membrane interaction of antimicrobial peptides using E. coli lipid extract as model bacterial cell membranes and SFG spectroscopy.* Chemistry and physics of lipids, 2015. **187**: p. 20-33.
19. Nezil, F.A. and M. Bloom, *Combined influence of cholesterol and synthetic amphiphillic peptides upon bilayer thickness in model membranes.* Biophysical journal, 1992. **61**(5): p. 1176-1183.
20. Clifton, L.A., et al., *Design and use of model membranes to study biomolecular interactions using complementary surface-sensitive techniques.* 2020. **277**: p. 102118.

21. Sekiya, Y., et al., *Electrophysiological analysis of membrane disruption by bombinin and its isomer using the lipid bilayer system.* 2019. **2**(4): p. 1542-1548.
22. Geng, J., et al., *Stochastic transport through carbon nanotubes in lipid bilayers and live cell membranes.* 2014. **514**(7524): p. 612-615.
23. Beltramo, P.J., R. Van Hooghten, and J. Vermant, *Millimeter-area, free standing, phospholipid bilayers.* Soft Matter, 2016. **12**(19): p. 4324-31.
24. Mansour, M.M.M., et al., *A skin-inspired soft material with directional mechanosensation.* 2021.
25. Bianco, A., K. Kostarelos, and M. Prato, *Applications of carbon nanotubes in drug delivery.* Current opinion in chemical biology, 2005. **9**(6): p. 674-679.
26. Corredor, C., et al., *Disruption of model cell membranes by carbon nanotubes.* 2013. **60**: p. 67-75.
27. Schoch, P., D.F. Sargent, and R. Schwyzer, *Capacitance and conductance as tools for the measurement of asymmetric surface potentials and energy barriers of lipid bilayer membranes.* The Journal of Membrane Biology, 1979. **46**(1): p. 71-89.
28. Alvarez, O. and R. Latorre, *Voltage-dependent capacitance in lipid bilayers made from monolayers.* Biophysical journal, 1978. **21**(1): p. 1-17.
29. Taylor, G.J., et al., *Direct in situ measurement of specific capacitance, monolayer tension, and bilayer tension in a droplet interface bilayer.* Soft Matter, 2015. **11**(38): p. 7592-605.
30. Taylor, G.J., et al., *Capacitive Detection of Low-Enthalpy, Higher-Order Phase Transitions in Synthetic and Natural Composition Lipid Membranes.* Langmuir, 2017. **33**(38): p. 10016-10026.
31. Taylor, G., et al., *Electrophysiological interrogation of asymmetric droplet interface bilayers reveals surface-bound alamethicin induces lipid flip-flop.* Biochimica et Biophysica Acta (BBA)-Biomembranes, 2018.
32. Goldman, D.E.J.T.J.o.g.p., *Potential, impedance, and rectification in membranes.* 1943. **27**(1): p. 37-60.
33. Bayley, H., et al., *Droplet interface bilayers.* Mol Biosyst, 2008. **4**(12): p. 1191-208.
34. Funakoshi, K., H. Suzuki, and S. Takeuchi, *Lipid bilayer formation by contacting monolayers in a microfluidic device for membrane protein analysis.* Analytical chemistry, 2006. **78**(24): p. 8169-8174.
35. Poulin, P. and J. Bibette, *Adhesion of water droplets in organic solvent.* Langmuir, 1998. **14**(22): p. 6341-6343.
36. Gross, L.C., et al., *Determining membrane capacitance by dynamic control of droplet interface bilayer area.* Langmuir, 2011. **27**(23): p. 14335-42.
37. El-Beyrouthy, J., et al., *A new approach for investigating the response of lipid membranes to electrocompression by coupling droplet mechanics and membrane biophysics.* Journal of the Royal Society Interface, 2019. **16**(161): p. 20190652.
38. El-Beyrouthy, J., et al., *Studying the Mechanics of Membrane Permeabilization through Mechanoelectricity.* 2022.

# CHAPTER 2

# CHARACTERIZING THE STRUCTURE AND INTERACTIONS OF MODEL LIPID MEMBRANES USING ELECTROPHYSIOLOGY [1]

[1] El-Beyrouthy, J., & Freeman, E. (2021). Characterizing the Structure and Interactions of Model Lipid Membranes Using Electrophysiology. *Membranes*, *11*(5), 319.
Reprinted with permission of publisher.

## Abstract

The cell membrane is a protective barrier whose configuration determines the exchange both between intracellular and extracellular regions and within the cell itself. Consequently, characterizing membrane properties and interactions is essential for advancements in topics such as limiting nanoparticle cytotoxicity. Characterization is often accomplished by recreating model membranes that approximate the structure of cellular membranes in a controlled environment, formed using self-assembly principles. The selected method for membrane creation influences the properties of the membrane assembly, including their response to electric fields used for characterizing transmembrane exchanges. When these self-assembled model membranes are combined with electrophysiology, it is possible to exploit their non-physiological mechanics to enable additional measurements of membrane interactions and phenomena. This chapter reviews several common model membranes including liposomes, pore-spanning membranes, solid supported membranes, and emulsion-based membranes, emphasizing their varying structure due to the selected mode of production. Next, electrophysiology techniques that exploit these structures are discussed, including conductance measurements, electrowetting and electrocompression analysis, and electroimpedance spectroscopy. The focus of this review is linking each membrane assembly technique to the properties of the resulting membrane, discussing how these properties enable alternative electrophysiological approaches to measuring membrane characteristics and interactions.

## Introduction

Cell membranes are semi-permeable barriers surrounding cellular organisms, separating the intracellular components from the extracellular environment [1]. Since cell membranes provide the cellular architecture enabling the distinction between adjacent regions of the cell and intracellular compartmentalization, these lipid barriers are a fundamental scaffold for inter and intracellular communication and exchange [2]. Within individual cells, membranes permit for multiple molecular reactions to occur simultaneously via membrane compartmentalization [3, 4]. Within the membrane itself, multiple lipid domains coexist in different parts of the membrane, controlling various cellular activities [3]. These lipid domains undergo changes in phase separation and overall lipids packing essential to cell differentiation and proliferation [5]. Furthermore, membrane electrochemical properties are vital for the cell's functionality, such as the propagation of action potentials and maintaining intracellular compositions [6]. Since the membrane acts as a differentiating limit between the cytosol and the extracellular environment, it also governs cell-to-cell communication [2, 5]. External stimuli are detected by the membrane's corresponding receptors initiating complex molecular reactions through ion channels opening or closing depending on the reaction launched [7, 8]. Thus, the membrane is a key element in the life of individual cells as well as in tissue maintenance. Investigating its properties and dynamic behavior opens doors for advancements in pharmaceuticals [9, 10], synthetic biology [11, 12], and bioinspired materials [13, 14].

The cell membrane's primary structure is a double layer of phospholipids that holds within its leaflets varying components including the proteins, peptides and sterols necessary for its functionality [1]. Figure 2.1 shows a schematic of the shape and possible

structure of a generic cell membrane [15-18]. Each membrane or region within the membrane possesses a particular molecular combination that produces varying bulk properties. For example, drug-resistant cancer cells show a higher membrane bending rigidity in comparison to drug-sensitive cells [19, 20], and the negatively charged exoplasmic surface of gram-negative bacteria makes them an easier target for cationic antibacterial peptides [21, 22]. The two lipid leaflets forming the cellular envelope exhibit varying compositions. For example, cholesterol is more abundantly found in the inner leaflets of plasma membranes [23], whereas membranous domains, or lipid rafts, are mainly formed in the exoplasmic leaflets [24]**.** Cellular membranes rely on their asymmetry for stability, shape, permeability as well as membrane potential activities. The membrane asymmetry presents a constant state of non-equilibrium which is maintained by continuous active processes [25].

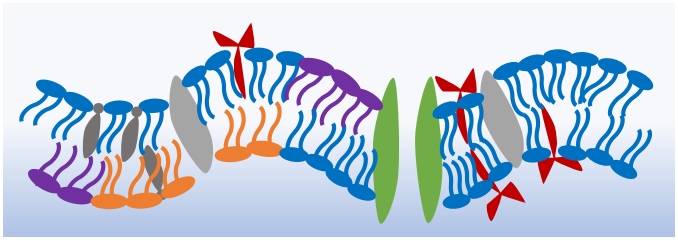

Figure 2.1: A schematic illustrating the complexity of natural cell membranes. The base structure of these barriers is a double layer of phospholipids. Transport proteins, sterols and other biomolecules are present in different parts of the membrane depending on the cell's role and life cycle stage.

Phospholipids are amphiphilic molecules possessing a hydrophilic headgroup and two hydrophobic fatty acid chains [26]. This amphiphilic structure enables their self-assembly whenever dispersed in a polar-apolar medium [27]. The middle layer of the cell membrane consists of the fatty acid chains bonding through hydrophobic forces, whereas the two outer layers are primarily the hydrophilic head groups. Since the membrane's

hydrophobic interior is near-impermeable to dissolved species within the aqueous phases, transmembrane exchange is primarily handled through embedded channels, and transport proteins contained within the membrane interior [1]. Furthermore, this middle layer provides an electric permittivity that is substantially lower than that of the outer hydrophilic regions leading to the traditional membrane's electrical representation: a capacitor in parallel with a resistor [28]. This analogy is the basis of electrical investigations of membrane structure, dynamics and nanoparticle interactions.

One technique for characterizing the electrical properties of the cell is the patch-clamp technique [29], where an electrode-pipette comes in direct contact with an isolated cell bathed into an electrolyte solution mimicking its physiological environment [30, 31]. Silver-silver/chloride (Ag/Ag-Cl) electrodes connected to a patch clamp amplifier allow for either a clamped voltage or current, measuring the membrane response and producing current-voltage relationships for further study. The produced electric field here falls primarily across the membrane interior through the separation of charged ions, mimicking membrane potentials within the body. Individual patches of the membrane can be isolated by adjusting the position of the electrode. However, this technique requires precise positioning and presents unique challenges due to the complex and delicate structure of the cells. In addition, studying the intertwined membrane components within a single patch or entity of a complex natural membrane often prevents the ready isolation of the desired agent-membrane interactions. Thus, to elucidate the components of a certain mechanism, one needs to recreate the lipid membrane in a more controlled laboratory environment, commonly achieved through creating synthetic, or model, membranes. Model membranes are synthetic double layers of phospholipids mimicking the core structure of the biological

membrane. They present a tailorable model platform for simulating cellular environments and allow for a better control over simulated external conditions.

In the last decade, multiple reviews discussing different model membrane formation techniques combined with electrophysiological characterizations have been published. Siontorou et al. presented the advancements in model membrane platforms, suspended and supported, while focusing on their applications in biosensing and characterization [32]. Khan et al. described various membrane-protein mechanics based on electroimpedance studies for solid supported model membranes and pore-spanning membranes [33]. Similarly, Grewer et al. compared protein transport in artificial lipid membranes to natural cell membranes focusing on the patch-clamp technique [30]. Nanomaterials and nanoparticles interactions at the membrane level were also discussed by Wu and Jiang [34], and Rascol et al. [35], respectively, while not limiting the characterization techniques to electrophysiological approaches. The review presented here instead focuses on some of the most relevant and recent electrophysiological approaches for investigating membrane structure and interactions, highlighting in particular how the selected method for membrane formation influences the available methods for characterization.

First, four of the most common model membranes are presented along with their properties and experimental artefacts resulting from their mode of production: lipid vesicles or liposomes formed in aqueous solutions or microfluidic channels, pore-spanning membranes formed at the orifice of a hydrophobic wall, solid supported membranes formed at the surface of a hydrophilic support; droplet on hydrogel bilayer, and droplet interface bilayer. Next, three major concepts of membrane electrophysiology are explained along

with the membrane characteristics they underline: conductance measurements, electrowetting-electrocompression analysis, and electroimpedance spectroscopy. Throughout this discussion, we focus on linking these electrophysiology approaches to the model membrane properties and constraints, while highlighting how the membrane structure and interactions may be assessed.

## Model membranes: manufactures and resulting properties

Model membranes reproduce the fundamental structure of cellular membranes: a double layer of phospholipids. Each model membrane platform is unique and leads to a different environment for studying membrane structures and interactions. This section presents four of the most common model membranes, explains their formation process, and discusses their resulting properties and how these properties may influence measurements of membranous phenomena.

### Liposomes

Liposomes, also called lipid vesicles, are one of the earliest forms of synthetic membranes [36]. As shown in Figure 2.2, they are spherical lipid bilayers formed in an aqueous environment, commonly through electroformation [37-39], phase transfer [40-42] or microfluidic jets [43, 44]. Liposomes may be formed in different sizes and distributions [45], but giant unilamellar vesicles (GUVs) are often employed as they are comparable in size and shape to living cells [44]. GUVs may be formed using electroformation [37], where a volatile solvent, such as chloroform or methanol, containing the desired lipids is placed on a conductive surface–commonly an indium tin oxide (ITO) slide–followed by an overnight evaporation to form dry lipid films. These dry films are then rehydrated with sucrose solution and the vesicles are formed by applying an AC voltage across the

conductive surface, where the voltage frequency and amplitude are tuned to reach the desired liposome size. In phase transfer [40], an aqueous droplet, submerged in a lipid-dispersed oil medium is coated with these lipids through their amphiphilic-driven self-assembly. The coated droplet is then added onto a separate water-oil lipid monolayer. The difference in salt concentrations between the water droplet and the secondary aqueous solution drives the droplet into the planar lipid sheet forming a spherical double layer or, a liposome. Elani et al. showed that this approach enables the formation of adjacent compartments mimicking compartmentalization observed in living cells [46]. Furthermore, they successfully formed and mechanically investigated asymmetric liposomes [47] as well as thermally controllable lipid vesicles [48]. Authors noted residual solvent in between the leaflets when created using phase transfer. However, this was not an issue in the microfluidic jet technique, where a focused fluid flow is applied to a planar bilayer formed at a water-oil-water interface, generating multiple lipid vesicles [43, 44].

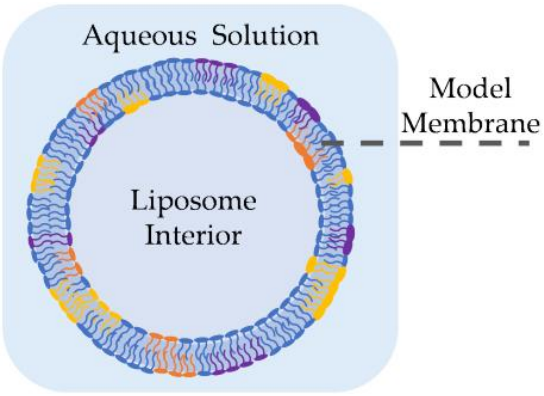


Figure 2.2: A cross-section of a liposome, or a lipid vesicle. Liposomes are model membranes recreating a lipid bilayer, while resembling cells in their shape and size, especially through giant unilamellar vesicles. Liposomes can be formed through electroformation, phase transfer or microfluidic jets.

Liposomes are commonly used to investigate membrane permeability through fluorescence [49] or radioactive tracking [50], in addition to permitting measurement of

some mechanical properties [47] such as membrane bending rigidity [51, 52]. The shape of liposomes resembles that of natural cell membranes in providing a closed, continuous membranous shell around their contents. This renders them a reliable platform for the study of nanoparticles-membrane interactions [53-55], especially nanoparticle uptake [56]. In addition, these lipid vesicles form the basic structure of multiple drug-delivery nanocarriers [9, 57, 58]. Encapsulating a certain drug, usually of a toxic or fragile nature, inside a closed membrane allows for its safe transport across the organism until it reaches its target destination [59, 60]. The transport and delivery of the drug is more effective, better controlled and safer through lipid-composition alternations and surface manipulations [61-63]. For example, thermosensitive liposomes, formed by mixture of low-temperature sensitive phospholipids, enable the localized release of toxins in the diseased area through temperature manipulation [64].

Liposomes are geometrically comparable to natural membranes allowing for studies of membrane mechanics [65-67], undulations [52], and surface interactions [68]. Furthermore, single-channel recordings of transmembrane activity in liposomes is possible by means of the patch-clamp technique [68]. However, since many electrical methods for liposome characterization involve placing the liposomes between two electrodes and supplying an external field rather than a localized field directly across the membrane itself, liposomes electrophysiological studies are primarily limited to single-channel patch-clamp measurements and are not a point of emphasis within the scope of this particular review article.

### Pore-spanning membranes

First introduced by Mueller et al., pore-spanning membranes, also referred to as black lipid membranes, are formed at the opening of a hydrophobic separator (or septum) between two aqueous baths [69, 70], as seen in Figure 2.3. These membranes were first created using the painting technique [69], where a membrane-forming solution would be spread across the orifice by means of a brush or a syringe. First, the solvent solution–commonly decane oil containing phospholipids–is brushed on both sides of the aperture. Due to the amphiphilic nature of the lipids, they self-assemble such that the hydrophilic heads are oriented towards the aqueous baths. Since the separator is hydrophobic, the solvent moves towards its surface, partially expelling itself from between the monolayers, forming the lipid membrane at the aperture between the two baths. Decane is often used as the solvent in this technique due to its high volatility and low viscosity compared to higher chain oils, enabling partial evaporation and easier relocation from between the monolayers, and thus a proper membrane formation [71]. Silver/silver-chloride (Ag/AgCl) electrodes are placed in the aqueous solutions on opposite sides of the membrane enabling electrophysiological measurements. Note that the painted membrane may contain excess residual solvent, as the short chain oil does not completely expel itself from between the lipid leaflets, leading to soft or highly elastic membranes [72, 73]. The amount of residual solvent within the membrane has been reduced by various efforts including coating the aperture with an amphiphobic agent [74], decreasing the control temperature to below the oil freezing point [75], and using longer chain solvents that are unable to distribute within the membrane interior [72, 76]. In addition, the formation of asymmetric membranes,

where the two leaflets are composed of different lipid combinations, requires additional layers of formation [77].

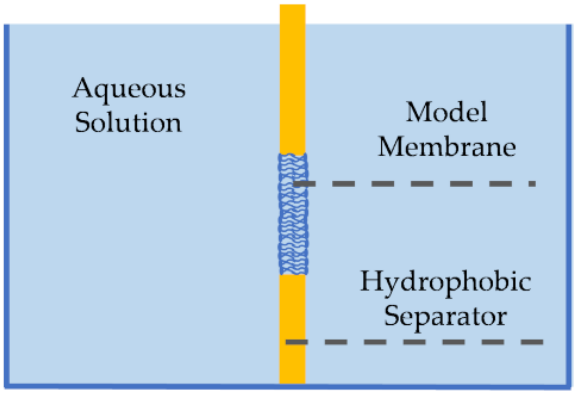


Figure 2.3: Pore-spanning membranes are planar lipid bilayers formed at the orifice of a hydrophobic separator between two aqueous solutions. The membrane can be achieved through the painting or folding approach. In the painting method, lipid-dispersed solvent is placed in the separator hole by painting it with a syringe or a brush. The bilayer is then formed through lipids self-orientation. In the folding method, the lipid monolayers are initially formed at the water-air interface while the orifice is higher than the water level. Then, pulling the hydrophobic separator downwards, the monolayers follow through hydrophobic bonding and the bilayer is formed in the orifice.

One decade later, Montal and Mueller introduced the folding approach for creating pore-spanning membranes, by folding two air-water lipid monolayers into the hydrophobic orifice [70]. In this technique, two lipid monolayers are first formed at the water-air interface separated by the solid septum. The two monolayers are formed by adding phospholipids-dispersed volatile solvents, such as chloroform or ethanol, on the surface of the aqueous solutions. The solvents then evaporate leaving the dry film at the water-air interface. The hydrophobic separator orifice, which is originally higher than the monolayers level, is slowly pulled downwards dragging the two monolayers along and forming the bilayer through hydrophobic affinity. The rate of displacement of the separator should be slower than the rate of monolayers bonding to ensure a successful membrane formation. Since there is no initial solvent residue, the folded membrane is solvent-free and

closer in thickness to that of living membranes. Additionally, asymmetric membranes can be directly formed through the folding technique by originally placing different phospholipids on the two aqueous surfaces [78, 79].

Recent pore-spanning membrane platforms involve lipid bilayers supported over multiple pores [80], as well as thin-film pressure balances, which are combined with electrophysiology for precise characterization of large area model biomembranes (LAMBs). These systems have been presented by Beltramo et al., providing control over membrane tension with varying solvents [72, 81] and demonstrating asymmetric membrane formation [82].

These modes for forming pore-spanning membranes lead to sealed and tightly-packed lipid bilayers with a high innate membrane impermeability, and thus a high electrical resistance [70, 83]. This high innate resistance rendered these membranes as ideal for studies on transmembrane exchange [70, 79, 84, 85]. Furthermore, the membrane area is geometrically constrained by the surrounding orifice limiting its ability to adjust in response to externally applied forces [69-71].

**Solid Supported Membranes**

Solid supported membranes (SSMs) are model membranes that are formed on a hydrophilic solid support in an aqueous medium, as illustrated in Figure 2.4 (a) [14, 33]. These have shown to be more robust and stable than previously developed model membranes owning their stability to the localized tight lipids packing and the solid supporting scaffold. Their robustness and stability lead to their popularity in molecular electronic microfluidic chips [14, 86, 87]. They were first introduced by Tamm and McConnell, where two water-air monolayers were deposited on a hydrophilic solid support

such as silicon, glass and quartz [88]. In this initial work, membranes were formed through the Langmuir-Blodgett and Langmuir Schaefer (LB/LS) technique, while others have later successfully formed these membranes through vesicle fusion or through a combination of both. In the LB/LS technique, the lipid monolayer is formed at a water-air interface through phospholipids self-assembly, then a hydrophilic aperture is displaced across while adhering the lipid sheets on its surface. The film is then placed horizontally on top of the other monolayer and pushed under the water level until deposited on the bottom of the reservoir. The second approach to forming SSMs is through vesicle fusion [89], where small unilamellar vesicles are formed and dispersed into the aqueous solution covering the hydrophilic substrate. Driven by hydrophilic favorability, the vesicles adsorb and unfold onto the hydrophilic surface, forming a planar lipid bilayer. The third approach is a combination of these two techniques, where the bottom lipids sheet is formed by means of the Langmuir-Blodgett monolayer and the top lipids sheet is formed through vesicles unfolding [90]. This combined approach is mostly used for the formation of asymmetric membranes–different lipids forming the two leaflets. The material of the hydrophilic support has been varied over the years, depending on the required membrane properties and the technique used to study the membrane. Commonly, silicon or mica are used in atomic force microscopy as they provide flat and smooth surfaces [91, 92], gold and silver are adopted during surface plasmon resonance technique [93-95], silica and borosilicate glass are used in optical-based techniques [96, 97], whereas Indium-Tin-Oxide (ITO) glass is the most suitable for electrophysiology studies due to its high electrical conductivity [98, 99].

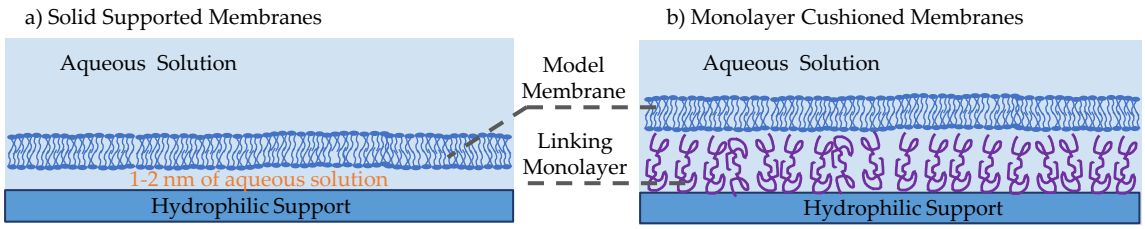


Figure 2.4: Model membranes are formed on a solid substrate in two configurations. (a) Solid supported membranes are formed at the planar surface of a hydrophilic solid support. The bilayer is formed through LB/LS method or vesicle fusion method or a combination of both. The resulting membrane is stable, mechanically robust and long-lasting as a result of localized tight lipids packing and the presence of the underneath solid support. (b) The introduction of a linking interstitial region between the solid support and the membrane leads to a larger aqueous environment beneath the membrane. This facilitates the introduction of proteins and larger biomolecules in a safe and unconstrained setting. The joining monolayer can be formed through a polymer, a protein, thiolipids or other amphiphilic molecules.

Solid supported membranes in their original form were not optimized for incorporating proteins and peptides. The resulting 1–2 nm aqueous layer between the membrane and the solid substrate [97, 100] is insufficient for these large molecules to freely move, and in most cases, they are exposed to the solid surface leading to denaturation. Consequently, monolayer cushioned membranes were introduced [101]. As shown in Figure 2.4 (b), these membranes differ from previously discussed SSMs by the presence of an additional monolayer between the solid substrate and the membrane [102-106]. The intermediate amphiphilic layer substantially increases the aqueous layer thickness leading to the possibility of adding membrane-active molecules and observing their behavior in an unconstrained environment [107]. The biomolecule used should be amphiphilic, soft, able to attach to the membrane and the hydrophilic surface while minimally interactive with the studied proteins avoiding unwanted interactions [103]. Conventionally, differentiation occurs between polymer-cushioned membranes and tethered membranes. The most common polymers adopted are polyelectrolytes polymers

[105, 108, 109], which are driven by electrostatic forces to abide to the solid surface, and lipopolymers [110], which are lipid-like polymers that bind themselves between the phospholipids and the solid substrate. Tethered bilayers lipid membranes, or tBLMs, are supported via tethering of thiolipids [111-113],which are amphiphilic molecules possessing a hydrophilic separator [114]. Zhang et al. used a conductive polymer–poly(3,4-ethylenedixoythiophene) polystyrene sulfonate (PEDOT:PSS)–as the membrane's cushion forming a biological transistor [115]. In addition, the polymer layer can be altered to form a complex mesh similar to that of the extracellular matrix, improving the system's physiological similarity [116].

The membrane resistance in this case is approximately one order of magnitude lower than that of cell membranes and several orders of magnitude lower compared to other model membranes [98, 99]. This has been interpreted by the presence of scattered voids in between the lipids packing caused by the solid surface roughness [117]. Multiple successful efforts have been presented to minimize these membrane defects and increase its resistance, including the addition of a hydrogel layer leading to a smooth and functional surface for the compact attachment of tethered-protein, forming a tightly packed, defects-free giga-resistive membrane [112, 118]. In a recent study, solid supported membranes were formed through polar lipid fraction E (PLFE) remained stable in a microfluidic chip for 50 hours while maintaining a constant impedance value [119]. In the literature, electrophysiological studies of these membranes typically involve electroimpedance spectroscopy (EIS). The EIS works well with solid supported membranes as it characterizes the impedance of the individual layers.

Another model membrane technique that can be described as solid-supported is called the “tip-dip” technique [120]. First introduced by Coronado and Latorre, the model membrane is formed at the tip of a few micrometers wide glass pipette. In a lipids-dispersed aqueous solution, the hydrophilic glass pipette is submerged, and a lipid monolayer is formed at the water-air interface surrounding the pipette. Once the monolayer is formed and stabilized the pipette is removed and reentered into the aqueous solution several times, hence the “tip-dip” term. This manipulation of the pipette ensures the formation of the lipid bilayer at its tip when submerged in the aqueous medium. The preference of this approach over previously discussed solid supported membranes is enhanced when interested in single-channel recordings [121, 122]. The first attempt of these membranes led to 5–20 GΩ membranes while following efforts reached up to 100 GΩ by using a polyethylene glycol (PEG)–coated gold electrode [123]. In a comparison between membranes formed by the tip-dip method and membranes formed by the painting technique in studying gramicidin, Matsuno et al. found that even though both techniques enable reliable channel recordings, the tip-dip approach formed more stable and long lasting membranes allowing for minutes long recordings otherwise unachieved [121]. Furthermore, membranes formed at the tip of a glass electrode present the additional advantage of reversible membrane formation. Shoji et al., developed a gold-based electrode where lipids sheets were formed on gold-oil and water-oil interfaces and showed a directional dependency on protein gating [124], while Hirano et al., expanded this technique towards immobilizing proteins on hydrogel beads for prompt constitution of channels [125]. Challita et al. formed membranes at the interface of an aqueous droplet and a polyethylene glycol dimethacrylate (PEGDMA) hydrogel pipette, submerged in an oil dish [126] and emphasized reliable and repeatable membrane

formation. In this work, membranes were formed by piercing a lipid-oil medium with a lipid-coated electrode to contact another lipid-coated aqueous droplet.

### Membrane formed at the interface of immiscible fluids

In this section, two emulsion-based model membrane techniques will be presented, where at least one of the lipid monolayers is formed at the surface of an aqueous droplet submerged in an oil medium. The immiscibility of water droplets in oil drives the formation of lipid sheets at the hydrophilic-hydrophobic interface. These microfluidic-based model membranes allow for the utilization of emulsion science to determine membrane mechanics.

### Droplet on hydrogel bilayer

Emulsion-based lipid membranes have been reported since 1966 by Tsofina et al. and others [127-129]. However, it was not until the early 2000s that these techniques gained popularity for electrophysiological studies. Droplet on hydrogel bilayer, or a DHB, forms a model membrane at the interface of a water droplet and a hydrogel surface submerged in an oil medium [73, 130, 131], as shown in Figure 2.5. Molten [73], or spin-coated [132], hydrogel is placed on a glass coverslip forming a hydrophilic surface at the bottom of an oil well. The desired phospholipids are dissolved in the oil medium–or in the oil and droplet–and due to their amphiphilic property, self-assemble at the hydrogel-oil interface forming a lipid monolayer. Submerging a nanoliter aqueous droplet in the reservoir forms the second monolayer at the water-oil interface surrounding the droplet's surface. Once the monolayers are formed and stabilized, the droplet is placed on the hydrophilic surface leading to the formation of the lipid membrane at that interface, and

electrophysiology measurements are enabled through the presence of Ag/Ag-Cl electrodes on either side of the membrane [73, 131].

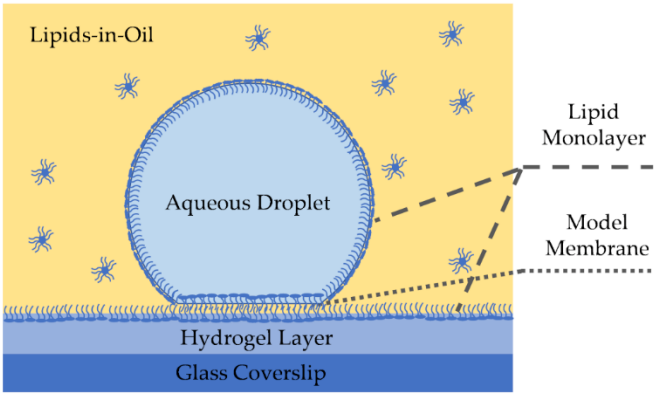


Figure 2.5: Side view of a droplet on hydrogel bilayer, or a membrane formed at a water-hydrogel interface in an oil medium. Here a hydrogel layer and a water droplet are submerged in a lipid-dispersed oil solution and the amphiphilic molecules self-assemble at the oil-hydrogel and at the oil-water interfaces forming monolayers. Placing the aqueous droplet on the hydrogel surface enables membrane formation.

DHBs have shown to provide high lateral lipid mobility as the smooth and homogeneous underlying hydrogel layer minimizes area defects leading to a high innate resistance [131]. Lateral lipid mobility enhances these membranes biological relevance and makes them a strong candidate for membrane-particle diffusion studies [130]. Additionally, the DHB setup enables full visualization of the membrane surface area within the focal plane of an inverted microscope [73], leading to an advantage in measuring properties dependent on the membrane area such as specific capacitance.

**Droplet interface bilayers**

Droplet interface bilayers, or DIBs, are model membranes formed at the adhered interface of two aqueous droplets submerged in an oil medium [133-135], as seen in Figure 2.6. Similarly to DHBs, DIBs require the presence of two immiscible fluids, aqueous droplets in oil. Lipids can be dispersed in the aqueous medium or in the oil medium, or

both. Due to their amphiphilic nature, the lipids self-assemble around the droplets surfaces and form lipid monolayers at the water-oil interface, which are then brought together forming the membrane. The droplets are often suspended from Ag/Ag-Cl electrodes enabling electrophysiological studies. In the case of droplet-based membranes, the equilibrium position of the droplets and the equilibrium membrane capacitance are denoted by the surface tension balances.

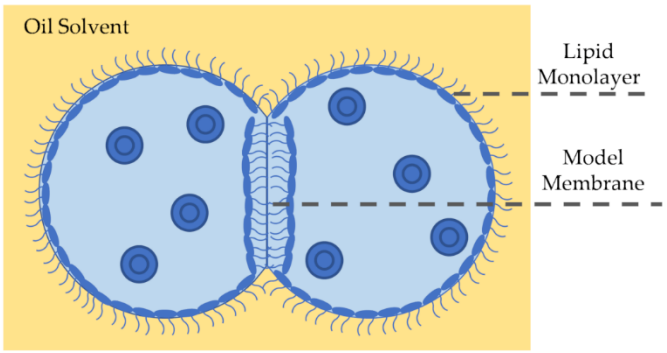


Figure 2.6: A DIB is a model membrane formed at the interface of two lipid-coated droplets in oil. Submerging lipid-dispersed aqueous droplets in an oil medium lead to the self-assembly of the amphiphilic molecules at the water-oil interface forming the monolayers. Note that it is possible to have the phospholipids dispersed in oil or water. Placing the droplets into contact, the membrane spontaneously forms at their adhered interface. The droplets contact angle links the membrane mechanics to the DIB's equilibrium state is dictated by the balance of surface tensions.

The DIB technique enables the formation of freestanding liquid-in-liquid membranes able to respond to externally applied forces, including the electric field across the membrane [136, 137]. Note that despite the droplets' attachment to silver electrodes, these wires are micrometers thick in diameter leading to a minute physical constraint, which does not overly restrict the DIB interface from expanding or shrinking as needed. Thus, the DIB allows for a direct link between interfacial tensions and membrane biophysics, permitting visual measurements of membrane qualities. Membrane surface tension is measured by balancing forces at the triple point of contact. The system's

equilibrium is defined by the contact angle between the droplets and it is utilized to monitor the behavior of membrane tension under changing conditions such as a varying electrical field [137]. DIBs present another advantage as they form asymmetric membranes in a simple yet controllable manner by dispersing different lipid mixtures in each droplet [138, 139]. Furthermore, these emulsion systems allow for the assembly of membranous networks for investigating synthetic tissues [140] and bespoke model environment for studying transmembrane exchanges [141].

DIBs present challenges including the assumption of spherical droplets and complications arising from the surrounding oil reservoir. When investigating DIB mechanics and observing droplets through an inverted microscope, it is often assumed that the droplets are spherical, and that the membrane surface area is consequently circular. However, the presence of surfactants at the droplets surfaces leads to a reduction in the water-oil surface tension [142] to magnitudes of approximately 1 mN/m [136, 137, 143], making the droplets sag from perfect spheres to hanging droplets, and thus the membrane area is an ellipse rather than a perfect circle. This issue has been addressed by multiplying the membrane area by a compensating factor depending on the monolayer surface tension and the oil density [137], or by placing a side view camera allowing for measurements of both principal diameters of the elliptical membrane [136, 143]. As for the immense oil reservoir surrounding these membranes, it largely influences the resulting thickness and elasticity of the produced membranes [73]. The solvent's viscosity affects the intensity and the pace at which the membrane responds to external stimuli, by inducing a resistance that the leaflets must overcome to adjust the membrane's geometry accordingly. Moreover, when amphiphilic molecules are dispersed within the droplets, the encapsulating oil-water

interface is likely to attract the molecule and drive it from its desired location – in between the membrane leaflets which may be measured through electrophysiological techniques – to its more favorable hydrophobic environment, interfering with the designed experimental conditions.

## Electrophysiological methods for characterizing lipid membranes

Electrophysiology is a fundamental technique in cellular biology, especially for studying cell membranes. Ag/Ag-Cl electrodes are introduced to the aqueous phases adjacent to the membrane and connected to a patch-clamp amplifier. Voltage-clamp is the primary method discussed here, where the voltage drop between a source electrode and the ground is clamped to a desired waveform function, and the current necessary to maintain that voltage is recorded. The Ag/Ag-Cl electrodes ensure that this voltage drop falls primarily across the lipid membrane, and measurements are typically conducted in properly-grounded low-noise environments, enabling measurements of the current within the picoamps range. Precise current-voltage relations are produced for lipid membranes through this approach and translated into membrane properties and interactions through various interpretations of the membrane structure.

In this chapter, electrophysiology-based characterization approaches are presented along with the membrane properties they assess. While multiple model membrane properties are mentioned herein, focus will be placed on four membrane-defining characteristics: membrane capacitance $C_s$, membrane conductance $G_s$, membrane intrinsic potential $\Delta\varphi$, and membrane surface tension $\gamma_b$. These aspects are used to reveal membrane structure and changes in their values will be interpreted into membrane dynamics.

Model membranes are typically studied using voltage-clamp mode, where a voltage is prescribed and the current necessary to maintain it is measured. The applied voltage and the generated current are then interpreted using an electrical model of the membrane to separate contributions from its capacitance and conductance. As shown in Figure 2.7 (a), the standard electrical representation of membranes is a variable capacitor in parallel with a resistor [144, 145]. The current *I(t)* passing across the double layer possesses a capacitive and a resistive component as following:

$$\boldsymbol{I(t) = C_m \frac{dV(t)}{dt} + V \frac{dC(t)}{dt} + G_m V(t)} \qquad (2.1)$$

where *V(t)* is the voltage across the membrane, and $C_m$ and $G_m$ are the membrane total capacitance and conductance, respectively. The first two terms on the right-hand side of the equation denote the capacitive current taking into consideration the soft nature of this biological capacitor. The third term represents the resistive current and is calculated solely through the direct voltage component. Varying the nature of the applied voltage allows for the isolation of the membrane electrical properties, $C_m$ and $G_m$, which may be then used to infer membrane structural qualities. It is important to note that these are the properties of the membrane as a whole.

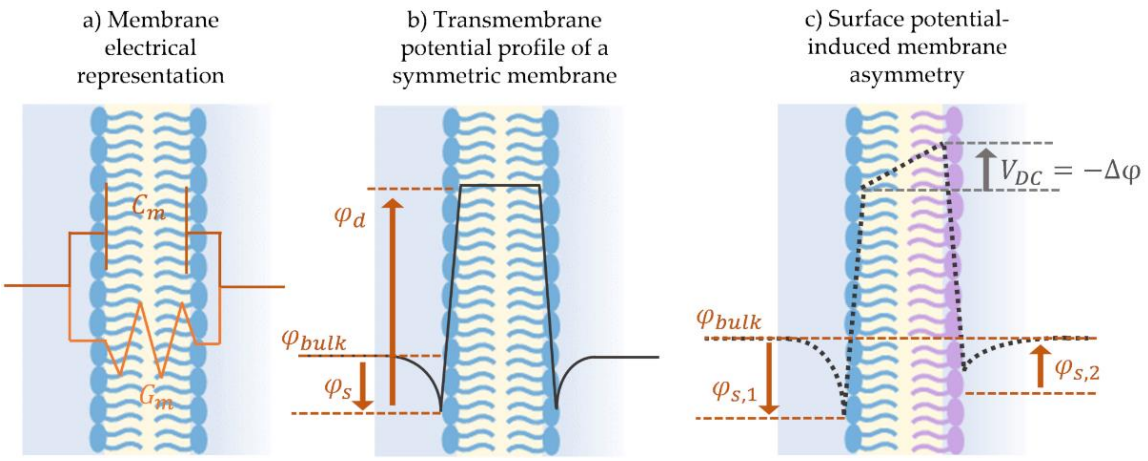


Figure 2.7: Membrane electrostatics. (a) Membranes are electrically modeled as a capacitor and a resistor in parallel. Membrane capacitance arises from the permittivity difference between the inner hydrophobic layer and the two outer hydrophilic surfaces, providing the membrane its ability to retain charge. Membrane resistance arises from its impermeability to dissolved species, except in the presence of conductive channels or pores. (b) The monolayer surface potential, $\varphi_s$, and dipole potential, $\varphi_d$, summarize the overall transmembrane potential profile. In the case of a symmetric membrane, lipid leaflets are identically composed and consequently show similar surface and dipole potentials. This leads to a symmetric transmembrane potential profile, as indicated by the solid lines. (c) In the case of an asymmetric membrane, the lipid leaflets are formed with different lipid mixtures leading to different surface and/or dipole potentials. This schematic illustrates an example of one leaflet possessing a lower surface potential generating a mismatch across the membrane, characterized by the asymmetric potential in the bulk, $\Delta\varphi$. When electrodes are placed in the bulk and the membrane is short-circuited in voltage-clamp mode at 0 mV, an electric field is produced across the membrane as the asymmetric values in the bulk are corrected.

Membranes owe their capacitive nature to the dielectric permittivity difference between the hydrophobic fatty acid chains— $\varepsilon_r \sim 2.2$ [146]—forming the membrane's middle layer, and the hydrophilic headgroups forming the two outer surfaces— $\varepsilon_r \sim 5$ [146]. This difference in permittivity leads to a parallel plate capacitor-like structure and behavior, where the capacitor's permittivity is approximated as that of the hydrocarbon interior [147]. Model membrane specific capacitance, $C_s$ denoted as capacitance per unit area, depends on the lipids and solvent used, the bilayer's geometry, as well as the forces applied on the fluidic system [148]. It is used to calculate membrane dielectric thickness

according to the parallel plate capacitor equation. Note that this membrane thickness is the water-to-water distance across the phospholipids double layer, which is sometimes altered by the presence of water molecules near the hydrophobic group due to dynamic fluctuations [70, 149]. The resistive component, $G_m$, on the other hand, depends on the membrane's permeability or the presence of ions conductive channels. The cell membrane's main role is a selective barrier as it reacts to each pore-forming agent differently [150]. Defects, pores, and channels across the membrane increase the membrane's conductance as ions travel through the pathways to the other side. A perfectly sealed membrane with no conductive channels, presents a high resistance in the order of giga-ohms and the electrical current is primarily capacitive.

The approximation of the membrane as a capacitor and a resistor loses sight of its underlying electrochemical structure. The molecular composition of the individual lipid presents fixed charges along its profile producing localized electric fields. The position and amplitude of these fields establish the overall transmembrane potential profile across the membrane thickness [146]. In summary, each lipid leaflet possesses a surface and a dipole potential. First, the leaflet's surface potential is induced by surface charge at the aqueous-phospholipid interface, and depends on the phospholipids charged headgroups as well as on the surrounding electrolyte concentration [151]. Second, the dipole potential is typically present at the linking group joining the hydrophilic and hydrophobic parts of the amphiphilic molecule [152], and this potential is largely independent of the aqueous solution and is a function of the selected lipids [153, 154]. Any asymmetry between the leaflets concerning these underlying electrostatics generates a membrane potential, $\Delta\varphi$, characterized by the overall offset in the transmembrane potential profile.

Not to be confused with the resting potential of natural membranes, model membrane potential discussed herein is the result of an imbalance between the leaflets electrostatics, induced by short-circuiting the model membrane through Ag/Ag-Cl electrodes [144]. Figure 2.7 sketches the transmembrane potential across (b) a symmetric model membrane formed from similar lipid leaflets and possessing a null overall potential, in comparison to (c) an asymmetric membrane where the leaflets are formed with two different lipids leading to the presence of a membrane asymmetric potential, $\Delta\varphi \neq 0$ [138, 139, 144, 155]. Membrane potential is a key element in conducting membrane electrophysiological studies and in characterizing membrane surface interactions. It is traditionally measured by equating it to a compensating external electrical field. Consequently, electrophysiological techniques readily allow for measurements of membrane asymmetry or the membrane transverse structure, while measurements of lateral variations within the membrane are more challenging.

From a surface chemistry point of view, the resulting model membrane is a thin film separating two fluid-fluid or fluid-solid mediums and thus possesses a surface tension, $\gamma_b$, governed by a balance of attractive and repulsive forces, and expressed as excess energy per unit area [156]. The membrane tension indicates the favorability of this surface in the system and mainly depends on the phospholipids-solvent combination used [136, 139], but can also be altered electrically [137, 157] or mechanically [158]. Membrane surface tension allows for the calculation of the total energy of the system leading to membrane mechanics understandings otherwise unexplained [136]. The following sections present the most adopted electrophysiological techniques aiming at investigating one or a combination of

these four characteristics, while highlighting the connection between model membrane setup and the electrical approach and interpreting the results into membrane findings.

### Conductance measurements

Conductive channels are the cell's primary mode of exchange across the near-impermeable double layer [1]. These are either formed naturally by the cell or synthetically by the interference of foreign agents such as the case of an actively attacked bacterial cell wall [159, 160]. Depending on the cell's type, cycle, and surrounding, these molecules form different configurations of pores or defects across the lipid barrier, detected as an increase in the membrane conductance [150]. Model membranes present a reliable platform to estimate the disruption of these agents at the cellular wall. Broadly, a conductance study relies on tracking the current's offset while applying a DC voltage. The application of a constant DC voltage without an alternating component minimizes the capacitive currents and focuses solely on the resistive portion. Jumps in the recorded current and deviations from the reference level indicate the temporary disruption of the near-impermeable lipid barrier. Eliminating the capacitive currents from Equation (2.1), the resistive current is expressed as shown in Equation (2.2):

$$\boldsymbol{I_R = G_m V_{DC}}, \tag{2.2}$$

where $V_{DC}$ is the DC voltage applied and $G_m$ is the membrane conductance. In these studies, the membrane's innate or base resistance must be controlled for successful experiments and reliable data. In fact, the membrane resistance must be in the giga-ohms range, conventionally called a giga-sealed membrane, as illustrated in Figure 2.8 (a), prohibiting any ion transport that is not induced by the biomolecule in question and thus enabling single channel recordings, as seen in Figure 2.8 (b).

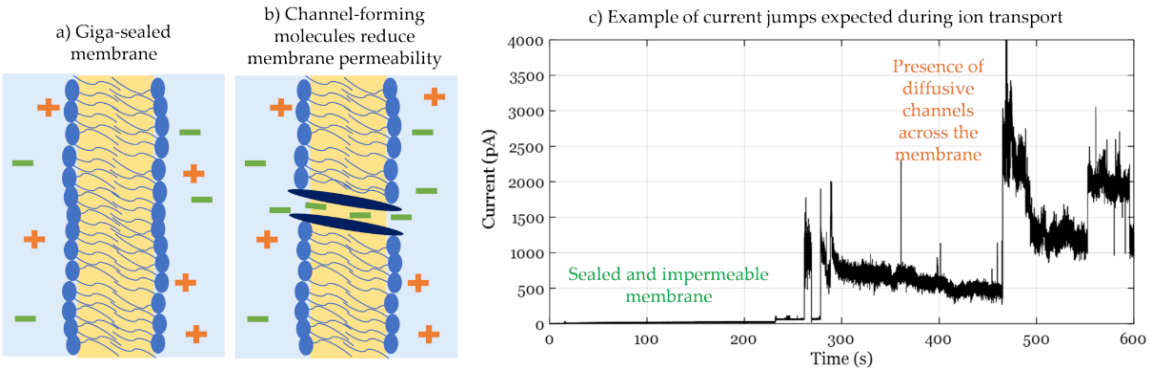


Figure 2.8: Membrane conductance studies. (a) Giga-sealed membranes present tightly packed lipid sheets where the hydrophobic layer inhibits ionic transport (b) Once a channel forming molecule–peptides, polymers, or others–integrates across the membrane leaflets, ions transporting channels are created and the gross membrane conductance is increased. This can be detected by applying a constant DC voltage and monitoring the membrane-generated current. (c) Adopted from *"Makhoul-Mansour, M.M., et al., Photopolymerized microdomains in both lipid leaflets establish diffusive transport pathways across biomimetic membranes. Soft matter, 2019. 15(43): p. 8718-8727".* Example of current behavior upon increase in membrane conductance. Conductance here is induced by the presence of channel-forming photopolymerizable phospholipids in DIBs generating defects in the membrane.

Conductance measurements reveal the mechanics of channel or pore-forming molecules, characterizing their dependence on concentration [161], membrane surface charge [162], and applied electrical field [163]. In addition, these measurements track the behavior of selective channels while varying the ionic species and their concentrations mimicking the ionic selectivity quality of biological membranes [164]. Conductance measurements require giga-sealed membranes to clearly observe agent-induced conductance events. Wu et al. presented a thorough study on the interaction of a variety of peptides in pore-spanning membranes, investigating if the cell membrane is their primary target when attacking bacterial walls [21]. To mimic the surface charge of gram-negative bacteria, they appropriately mixed zwitterionic and anionic phospholipids. They noticed that only a negative voltage allowed for conductive channel formation, which was explained by the fact that the peptides in questions were cationic demanding a negative

surface charge for surface adhesion highlighting membrane electrostatics. Also using pore-spanning membranes, Ashrafuzzaman et al. investigated the effect of gramicidin-S at the bacterial membrane [165]. They altered with the membrane surface charge and permeability by testing the peptide with zwitterionic phospholipids, then mixed with 20% anionic phospholipids, with and without the addition of cholesterol as the latter reduces membrane permeability [50, 166, 167]. Results showed that anionic and cholesterol-free membranes showed the highest interaction–higher conductance for a longer time–than neutral rigid membranes.

The DIB platform has also been used for conductance measurements, enabling flexible formation of lipid mixtures through control of lipid-dispersed droplets and solvent solutions. This allows for alternating the membrane's rigidity [166] and surface charge [151], in addition to the easy formation of asymmetric membranes [167], all affecting membrane-surface interactions. The use of DIBs in conductance studies has revealed multiple membrane mechanics including the activities of proteins, nanoparticles, and even the phospholipids themselves. The DIB platform enables mechanical membrane tension manipulation through parallel displacement of one droplet with respect to the other, allowing for the study of mechanosensitive protein channels [68, 158, 168]. de Planque et al. used the DIB platform to further investigate the effect of silica nanospheres on protein-free membranes [169]. The lipids were dispersed in the oil phase, whereas the nanoparticles were dissolved in one of the droplets indicating the trans side. The immiscibility of the liquids acts as a physical separation between the lipids and the silica particles inhibiting any pre-membrane interactions that might alter the resulting structure. Membrane conductance was tracked for various nanoparticle concentrations quantifying their effect

on membrane structure as well as their toxicity level. The DIB platform does not limit testing channels formed through external peptides but also through defects between the phospholipids themselves. Punnamaraju et al. demonstrated the behavior of 23:2 DiynePC photopolymerized phospholipids before and after UV light curing [170]. It was shown that these phospholipids form diffusive channels across the membrane only when they have been polymerized under UV light. Building on these original findings, Makhoul-Mansour et al. showed that additionally, pores only form when these phospholipids are present in both leaflets, example shown in Figure 2.8 (c) [155]. In this case, the DIB platform allowed the comparison between symmetric and asymmetric membranes for lipids-in-water and lipids-in-oil scenarios.

### Electrowetting and electrocompression-based techniques

The previous method focused on tracking the membrane conductance under a direct voltage, $V_{DC}$. The techniques presented herein shift the focus from membrane conductance to membrane capacitance, which is present in response to an alternating voltage. In this section, it will be assumed that the membranes are always giga-sealed, meaning there is no leak or permeability across the bilayer. The resistive current will be attenuated and thus ignored, only the capacitive current will be considered.

### Dynamic membrane capacitance in response to an electric field

Due to their fluidic nature, model membranes are soft capacitors able to react and thin to new dimensions in the presence of externally applied forces. Under an electric field, a lipid bilayer undergoes two main phenomena: a reduction in its surface tension leading to lateral expansion: electrowetting; and thinning between its leaflets: electrocompression; as seen in Figure 2.9 (a) and (b). Similar to a sessile droplet sitting on a semi-conductive surface,

electrowetting is the reduction in the membrane tension under an electric field [157, 171-173]. Reducing the membrane surface tension enhances its favorability in the system leading to a relaxation or expansion in its area. This phenomena is recently used as the driving force for multiple droplet on a microchip manipulations [174, 175] as well as pore gating through membrane tension alterations [173]. However, this expansion is not always possible given boundary conditions and constraints on the model membrane. In pore-spanning membranes for example, membrane area is bounded by the size of the orifice leading to minimized adjustments. Whereas, in droplet-based techniques, the membrane is free to expand reaching the minimum energy desired under the new equilibrium, barring constraints provided by the attached electrodes. Simultaneously, dielectric stress leads to attractive coulomb forces causing the leaflets to thin in the transverse direction [73, 136]. This is denoted as electrocompression which occurs in all model membranes and whose magnitude depends primarily on the selected solvent and slightly on the lipids used. Combining the two phenomena, the introduction of an electric field across the membrane leads to membrane thinning and expansion when possible which causes a change in the membrane total capacitance in response to voltage, or electrostriction. The geometrical dependence of the membrane capacitance is explained by the approximation of planar membranes as parallel plate capacitors:

$$\boldsymbol{C_m = C_s A_m = \frac{\varepsilon}{d} A_m} \tag{2.3}$$

where $C_s$ is the membrane specific capacitance or capacitance per unit area, $C_m$ is the membrane total capacitance, $A_m$ is the membrane area, $\varepsilon$ is the effective permittivity considering that of the hydrocarbon chains and $d$ is the membrane dielectric thickness. Thus, an increase in membrane area and a reduction in its thickness cause an overall

increase in the total capacitance, which is quadratic with respect to the voltage, or linear with the voltage squared [145], as seen in Figure 2.9 (d)**.** Considering Equation (2.1), membrane generated capacitive current depends not only on the alternating voltage but also on the consequential variation in membrane capacitance, *C*(*V*). Membrane generated current and changes in capacitance with voltage follow these equations:

$$\boldsymbol{I(t) = C(V)\frac{dV}{dt} + V(t)\frac{dC}{dt}} \tag{2.4}$$

$$\boldsymbol{C(V) = C_0(1 + \alpha(V + \Delta\varphi)^2)} \tag{2.5}$$

where $\Delta\varphi$ is the membrane asymmetric potential, $C_0$ is the minimum membrane capacitance corresponding to zero total electric field, and $\alpha$ is the electroresponse coefficient. The value for $\alpha$ varies with frequency and should not be confused with the steady state response to a voltage denoted γ, in Figure 2.9 (d). In the following paragraphs, electrowetting and electrocompression techniques based on tracking changes in membrane capacitance with respect to the electrical field will be discussed as these unfold multiple membrane properties such as membrane composition, monolayer surface tension, membrane potential, and others. It is assumed that the alternating component of the voltage signal does not influence the membrane dimensions.

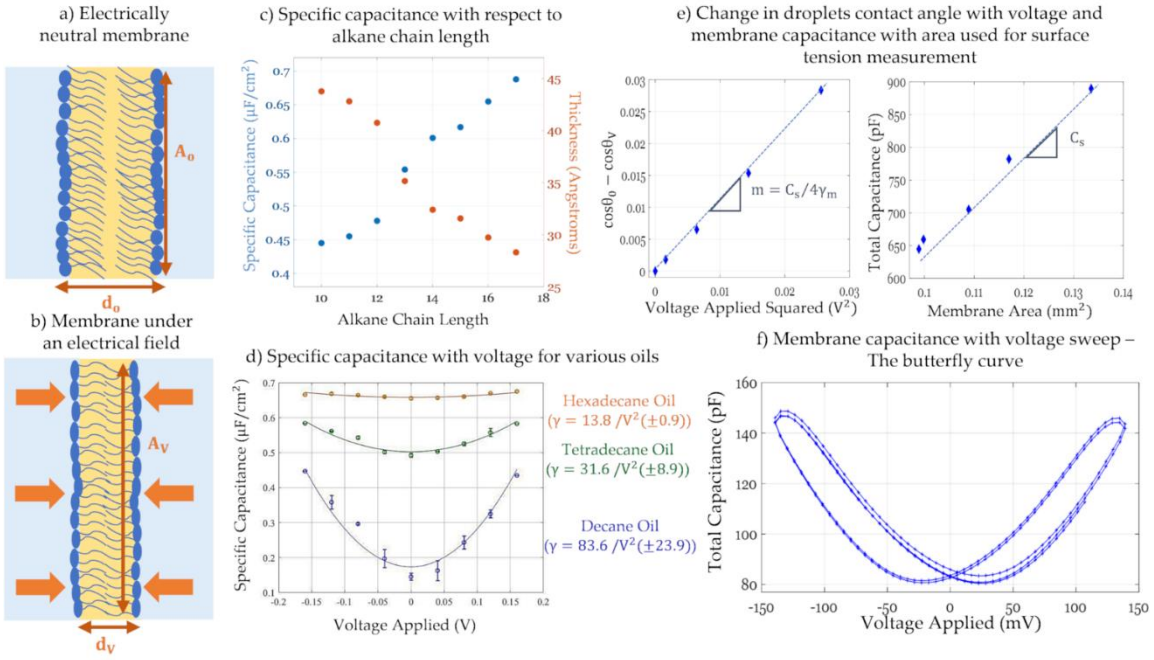


Figure 2.9: (a) With zero intramembrane electric field, the membrane is at its relaxed state with an initial geometry suitable for the system's equilibrium. (b) When an electrical field is applied, the membrane undergoes electrocompression-reduction in thickness due to attractive coulomb forces and if the setup allows electrowetting-increase in membrane area due to a reduction in surface tension. (c) Reproduced from *"Gross, L.C., et al., Determining membrane capacitance by dynamic control of droplet interface bilayer area. Langmuir, 2011. 27(23): p. 14335-42."* Specific capacitance and thickness of membranes composed of the same phospholipids, but with varying alkane chain length shows the solvent effect on membrane properties. (d) Reproduced from *"El-Beyrouthy, J., et al., A new approach for investigating the response of lipid membranes to electrocompression by coupling droplet mechanics and membrane biophysics. Journal of the Royal Society Interface, 2019. 16(161): p. 20190652".* Specific capacitance with respect to voltage for different solvents showing the latter's effect on the membrane's elasticity. (e) Adapted from *"El-Beyrouthy, J., et al., A new approach for investigating the response of lipid membranes to electrocompression by coupling droplet mechanics and membrane biophysics. Journal of the Royal Society Interface, 2019. 16(161): p. 20190652".* The DIB set up allows for a direct in-situ measurement of monolayer surface tension by monitoring the change in droplets contact angle, and thus membrane tension, with voltage, assuming constant membrane thickness. (f) Changes in membrane capacitance due to a relatively fast voltage sweep leads to a butterfly shaped curve. The point of overlap indicates transmembrane potential compensation.

The general approach for tracking capacitance with changing voltage is by applying a signal of the form: $V(t) = V_{DC} + V_0 \sin(\omega t)$ across the membrane. Varying the value of $V_{DC}$ in a slow step function, the equilibrium capacitance is calculated at each step. Total

capacitance amplitude is obtained by measuring the output current amplitude and using the capacitor voltage-current relation, as such: $C_V = I/\left(\frac{dV}{dt}\right)$. The change in capacitance with time in this case is set to zero, $dC/dt \approx 0$, as the equilibrium value is of interest. As for the membrane area, it is mainly obtained via visual estimations including light microscopy. Combining the capacitance with the membrane area, the specific capacitance and thus the dielectric thickness can also be calculated, based on Equation (2.3). Furthermore, plotting the equilibrium capacitance with respect to $V_{DC}$, leads a quadratic equation as seen in Equation (2.5) and in Figure 2.9 (d). The resulting parabola is centered at zero in the case of symmetric membranes, but in the case of asymmetry, it is shifted by a compensating voltage that equals in magnitude but opposites in field direction to the membrane asymmetric potential, i.e., $\Delta\varphi = -V_{DC}$. At this voltage, the membrane initial electric field is compensated. This is denoted as the minimum capacitance technique to obtain the membrane potential [138, 145].

In this process, one must be mindful of the signal frequency as well as the equilibration time between each voltage step. In fact, membrane impedance, as shown in Figure 2.7 (a), is frequency dependent, so the frequency adopted, $\omega$, must fall within a certain range where the capacitance dominates over the resistance [176, 177]. Even though the model membrane is impermeable, and the conductance is theoretically zero, if using an inappropriate frequency, the generated current may include a resistive component while considered as purely capacitive. Second, the wait time between the voltage steps must allow for the membrane to reach its new equilibrium, so that the capacitance indicates the steady state value. Mainly depending on the oil's viscosity [72, 126, 178] but also on the

membrane size, the time needed for the membrane to reach steady state differs from one bilayer to another and must be adjusted accordingly.

Emulsion-based membranes present a suitable platform in electrowetting and electrocompression analysis as their fluidic nature enables an unconstrained response to the electrical field and a direct connection between droplets geometry and membrane electrophysiology [179]. The following paragraphs focus on some of the recent innovations in membrane characterization developed through droplet-based membranes. Gross et al., adopted the DHB platform to track membrane capacitance with alternating areas via changes in voltage [73]. In that work, multiple model membranes were formed with the same phospholipids while varying the organic solvent, from short to long chain length oils. The DHB platform allows for a direct visualization of the membrane area through an inverted microscope, enabling accurate thickness calculations. Findings included a reduction in membrane thickness and elasticity as the oil chain length increases, as observed in Figure 2.9 (c). In fact, low chain alkane leaves residuals in between the leaflets during monolayers adhesion, leading to a solvent-full membrane able to significantly thin by expelling these residuals. Higher chain oils will not remain between the leaflets leading to a solvent-free membrane with not much room for further thinning. In this work the contact angle was estimated assuming a spherical cap geometry of the droplet.

Direct measurements of this contact angle may be achieved visually in the DIB approach. Taylor et al. presented a DIB based approach that relies on an altered Berge-Lippmann-Young equation to calculate the monolayer surface tension in-situ [137]. In the DIB setup, the membrane tension is balanced by the two monolayer surface tensions as follows:

$$\boldsymbol{\gamma_b = 2\gamma_m cos\theta_m} \tag{2.6}$$

where $\gamma_b$ and $\gamma_m$ are the bilayer and monolayer tensions, respectively, and $\theta_m$ is half the contact angle in between the droplets. Through an inverted microscope, direct contact angle measurement is possible and hence the calculation of the bilayer tension according to Equation (2.6), providing that the monolayer surface tension is separately measured, using for example the pendant drop approach [142, 180]. Alternatively, Taylor et al. proposed balancing the energy of the applied electric field with the reduction in membrane tension, and assuming negligible electrocompression constant membrane thickness the monolayer tension was calculated. Berge-Lipmann-Young equation provides the balance of forces between the electric stress and the reduction in membrane tension: $\Delta\gamma_b = E_{elec}$. Using Equation (2.6) and the equation of a charged capacitor, the Berge-Lipman-Young equation specific for DIBs was introduced [137]:

$$\boldsymbol{cos\theta_0 - cos\theta_V = \frac{C_s}{4\gamma_m} V^2} \tag{2.7}$$

The slope of this equation as well as the membrane specific capacitance are obtained graphically as seen in Figure 2.9 (e), leaving the monolayer tension as the only unknown in Equation (2.7). Monolayer surface tensions obtained from this equation were compared to the ones form the pendant drop technique validating the accuracy of the

approach. Building on these two innovations, El-Beyrouthy et al. presented an enhanced DIB setup where the droplets are visualized from the bottom and the side view, allowing for simultaneous contact angle and membrane area measurements revealing additional membrane properties under dielectric forces [136]. This alteration allows for the direct measurement of a varying membrane specific capacitance, or thickness, considering electrocompression of the leaflets. In a similar effort, Rofeh et al. adjoined a side-view camera on the DIB platform allowing in-situ measurement of the monolayer tension through the pendant drop algorithm [143].

Capturing the change in membrane capacitance with a varying electric field was also investigated by Schoch et al. for the purpose of quantifying the membrane intrinsic potential and other membrane properties [144]. Schoch et al. formed solvent-full asymmetric pore-spanning membranes where membrane asymmetry was introduced through salt concentration mismatch causing surface potential difference. In that work, membrane capacitance was tracked with respect to a voltage sweep rather than voltage steps. The applied signal was composed of a high frequency low amplitude sinusoidal voltage added to a low frequency high amplitude triangular one driving the voltage sweep. The high frequency sinusoidal voltage was used for the capacitance calculations, whereas the low frequency signal alternates between $\pm$ $V_{DC}$ within a period of $T = 1/f_{slow}$. Membrane capacitance with respect to the slow voltage forms a butterfly shaped curve, as seen in Figure 2.9 (f). It has been shown that the butterfly curve is centered at the voltage compensating for the membrane asymmetric potential [144, 181]. Hysteresis is observed since the membrane is not allowed sufficient time for equilibration. Hysteresis is linked to how much and how fast the membrane responds under changes in electric force, depending

on the solvent and the frequency used for the voltage sweep [181]. The use of a solvent-full membrane produces greater sensitivities to electrocompression, enabling changes in capacitance that are easily detected. Since pore-spanning membranes were used in the original work, the change in total capacitance can be directly tied to changes in thickness as the membrane area is constrained, removing this additional variable.

**Membrane current analysis and attenuation techniques**

The previous paragraph presented the capacitance dependency on a changing electric field and its links to membrane properties and energetics. This paragraph focuses on attenuating the current generated across the membrane to find the minimum field. Analyzing the voltage necessary for minimum current instead of capacitance trends with respect to voltage enables faster and more frequent measurements. However, this comes at the cost of requiring an approach for attenuation. In 1980, Sokolov et al. first presented the Intramembrane Field Compensation (IFC) technique for measuring membrane asymmetric potential based on solvent-full pore-spanning membranes [182]. Lipid composition mismatch between the leaflets causes a membrane potential offset, as described in Figure 2.10 (a). The membrane asymmetric potential necessitates the application of an opposing external electrical field to compensate for its influence on membrane dimensions, and its measurement allows for investigating complex membrane biophysics [183] including membrane-particle interactions [184, 185].

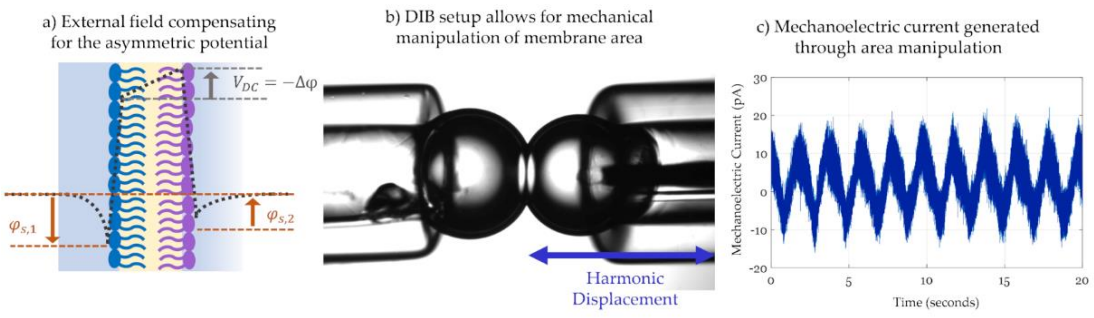

Figure 2.10: (a) Example of the transmembrane potential profile of a generic asymmetric membrane. Having two different leaflet compositions leads to an offset in the overall transmembrane potential, denoted as the membrane asymmetric potential, $\Delta\varphi$. The latter is composed of the difference between the surface potentials and the dipole potentials between the lipid sheets and can be measured based on the attenuation of an electrocompression-generated current. (b) The DIB setup allows for mechanical compression of the membrane through the displacement of one droplet with respect to the other, leading to mechanical adjustment of the membrane area. (c) This mechanical displacement leads to the generation of a mechanoelectric capacitive current.

IFC exploits the rapid changes in the membrane's thickness with an oscillating electrical field. To summarize, a voltage signal of the following form is applied: $V(t) = V_{DC} + V_0\, cos(\omega t)$. The voltage signal has a direct component, $V_{DC}$, and a sinusoidal component of a relatively high amplitude, $V_o$, and high frequency, $\omega$. Recalling Equation (2.4), membrane generated capacitive current includes changes in voltage and capacitance with respect to time. Since the instantaneous change in membrane capacitance is the driving element of this technique, it is crucial to consider both these terms of the capacitive current. The fast Fourier transform, or FFT, is then applied to the current dividing it into its harmonics. Replacing the fast change in capacitance, by: $C(t) = C_0(1 + \alpha V(t)^2)$, and the true voltage drop across the membrane, by: $V(t) = (V_{DC} + \Delta\varphi) + V_0\ sin(\omega t)$, where $\Delta\varphi$ is the membrane potential due to its asymmetry, into Equation (2.4), the first two current harmonics are as follows [186]:

$$\boldsymbol{I_{\omega} = V_0 \omega C_0 \left[1 + 3\alpha (V_{DC} + \Delta\varphi)^2 + \frac{\alpha V_0^2}{2}\right] sin(\omega t)} \tag{2.8.a}$$

$$\boldsymbol{I_{2\omega} = 3\alpha V_0^2 \omega C_0 (V_{DC} + \Delta\varphi)\, sin(2\omega t)} \tag{2.8.b}$$

As would be expected, the first harmonic, shown in Equation (2.8.a), is the most dominant as $\omega V_0 C_0$ is a direct integration of the voltage according to the impedance of a capacitor. However, the second harmonic is the one of most interest in this technique.

Equation (2.8.b) shows that the amplitude of the second harmonic is approximately linear with the total electrical field, $(V_{DC} + \Delta\varphi)$, and it equals zero when the applied voltage matches the membrane potential, i.e., $V_{DC} = -\Delta\varphi$, rending the oscillating voltage symmetric about a compensated intramembrane field. Thus, the technique proposed by this original work analyzes the membrane current, examines the harmonics of the signal, then alternates the DC voltage while monitoring the second harmonic until the second harmonic is attenuated. Upon attenuation, the DC voltage successfully compensates the membrane asymmetric potential.

For the measurement of the membrane potential, IFC does not require any capacitance or even current calculations, requesting solely the attenuation of the second harmonic to its feasible minimum. Furthermore, it untangles the experimental design from any geometrical constraints such as a fixed or a variable membrane surface area or tracking the changes in membrane thickness, emphasizing its advantage over the minimum capacitance technique in measuring the membrane potential. However, the second harmonic presents a relatively small amplitude, so experimental amplifications are needed to clearly differentiate it and to have an intensified change with varying $V_{DC}$. The electroresponse coefficient, $\alpha$, describes the capacitance change with respect to voltage, as seen in Equation (2.5), quantifying the membrane response intensity. The original work of Sokolov et al. used pore-spanning membranes, which are typically formed with shorter chain alkanes leading to a pronounced thinning in response to the electrical field, amplifying the value of $I_{2\omega}$ and making it more susceptible to changes in $V_{DC}$. Additionally, in the case of pore-spanning membranes, electrocompression is the main response to an electrical field as the membrane area is bounded by the orifice surface, making

electrowetting phenomena negligible. Thus, $\alpha$ represents the electrocompression intensity of the thickness-alternating membrane. If using membranes that are not laterally constrained instead, such as DIBs, $\alpha$ would represent the total electroresponse including electrowetting and electrocompression combined and differentiating between the two phenomena requires additional calculations and considerations which would not affect the IFC design but might be used to reveal additional membrane mechanics beyond the intrinsic potential [181]. Furthermore, the alternating voltage amplitude and frequency must be tuned as well. In theory, the highest amplitude and frequency that can be experimentally provided are desired as these amplify the second harmonic amplitude. However, these values must be chosen carefully to avoid overcompensation leading to opposite results. In fact, using an overly high frequency might be too fast for the membrane to follow and thin due to the solvent viscous effects [181]. In addition, the frequency must present a capacitance-dominant impedance without interference from the electrolyte resistance [176]. Thus, the sinusoidal voltage amplitude and frequency must be large enough to amplify the membrane response, but care must be taken not to overcompensate and lead to a nonresponsive membrane or to a resistance-dominated impedance.

As explained in the previous paragraph, IFC is most effective when used on solvent-rich highly elastic membranes. This primarily includes pore-spanning membranes that multiple researchers adopted and, following the original work, used the IFC method to investigate not only membrane asymmetric potential but additional membrane properties and mechanics [184]. Pohl et al. used solvent-full BLMs and applied IFC to track pH-driven lipid flipflop events [183]. Advancing the approach, Passechnik accounted for the heterogeneity of the membrane layers and re-developed the current harmonic equations

while considering the electric stress and membrane compression moduli [187], allowing for the localization of charges across the double layer levels [185]. Solvent-full droplet-based membranes are also favorable for IFC measurements. In fact, El-Beyrouthy et.al built highly elastic membranes by forming DIBs with decane oil [73], and combining this membrane with an automated control system, the IFC fundamentals were successfully utilized for obtaining a rapid and real-time reading of asymmetric membrane potentials [188].

Inspired by the alternating change in membrane capacitance, Freeman et al. used the DIB platform to create a droplet compression system that generates mechanoelectric current [189]. Figure 2.10 (b) shows how the droplets-based platform is manipulated to generate current through displacement rather than the application of an electric field. Equation (2.4) shows that the capacitive current across the membrane is enabled through two components: an alternating voltage and an alternating capacitance. The initiative of this work focuses on the alternating capacitance ($dC/dt$) achieved by varying membrane area through compression of the droplet pair in a rhythmic fashion using a piezoelectric actuator [158, 189]. An example of this mechanically induced current is shown in Figure 2.10 (c). The ability to mechanically compress the membrane is possible through the fluidic nature of DIBs and the change in area was shown to be substantial enough to be detected by tension-driven peptides [158, 190]. However, the main restriction of this technique remains in the maximum change in area possible by the interface. Similarly to the frequency issue discussed in the IFC technique, the displacement frequency has to be high enough to increase the current amplitude but slow enough to allow the membrane to respond accordingly, otherwise the current is attenuated. Additional mechanoelectric work

showed that a lower displacement frequency promotes a higher change in membrane area [158].

## Electroimpedance spectroscopy

The simple electrical representation of the membrane as a capacitor in parallel with a resistor is true under the condition that the frequency applied leads to a dominant membrane impedance, $Z_m(\omega) = 1/(G_m + j\omega C_m)$, where $G_m$ and $C_m$ are the membrane specific conductance and capacitance, respectively [191]. This impedance is that of the membrane core, however, the entire fluidic double layer structure contains additional regions of interest. In addition to the core membrane impedance, the electrical double layer capacitance, $C_{GCS}$, and the electrolyte solution resistance, $R_e$, are present when considering the entire electrical circuit [117], as illustrated in Figure 2.11 (a). Generally, and for the ease of analysis, the impedance of the electrical double layer at the hydrophilic-aqueous interface, $C_{GCS}$, is either ignored or added to the membrane impedance. The reasoning behind this is that the capacitance of this layer is significantly high compared to that of the membrane, leading to a much smaller influence on the system's equivalent impedance. While commonly being an unwanted impedance, the electrolyte resistance is avoided by using an appropriate frequency range [176] and a specific salt concentration [192].

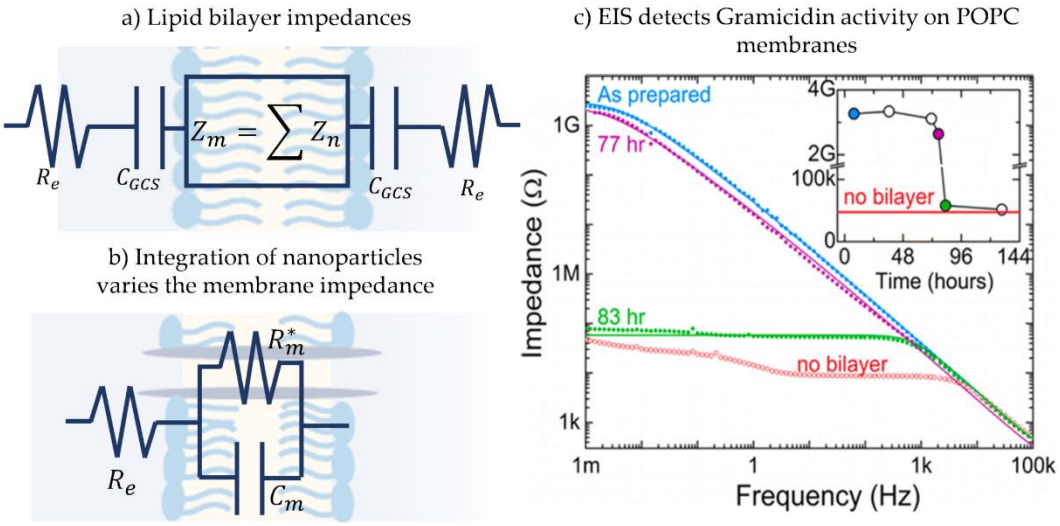


Figure 2.11: (a) The overall membrane electrical behavior is often more complex than a resistor and a capacitor in parallel. The electrolytes resistance *Re* and the capacitance of the electrical double layer $C_{GCS}$ are also present in the electric circuit, but the membrane impedance typically dominates the response. However, the double layer itself and its surrounding can be divided into tuned impedance layers depending on the hypothesis in question and each layer is detected through varying frequencies. (b) A common electrical circuit when investigating channel-forming proteins in membranes: the electrolyte solution resistance, $R_e$, in series with membrane capacitance, $C_m$, and membrane resistance, $R_m$. The latter is variable in the presence of membrane-protein activities. (c) Copied from "Korman, C. E., et al. (2013). "Nanopore-spanning lipid bilayers on silicon nitride membranes that seal and selectively transport ions."29(14): 4421-4425. Membrane conductance was tracked via EIS investigating the effect of Gramicidin on POPC membranes.

Electroimpedance spectroscopy, or EIS, is a frequency-based analysis that considers the model membrane's total impedance response with respect to a frequency sweep: Bode or Nyquist plots [191, 193]. It is distinguished from previously discussed techniques in the fact that it does not investigate changes in the intramembrane field but focuses solely on its electroimpedance response. In this analysis, each model membrane layer, or membrane component, is considered as a separate impedance element composed of a real and imaginary part indicating its conductance and capacitance, respectively. EIS consists of sending a small amplitude alternating voltage across the membrane while performing a frequency sweep. The voltage amplitude must be small enough to avoid any

nonlinear effects related to the presence of a high electric field [194]. As for the frequency range, it generally ranges from a few *mHz* to several *kHz,* depending on the resolution of the impedance analyzer [191, 195]. In addition, the data sampling frequency and the number of samples must be adjusted during the sweep to obtain evenly distributed data throughout the frequency range. The generated current and applied voltage are used to get the total impedance response impedance amplitude and phase angle. The generated Bode plots are then compared to the modeled equivalent circuit leading to capacitance and conductance measurements corresponding to various membrane layers. The electrical model for the membrane may be altered as needed dependent on the experimental data, revealing additional membrane layers properties such as area defects [117, 196].

Electroimpedance spectroscopy is commonly utilized on solid supported membranes, as this specific setup allows for the direct connection between bilayer and electrode, removing additional undesired impedance layers and increasing the frequency range otherwise limited. Figure 2.11 (b) presents a common electric circuit used to describe these membranes under EIS. Note that the membrane resistance, $R_m$, is variable in the presence of a channel-forming biomolecule and tracking membrane equivalent impedance mirrors changes in the conductance highlighting membrane-biomolecule interactions. In solid supported membranes, EIS helps detecting membrane formation [118, 197], separates the multi-layers of this membrane [98, 198, 199], as well as detects and localizes biomolecule attachment [99, 191, 195, 200-202]. Stelzler et al. utilized EIS on solid supported membranes made through two different approaches–LB/LS and vesicle fusion and compared the mechanics of ligand bindings in these membranes [117]. In EIS analysis, the electric circuit is adjustable as the electrical components can be either divided into sub-

impedances or grouped together. For example, Karolis et al. investigated the effect of cholesterol on egg lecithin bilayers while being interested in the specific location this sterol made the greatest effect on the phospholipids [203]. To do so, the electric circuit adopted consisted of 4 impedances each represent a different part of the phospholipid molecule: acyl chain, carbonyl, glycerol bridge and phosphatidylcholine. Whereas, Romer and Steiner used the EIS technique to obtain electrical properties of a newly developed model membrane, a hybrid between pore-spanning membrane and solid supported membrane [194]. For their hypothesis, the membrane was considered as one impedance since the interest was on the membrane as one entity with no need for added complexity. Figure 2.11 (c) shows the work of Korman et.al, who utilized EIS spectra to measure multiple POPC nano-membranes equivalent impedance [204]. This work characterized these membranes and investigated the effect of gramicidin, showing how this channel-forming protein increases the membrane conductance, and how the influence of gramicidin can be reduced with divalent cations, such as when $CaCl_2$ is used in the buffer solution. More recently, EIS has been utilized to characterize microcavity pore-suspended lipid bilayers for detecting membrane-drug activity [205], as well to investigate the adsorption and attachment of lipid vesicles on a solid substrate [206]. Not limited to solid-supported membranes, EIS has been used on networks of membranes formed by adhesive emulsion systems such as a network of DIBs, where the impedance response allows for multiple membrane studies and total network analysis [176, 177].

**Summary and conclusion**

This review presents a collection of common model membranes developed to mimic the structure of cellular membranes in a controlled environment. First, the formation

of liposomes, or lipid vesicles, which are similar in shape and size to natural membranes, is discussed followed by pore-spanning membranes formed at a hydrophobic orifice, whose high membrane resistance and elasticity allowed for the development of various electrophysiological approaches. Solid supported membranes are then presented highlighting their mechanical robustness and popular use in membrane-protein studies. Finally, two droplet-based membranes are described allowing for the direct correlation between emulsion mechanics and membrane biophysics. Table 2.1 summarizes these model membrane manufactures and their resulting properties.

Table 2.1. Summary of the discussed model membrane manufactures.

| Model Membrane | Liposomes | Pore-Spanning Membranes | Solid Supported Membranes | Emulsion-based Membranes | |
|---|---|---|---|---|---|
| | | | | Droplet on Hydrogel Bilayers | Droplet Interface Bilayers |
| **Description** | Lipid vesicles formed in an aqueous environment | Lipid bilayer formed at the orifice of a solid separator between two aqueous baths | Lipid bilayer formed on a solid support submerged in an aqueous solution | Lipid bilayer formed at a droplet-hydrogel interface | Lipid bilayer formed at a droplet-droplet interface |
| **Manufacturing Techniques** | Electroformation<br>Phase Transfer<br>Microfluidic Jets | Solvent painting<br>Monolayers folding | Langmuir-Blodgett/ Langmuir-Schaefer<br>Vesicle fusion | Microfluidic droplet deposition and manipulation in oil reservoirs | |
| **Advantages** | Similar in geometry and dimensions to natural membranes | Well-packed, high impedance membranes<br>Isolate transverse properties | Mechanically robust, stable, and long-lasting membranes | Full membrane area visualization | Direct tension measurements<br>Simple formation of asymmetric membranes |

Table 2.2 summarizes the second part of this review, which focuses on three fundamental electrophysiological approaches as well as their ongoing development. Membrane conductance is tracked to analyze membrane structure and surface interactions. Dynamic membrane capacitance and alternating current are utilized for revealing several membrane properties such as thickness, elasticity, surface tension and asymmetric potential, and electroimpedance spectroscopy allows for the tuned and detailed study of lipid membranes sub-layers.

Table 2.2. Summary of the discussed electrophysiology-based techniques.

| Electrophysiology technique | Conductance Measurements | Electrowetting and Electrocompression | | Electroimpedance Spectroscopy |
|---|---|---|---|---|
| | | Dynamic Capacitance | Current Attenuation | |
| **Fundamental Equation** | $I = G_m V_{DC}$ | $I(t) = C\frac{dV(t)}{dt}$ | $I(t) = (V_{DC} + \Delta\varphi)\frac{dC(t)}{dt}$ | $Z_m(\omega) = 1/(G_m + j\omega C_m)$ |
| **Experimental Approach** | Applying constant DC voltage and tracking the current | Applying step-DC voltage and calculating the equilibrium capacitance | Attenuating the current harmonics through varying the applied voltage. | Generating Bode or Nyquist plots and comparing them to the expected model circuit |
| **Common Applications** | Measuring channel-forming mechanisms of disruptive agents | Calculating membrane potential, dielectric thickness, and monolayer surface tension | Measuring membrane potential and rigidity Detecting intramembrane dynamics | Detection and localization of molecular adsorption and sensor platforms |
| **Experimental Requirements** | High base membrane resistance | Sufficient equilibrium time between voltage steps | Highly compressible membrane for enhancing measurements | High signal frequencies and compatible equipment. |

Cellular membranes are complex structures that facilitate a variety of intertwined functions in living organisms. Due to their complexity, it is often infeasible to untangle the variables responsible for their physiological properties and interactions. Therefore, synthetic model membranes are routinely used, mimicking the cell membrane's simple structure while presenting a flexible and tunable platform for the isolation and study of specific membrane biomechanics. These artificial membranes differ from the naturally occurring membranes as a result of their selected mode of assembly. The default impermeability of most model membranes makes them highly sensitive to minute changes in conductance, leading to accurate conductive channels' recordings for in-depth membrane-nanoparticles investigations. Furthermore, and depending on the solvent used, model membranes possess an enhanced membrane elasticity making them highly responsive to electrical forces. This amplified soft response allows for membrane structure

investigations, bending stiffness studies and for the direct measurement of membrane asymmetric potential. Free-standing model membranes such as droplet-based membranes result in a unique link between droplets geometry and membrane biophysics including membrane tension and membrane electrostatics.

In this review, we examined several common methods for producing these model membranes in the laboratory, highlighting differences in the produced membranes. Next, we discussed how these differences may be exploited for enabling alternative techniques for characterizing the membrane properties, focusing in particular on membrane-particle interactions. Model membranes are a simple representation of natural membranes and despite their undeniable deviation in shape and innate characteristics from biological membranes, they allow for investigations that might be more challenging in natural systems.

## References


1. Lodish, H. and A. Berk, *Molecular cell biology*. Vol. 3.
2. Grecco, H.E., M. Schmick, and P.I.J.C. Bastiaens, *Signaling from the living plasma membrane.* 2011. **144**(6): p. 897-909.
3. Honigmann, A. and A.J.J.o.m.b. Pralle, *Compartmentalization of the cell membrane.* 2016. **428**(24): p. 4739-4748.
4. Rothstein, A.J.D.o.t.F.S., *Compartmentalization of the cell surface of yeast in relation to metabolic activities.* 1956. **21**: p. 229-238.
5. Levental, I., K. Levental, and K. Simons, *The Differentiation of the Plasma Membrane*. 2013, Federation of American Societies for Experimental Biology.
6. Sundelacruz, S., et al., *Role of membrane potential in the regulation of cell proliferation and differentiation.* 2009. **5**(3): p. 231-246.
7. Corre, I., C. Niaudet, and F.J.M.R.R.i.M.R. Paris, *Plasma membrane signaling induced by ionizing radiation.* 2010. **704**(1-3): p. 61-67.
8. Nagasawa, H., et al., *Involvement of membrane signaling in the bystander effect in irradiated cells.* 2002. **62**(9): p. 2531-2534.
9. Sharma, A. and U.S. Sharma, *Liposomes in drug delivery: progress and limitations.* International journal of pharmaceutics, 1997. **154**(2): p. 123-140.
10. Landon, C.D., et al., *Nanoscale drug delivery and hyperthermia: the materials design and preclinical and clinical testing of low temperature-sensitive liposomes used in combination with mild hyperthermia in the treatment of local cancer.* The open nanomedicine journal, 2011. **3**: p. 38.
11. Kamiya, K.J.M., *Development of artificial cell models using microfluidic technology and synthetic biology*. 2020. **11**(6): p. 559.
12. Bhattacharya, A., et al., *A minimal biochemical route towards de novo formation of synthetic phospholipid membranes.* 2019. **10**(1): p. 1-8.
13. Tien, H.T. and A.J.E.A. Ottova, *Supported planar lipid bilayers (s-BLMs) as electrochemical biosensors.* 1998. **43**(23): p. 3587-3610.
14. Castellana, E.T. and P.S.J.S.S.R. Cremer, *Solid supported lipid bilayers: From biophysical studies to sensor design.* 2006. **61**(10): p. 429-444.
15. Jacobson, K., E.D. Sheets, and R.J.S. Simson, *Revisiting the fluid mosaic model of membranes.* 1995. **268**(5216): p. 1441-1443.
16. Singer, S.J. and G.L.J.S. Nicolson, *The fluid mosaic model of the structure of cell membranes.* 1972. **175**(4023): p. 720-731.
17. Simons, K. and W.L.J.A.R.B.B.S. Vaz, *Model systems, lipid rafts, and cell membranes.* 2004. **33**: p. 269-295.
18. Fox, C.F.J.S.A., *The structure of cell membranes.* 1972. **226**(2): p. 30-39.
19. Peetla, C., et al., *Biomechanics and thermodynamics of nanoparticle interactions with plasma and endosomal membrane lipids in cellular uptake and endosomal escape.* 2014. **30**(25): p. 7522-7532.
20. Peetla, C., et al., *Drug resistance in breast cancer cells: biophysical characterization of and doxorubicin interactions with membrane lipids.* 2010. **7**(6): p. 2334-2348.

21. Wu, M., et al., *Mechanism of interaction of different classes of cationic antimicrobial peptides with planar bilayers and with the cytoplasmic membrane of Escherichia coli.* Biochemistry, 1999. **38**(22): p. 7235-7242.
22. Soblosky, L., A. Ramamoorthy, and Z. Chen, *Membrane interaction of antimicrobial peptides using E. coli lipid extract as model bacterial cell membranes and SFG spectroscopy.* Chemistry and physics of lipids, 2015. **187**: p. 20-33.
23. Gibson Wood, W., et al., *Cholesterol asymmetry in synaptic plasma membranes.* 2011. **116**(5): p. 684-689.
24. Simons, K. and D.J.N.r.M.c.b. Toomre, *Lipid rafts and signal transduction.* 2000. **1**(1): p. 31-39.
25. Marquardt, D., B. Geier, and G.J.M. Pabst, *Asymmetric lipid membranes: towards more realistic model systems.* 2015. **5**(2): p. 180-196.
26. Aktas, M., et al., *Membrane lipids in Agrobacterium tumefaciens: biosynthetic pathways and importance for pathogenesis.* 2014. **5**: p. 109.
27. Israelachvili, J.N., D.J. Mitchell, and B.W.J.B.e.B.A.-B. Ninham, *Theory of self-assembly of lipid bilayers and vesicles.* 1977. **470**(2): p. 185-201.
28. Goldman, D.E.J.T.J.o.g.p., *Potential, impedance, and rectification in membranes.* 1943. **27**(1): p. 37-60.
29. Hamill, O.P., et al., *Improved patch-clamp techniques for high-resolution current recording from cells and cell-free membrane patches.* 1981. **391**(2): p. 85-100.
30. Grewer, C., et al., *Electrophysiological characterization of membrane transport proteins.* 2013. **42**: p. 95-120.
31. Mukherjee, P., et al., *Combined numerical and experimental investigation of localized electroporation-based cell transfection and sampling.* 2018. **12**(12): p. 12118-12128.
32. Siontorou, C.G., et al., *Artificial lipid membranes: Past, present, and future.* 2017. **7**(3): p. 38.
33. Khan, M.S., N.S. Dosoky, and J.D.J.I.j.o.m.s. Williams, *Engineering lipid bilayer membranes for protein studies.* 2013. **14**(11): p. 21561-21597.
34. Wu, L., X.J.A. Jiang, and b. chemistry, *Recent developments in methodology employed to study the interactions between nanomaterials and model lipid membranes.* 2016. **408**(11): p. 2743-2758.
35. Rascol, E., J.-M. Devoisselle, and J.J.N. Chopineau, *The relevance of membrane models to understand nanoparticles–cell membrane interactions.* 2016. **8**(9): p. 4780-4798.
36. Chatterjee, S., S.J.F.r.b. Agarwal, and medicine, *Liposomes as membrane model for study of lipid peroxidation.* 1988. **4**(1): p. 51-72.
37. Angelova, M.I. and D.S.J.F.d.o.t.C.S. Dimitrov, *Liposome electroformation.* 1986. **81**: p. 303-311.
38. Angelova, M. and D.S. Dimitrov, *A mechanism of liposome electroformation*, in *Trends in colloid and interface science II*. 1988, Springer. p. 59-67.
39. Collins, M.D. and S.E.J.J. Gordon, *Giant liposome preparation for imaging and patch-clamp electrophysiology.* 2013(76): p. e50227.
40. Pautot, S., B.J. Frisken, and D.J.L. Weitz, *Production of unilamellar vesicles using an inverted emulsion.* 2003. **19**(7): p. 2870-2879.

41. Ohno, M., et al., *Dynamic behavior of giant liposomes at desired osmotic pressures.* 2009. **25**(19): p. 11680-11685.
42. Ip, T., et al., *Manufacture of multi-layered artificial cell membranes through sequential bilayer deposition on emulsion templates.* 2021.
43. Stachowiak, J.C., et al., *Unilamellar vesicle formation and encapsulation by microfluidic jetting.* 2008. **105**(12): p. 4697-4702.
44. Kamiya, K., et al., *Cell-sized asymmetric lipid vesicles facilitate the investigation of asymmetric membranes.* 2016. **8**(9): p. 881.
45. Milardi, D., et al., *Proteostasis of islet amyloid polypeptide: a molecular perspective of risk factors and protective strategies for type II diabetes.* 2021. **121**(3): p. 1845-1893.
46. Elani, Y., et al., *Engineering multi-compartment vesicle networks.* 2013. **4**(8): p. 3332-3338.
47. Elani, Y., et al., *Measurements of the effect of membrane asymmetry on the mechanical properties of lipid bilayers.* 2015. **51**(32): p. 6976-6979.
48. Karamdad, K., et al., *Engineering thermoresponsive phase separated vesicles formed via emulsion phase transfer as a content-release platform.* 2018. **9**(21): p. 4851-4858.
49. Nasr, G., et al., *Liposomal membrane permeability assessment by fluorescence techniques: Main permeabilizing agents, applications and challenges.* 2020. **580**: p. 119198.
50. Papahadjopoulos, D., S. Nir, and S. Ohki, *Permeability properties of phospholipid membranes: effect of cholesterol and temperature.* Biochimica et Biophysica Acta (BBA)-Biomembranes, 1972. **266**(3): p. 561-583.
51. Fernandez-Puente, L., et al., *Temperature and chain length effects on bending elasticity of phosphatidylcholine bilayers.* 1994. **28**(3): p. 181.
52. Chaurasia, A.K., et al., *Evaluation of bending modulus of lipid bilayers using undulation and orientation analysis.* 2018. **97**(3): p. 032421.
53. Schulz, M., A. Olubummo, and W.H.J.S.M. Binder, *Beyond the lipid-bilayer: interaction of polymers and nanoparticles with membranes.* 2012. **8**(18): p. 4849-4864.
54. Zhang, S., A. Nelson, and P.A.J.L. Beales, *Freezing or wrapping: the role of particle size in the mechanism of nanoparticle–biomembrane interaction.* 2012. **28**(35): p. 12831-12837.
55. Chen, K.L. and G.D. Bothun, *Nanoparticles meet cell membranes: probing nonspecific interactions using model membranes*. 2014, ACS Publications.
56. Strobl, F.G., et al., *Intake of silica nanoparticles by giant lipid vesicles: influence of particle size and thermodynamic membrane state.* 2014. **5**(1): p. 2468-2478.
57. Koning, G.A., et al., *Hyperthermia and thermosensitive liposomes for improved delivery of chemotherapeutic drugs to solid tumors.* Pharmaceutical research, 2010. **27**(8): p. 1750-1754.
58. Mayhew, E., *Liposomes in Cancer In:"Liposome Letters", AD Bangham*. 1983, Academic Press, London.
59. Chen, Z.-J., et al., *Nanobowl-supported liposomes improve drug loading and delivery.* 2020. **20**(6): p. 4177-4187.

60. Kumar, B., et al., *Liposomes: novel drug delivery approach for targeting Parkinson's disease.* 2020.
61. Kim, C.H., et al., *Surface modification of lipid-based nanocarriers for cancer cell-specific drug targeting.* 2017. **47**(3): p. 203-227.
62. Mady, M.M., et al., *Biophysical characterization of gold nanoparticles-loaded liposomes.* 2012. **28**(4): p. 288-295.
63. Jølck, R.I., et al., *Engineering liposomes and nanoparticles for biological targeting*, in *Biofunctionalization of Polymers and their Applications*. 2010, Springer. p. 251-280.
64. Tai, L.-A., et al., *Thermosensitive liposomes entrapping iron oxide nanoparticles for controllable drug release.* 2009. **20**(13): p. 135101.
65. Faizi, H.A., R. Dimova, and P.M.J.a.p.a. Vlahovska, *Viscosity of fluid membranes measured from vesicle deformation.* 2021.
66. Correa, N.M. and Z.J.T.J.o.P.C.B. Schelly, *Dynamics of Electroporation of Synthetic Liposomes Studied Using a Pore-Mediated Reaction, Ag++ Br-⟶ AgBr.* 1998. **102**(46): p. 9319-9322.
67. Kolahdouz, E.M. and D.J.P.R.E. Salac, *Dynamics of three-dimensional vesicles in dc electric fields.* 2015. **92**(1): p. 012302.
68. Nomura, T., et al., *Unidirectional incorporation of a bacterial mechanosensitive channel into liposomal membranes.* 2015. **29**(10): p. 4334-4345.
69. Mueller, P., et al., *Reconstitution of cell membrane structure in vitro and its transformation into an excitable system.* 1962. **194**(4832): p. 979-980.
70. Montal, M. and P. Mueller, *Formation of bimolecular membranes from lipid monolayers and a study of their electrical properties.* Proceedings of the National Academy of Sciences, 1972. **69**(12): p. 3561-3566.
71. Fuks, B. and F.J.B.j. Homble, *Permeability and electrical properties of planar lipid membranes from thylakoid lipids.* 1994. **66**(5): p. 1404-1414.
72. Beltramo, P.J., L. Scheidegger, and J.J.L. Vermant, *Toward Realistic Large-Area Cell Membrane Mimics: Excluding Oil, Controlling Composition, and Including Ion Channels.* 2018. **34**(20): p. 5880-5888.
73. Gross, L.C., et al., *Determining membrane capacitance by dynamic control of droplet interface bilayer area.* Langmuir, 2011. **27**(23): p. 14335-42.
74. Batishchev, O.V. and A.V.J.B. Indenbom, *Alkylated glass partition allows formation of solvent-free lipid bilayer by Montal–Mueller technique.* 2008. **74**(1): p. 22-25.
75. White, S.H.J.B.e.B.A.-B., *Temperature-dependent structural changes in planar bilayer membranes: Solvent "freeze-out".* 1974. **356**(1): p. 8-16.
76. White, S.J.B.j., *Formation of" solvent-free" black lipid bilayer membranes from glyceryl monooleate dispersed in squalene.* 1978. **23**(3): p. 337-347.
77. Neher, E.J.B.e.B.A.-B., *Asymmetric membranes resulting from the fusion of two black lipid bilayers.* 1974. **373**(3): p. 327-336.
78. Wiese, A., et al., *Planar asymmetric lipid bilayers of glycosphingolipid or lipopolysaccharide on one side and phospholipids on the other: membrane potential, porin function, and complement activation.* 1996. **70**(1): p. 321-329.

79. Van Gelder, P., F. Dumas, and M.J.B.c. Winterhalter, *Understanding the function of bacterial outer membrane channels by reconstitution into black lipid membranes.* 2000. **85**(2-3): p. 153-167.
80. Sun, Y., et al., *Lipid membranes supported by planar porous substrates.* 2020. **228**: p. 104893.
81. Beltramo, P.J., R. Van Hooghten, and J.J.S.M. Vermant, *Millimeter-area, free standing, phospholipid bilayers.* 2016. **12**(19): p. 4324-4331.
82. Liu, P., O. Zabala-Ferrera, and P.J.J.b. Beltramo, *Fabrication and electromechanical characterization of free-standing asymmetric membranes.* 2020.
83. Jeon, T.-J., et al., *Black lipid membranes stabilized through substrate conjugation to a hydrogel.* 2008. **3**(2): p. FA96-FA100.
84. Gómez-Lagunas, F., et al., *Incorporation of ionic channels from yeast plasma membranes into black lipid membranes.* 1989. **56**(1): p. 115-119.
85. Geng, J., et al., *Stochastic transport through carbon nanotubes in lipid bilayers and live cell membranes.* 2014. **514**(7524): p. 612-615.
86. Groves, J.T., N. Ulman, and S.G.J.S. Boxer, *Micropatterning fluid lipid bilayers on solid supports.* 1997. **275**(5300): p. 651-653.
87. Su, H., et al., *Facile generation of biomimetic-supported lipid bilayers on conducting polymer surfaces for membrane biosensing.* 2019. **11**(47): p. 43799-43810.
88. Tamm, L.K. and H.M.J.B.j. McConnell, *Supported phospholipid bilayers.* 1985. **47**(1): p. 105.
89. Reimhult, E., F. Höök, and B.J.L. Kasemo, *Intact vesicle adsorption and supported biomembrane formation from vesicles in solution: influence of surface chemistry, vesicle size, temperature, and osmotic pressure.* 2003. **19**(5): p. 1681-1691.
90. Kalb, E., S. Frey, and L.K.J.B.e.B.A.-B. Tamm, *Formation of supported planar bilayers by fusion of vesicles to supported phospholipid monolayers.* 1992. **1103**(2): p. 307-316.
91. Zasadzinski, J.A., et al., *Atomic force microscopy of hydrated phosphatidylethanolamine bilayers.* 1991. **59**(3): p. 755-760.
92. Egawa, H. and K.J.L. Furusawa, *Liposome adhesion on mica surface studied by atomic force microscopy.* 1999. **15**(5): p. 1660-1666.
93. Bunjes, N., et al., *Thiopeptide-supported lipid layers on solid substrates.* 1997. **13**(23): p. 6188-6194.
94. Lahiri, J., et al., *Method for fabricating supported bilayer lipid membranes on gold.* 2000. **16**(20): p. 7805-7810.
95. Salamon, Z., et al., *Assembly and molecular organization of self-assembled lipid bilayers on solid substrates monitored by surface plasmon resonance spectroscopy.* 1994. **1195**(2): p. 267-275.
96. Lagerholm, B.C., et al., *Rebinding of IgE Fabs at haptenated planar membranes: measurement by total internal reflection with fluorescence photobleaching recovery.* 2000. **39**(8): p. 2042-2051.
97. Cremer, P.S. and S.G.J.T.J.o.P.C.B. Boxer, *Formation and spreading of lipid bilayers on planar glass supports.* 1999. **103**(13): p. 2554-2559.
98. Hillebrandt, H., et al., *High Electric Resistance Polymer/Lipid Composite Films on Indium− Tin− Oxide Electrodes.* 1999. **15**(24): p. 8451-8459.

99. Gritsch, S., et al., *Impedance Spectroscopy of Porin and Gramicidin Pores Reconstituted into Supported Lipid Bilayers on Indium− Tin-Oxide Electrodes.* 1998. **14**(11): p. 3118-3125.
100. Johnson, S.J., et al., *Structure of an adsorbed dimyristoylphosphatidylcholine bilayer measured with specular reflection of neutrons.* 1991. **59**(2): p. 289-294.
101. Kühner, M., R. Tampe, and E.J.B.j. Sackmann, *Lipid mono-and bilayer supported on polymer films: composite polymer-lipid films on solid substrates.* 1994. **67**(1): p. 217-226.
102. Sackmann, E. and M.J.T.i.b. Tanaka, *Supported membranes on soft polymer cushions: fabrication, characterization and applications.* 2000. **18**(2): p. 58-64.
103. Wagner, M.L. and L.K.J.B.j. Tamm, *Tethered polymer-supported planar lipid bilayers for reconstitution of integral membrane proteins: silane-polyethyleneglycol-lipid as a cushion and covalent linker.* 2000. **79**(3): p. 1400-1414.
104. Renner, L., et al., *Controlled enhancement of transmembrane enzyme activity in polymer cushioned supported bilayer membranes.* 2010. **6**(21): p. 5382-5389.
105. Wong, J.Y., et al., *Polymer-cushioned bilayers. I. A structural study of various preparation methods using neutron reflectometry.* 1999. **77**(3): p. 1445-1457.
106. Cornell, B.A., et al., *A biosensor that uses ion-channel switches.* 1997. **387**(6633): p. 580-583.
107. Rossi, C. and J.J.E.B.J. Chopineau, *Biomimetic tethered lipid membranes designed for membrane-protein interaction studies.* 2007. **36**(8): p. 955-965.
108. Majewski, J., et al., *Structural studies of polymer-cushioned lipid bilayers.* 1998. **75**(5): p. 2363-2367.
109. Zhang, L., M.L. Longo, and P.J.L. Stroeve, *Mobile phospholipid bilayers supported on a polyion/alkylthiol layer pair.* 2000. **16**(11): p. 5093-5099.
110. Naumann, C.A., et al., *The polymer-supported phospholipid bilayer: Tethering as a new approach to substrate− membrane stabilization.* 2002. **3**(1): p. 27-35.
111. Vockenroth, I.K., et al., *Stable insulating tethered bilayer lipid membranes.* 2008. **3**(2): p. FA68-FA73.
112. Vockenroth, I.K., et al., *Tethered bilayer lipid membranes with giga-ohm resistances.* 2008. **10**(2): p. 323-328.
113. Andersson, M., et al., *Detection of single ion channel activity on a chip using tethered bilayer membranes.* 2007. **23**(6): p. 2924-2927.
114. Becucci, L., et al., *Tethered bilayer lipid micromembranes for single-channel recording: the role of adsorbed and partially fused lipid vesicles.* 2011. **13**(29): p. 13341-13348.
115. Zhang, Y., et al., *Supported lipid bilayer assembly on PEDOT: PSS films and transistors.* 2016. **26**(40): p. 7304-7313.
116. Tanaka, M. and E.J.N. Sackmann, *Polymer-supported membranes as models of the cell surface.* 2005. **437**(7059): p. 656-663.
117. Stelzle, M., G. Weissmüller, and E.J.T.J.o.P.C. Sackmann, *On the application of supported bilayers as receptive layers for biosensors with electrical detection.* 1993. **97**(12): p. 2974-2981.

118. Kibrom, A., et al., *Hydrogel-supported protein-tethered bilayer lipid membranes: a new approach toward polymer-supported lipid membranes.* 2011. **7**(1): p. 237-246.
119. Ren, X., et al., *Stability of free-standing tetraether planar membranes in microchips.* 2017. **540**: p. 27-34.
120. Coronado, R. and R.J.B.j. Latorre, *Phospholipid bilayers made from monolayers on patch-clamp pipettes.* 1983. **43**(2): p. 231-236.
121. Matsuno, Y., et al., *Single-channel recordings of gramicidin at agarose-supported bilayer lipid membranes formed by the tip-dip and painting methods.* 2004. **20**(8): p. 1217-1221.
122. Shoji, K., R. Kawano, and R.J.J.A.C. White, *Recessed Ag/AgCl Microelectrode-Supported Lipid Bilayer for Nanopore Sensing.* 2020. **92**(15): p. 10856-10862.
123. Okuno, D., et al., *A Simple Method for Ion Channel Recordings Using Fine Gold Electrode.* 2016. **32**(12): p. 1353-1357.
124. Shoji, K., R. Kawano, and R.J.J.A.n. White, *Spatially Resolved Chemical Detection with a Nanoneedle-Probe-Supported Biological Nanopore.* 2019. **13**(2): p. 2606-2614.
125. Hirano, M., et al., *A Lipid Bilayer Formed on a Hydrogel Bead for Single Ion Channel Recordings.* 2020. **11**(12): p. 1070.
126. Challita, E.J. and E.C.J.L. Freeman, *Hydrogel Microelectrodes for the Rapid, Reliable, and Repeatable Characterization of Lipid Membranes.* 2018. **34**(50): p. 15166-15173.
127. Tsofina, L., E. Liberman, and A.J.N. Babakov, *Production of bimolecular protein-lipid membranes in aqueous solution.* 1966. **212**(5063): p. 681-683.
128. Tien, H.T., *Bilayer lipid membranes (BLM): theory and practice*. 1974: M. Dekker.
129. Seddon, J. and R. Templer, *Polymorphism of lipid-water systems*, in *Handbook of biological physics*. 1995, Elsevier. p. 97-160.
130. Thompson, J.R., et al., *Enhanced stability and fluidity in droplet on hydrogel bilayers for measuring membrane protein diffusion.* Nano letters, 2007. **7**(12): p. 3875-3878.
131. Heron, A.J., et al., *Direct detection of membrane channels from gels using water-in-oil droplet bilayers.* Journal of the American Chemical Society, 2007. **129**(51): p. 16042-16047.
132. Leptihn, S., et al., *Constructing droplet interface bilayers from the contact of aqueous droplets in oil.* 2013. **8**(6): p. 1048-1057.
133. Bayley, H., et al., *Droplet interface bilayers.* Mol Biosyst, 2008. **4**(12): p. 1191-208.
134. Funakoshi, K., H. Suzuki, and S. Takeuchi, *Lipid bilayer formation by contacting monolayers in a microfluidic device for membrane protein analysis.* Analytical chemistry, 2006. **78**(24): p. 8169-8174.
135. Poulin, P. and J. Bibette, *Adhesion of water droplets in organic solvent.* Langmuir, 1998. **14**(22): p. 6341-6343.
136. El-Beyrouthy, J., et al., *A new approach for investigating the response of lipid membranes to electrocompression by coupling droplet mechanics and membrane biophysics.* Journal of the Royal Society Interface, 2019. **16**(161): p. 20190652.

137. Taylor, G.J., et al., *Direct in situ measurement of specific capacitance, monolayer tension, and bilayer tension in a droplet interface bilayer.* Soft Matter, 2015. **11**(38): p. 7592-605.
138. Taylor, G., et al., *Electrophysiological interrogation of asymmetric droplet interface bilayers reveals surface-bound alamethicin induces lipid flip-flop.* Biochimica et Biophysica Acta (BBA)-Biomembranes, 2018.
139. Makhoul-Mansour, M., et al., *Ferrofluid-Based Droplet Interface Bilayer Networks.* Langmuir, 2017. **33**(45): p. 13000-13007.
140. Makhoul-Mansour, M.M. and E.C.J.L. Freeman, *Droplet-Based Membranous Soft Materials.* 2021.
141. Korner, J.L., E.B. Stephenson, and K.S.J.L.o.a.C. Elvira, *A bespoke microfluidic pharmacokinetic compartment model for drug absorption using artificial cell membranes.* 2020. **20**(11): p. 1898-1906.
142. Berry, J.D., et al., *Measurement of surface and interfacial tension using pendant drop tensiometry.* J Colloid Interface Sci, 2015. **454**: p. 226-37.
143. Rofeh, J. and L.J.S.M. Theogarajan, *Instantaneous tension measurements in droplet interface bilayers using an inexpensive, integrated pendant drop camera.* 2020. **16**(18): p. 4484-4493.
144. Schoch, P., D.F. Sargent, and R. Schwyzer, *Capacitance and conductance as tools for the measurement of asymmetric surface potentials and energy barriers of lipid bilayer membranes.* The Journal of Membrane Biology, 1979. **46**(1): p. 71-89.
145. Alvarez, O. and R. Latorre, *Voltage-dependent capacitance in lipid bilayers made from monolayers.* Biophysical journal, 1978. **21**(1): p. 1-17.
146. Cevc, G., *Membrane electrostatics.* Biochimica et Biophysica Acta (BBA)-Reviews on Biomembranes, 1990. **1031**(3): p. 311-382.
147. Huang, W.-T. and D.G.J.B.j. Levitt, *Theoretical calculation of the dielectric constant of a bilayer membrane.* 1977. **17**(2): p. 111-128.
148. Toyama, S., A. Nakamura, and F. Toda, *Measurement of voltage dependence of capacitance of planar bilayer lipid membrane with a patch clamp amplifier.* Biophysical journal, 1991. **59**(4): p. 939-944.
149. Muller, N. and R.H.J.T.J.o.P.C. Birkhahn, *Investigation of micelle structure by fluorine magnetic resonance. I. Sodium 10, 10, 10-trifluorocaprate and related compounds.* 1967. **71**(4): p. 957-962.
150. Sekiya, Y., et al., *Electrophysiological analysis of membrane disruption by bombinin and its isomer using the lipid bilayer system.* 2019. **2**(4): p. 1542-1548.
151. Cherny, V., V.S. Sokolov, and I.G. Abidor, *330-Determination of surface charge of bilayer lipid membranes.* Bioelectrochemistry and Bioenergetics, 1980. **7**(3): p. 413-420.
152. Brockman, H.J.C. and p.o. lipids, *Dipole potential of lipid membranes.* 1994. **73**(1-2): p. 57-79.
153. Clarke, R.J.J.A.i.c. and i. science, *The dipole potential of phospholipid membranes and methods for its detection.* 2001. **89**: p. 263-281.
154. Wang, L.J.A.r.o.b., *Measurements and implications of the membrane dipole potential.* 2012. **81**: p. 615-635.

155. Makhoul-Mansour, M.M., et al., *Photopolymerized microdomains in both lipid leaflets establish diffusive transport pathways across biomimetic membranes*. 2019. **15**(43): p. 8718-8727.
156. Bergeron, V., *Force and structure in thin liquid soap film* 1999.
157. Dey, R., S. DasGupta, and S. Chakraborty, *Electrowetting of sessile drops on soft dielectric elastomer films*. Microfluidics and Nanofluidics, 2017. **21**(3).
158. Najem, J.S., et al., *Activation of bacterial channel MscL in mechanically stimulated droplet interface bilayers*. Sci Rep, 2015. **5**: p. 13726.
159. Moghaddam, M.M., et al., *The development of antimicrobial peptides as an approach to prevention of antibiotic resistance.* Reviews in Medical Microbiology, 2015. **26**(3): p. 98-110.
160. Jenssen, H., P. Hamill, and R.E. Hancock, *Peptide antimicrobial agents.* Clinical microbiology reviews, 2006. **19**(3): p. 491-511.
161. Hancock, R.E. and A. Rozek, *Role of membranes in the activities of antimicrobial cationic peptides.* FEMS microbiology letters, 2002. **206**(2): p. 143-149.
162. Christensen, B., et al., *Channel-forming properties of cecropins and related model compounds incorporated into planar lipid membranes.* 1988. **85**(14): p. 5072-5076.
163. Kagan, B.L., et al., *Antimicrobial defensin peptides form voltage-dependent ion-permeable channels in planar lipid bilayer membranes.* 1990. **87**(1): p. 210-214.
164. Coronado, R., R.L. Rosenberg, and C.J.T.J.o.g.p. Miller, *Ionic selectivity, saturation, and block in a K+-selective channel from sarcoplasmic reticulum.* 1980. **76**(4): p. 425-446.
165. Ashrafuzzaman, M., O. Andersen, and R.J.B.e.B.A.-B. McElhaney, *The antimicrobial peptide gramicidin S permeabilizes phospholipid bilayer membranes without forming discrete ion channels.* 2008. **1778**(12): p. 2814-2822.
166. Michalak, Z., et al., *Effect of monoglyceride structure and cholesterol content on water permeability of the droplet bilayer*. Langmuir, 2013. **29**(51): p. 15919-25.
167. Milianta, P.J., et al., *Water Permeability across Symmetric and Asymmetric Droplet Interface Bilayers: Interaction of Cholesterol Sulfate with DPhPC.* Langmuir, 2015. **31**(44): p. 12187-96.
168. Mansour, M.M.M., et al., *A skin-inspired soft material with directional mechanosensation.* 2021.
169. de Planque, M.R., et al., *Electrophysiological characterization of membrane disruption by nanoparticles.* 2011. **5**(5): p. 3599-3606.
170. Punnamaraju, S., H. You, and A.J.L. Steckl, *Triggered release of molecules across droplet interface bilayer lipid membranes using photopolymerizable lipids.* 2012. **28**(20): p. 7657-7664.
171. Quilliet, C. and B. Berge, *Electrowetting: a recent outbreak.* Current Opinion in Colloid & Interface Science, 2001. **6**(1): p. 34-39.
172. Mugele, F. and J.-C. Baret, *Electrowetting: from basics to applications.* Journal of Physics: Condensed Matter, 2005. **17**(28): p. R705-R774.
173. Trick, J.L., et al., *Voltage gating of a biomimetic nanopore: electrowetting of a hydrophobic barrier*. 2017. **11**(2): p. 1840-1847.
174. Martel, A. and B.J.B. Cross, *Handling of artificial membranes using electrowetting-actuated droplets on a microfluidic device combined with integrated pA-measurements.* 2012. **6**(1): p. 012813.

175. Fan, S.-K., et al., *Formation of suspended bilayer lipid membrane between electrowetting-driven encapsulated droplets.* 2014. **8**(5): p. 052006.
176. Sarles, S.A. and D.J.J.L.o.a.C. Leo, *Physical encapsulation of droplet interface bilayers for durable, portable biomolecular networks.* 2010. **10**(6): p. 710-717.
177. Sarles, S.A., D.J.J.J.o.i.m.s. Leo, and structures, *Tailored current—voltage relationships of droplet-interface bilayers using biomolecules and external feedback control.* 2009. **20**(10): p. 1233-1247.
178. Kancharala, A., et al., *A comprehensive flexoelectric model for droplet interface bilayers acting as sensors and energy harvesters.* 2016. **25**(10): p. 104007.
179. Punnamaraju, S. and A.J.J.L. Steckl, *Voltage control of droplet interface bilayer lipid membrane dimensions.* 2011. **27**(2): p. 618-626.
180. Lin, S.-Y., et al., *An examination on the accuracy of interfacial tension measurement from pendant drop profiles.* Langmuir, 1995. **11**(10): p. 4159-4166.
181. Najem, J.S., et al., *Dynamical nonlinear memory capacitance in biomimetic membranes.* 2019. **10**(1): p. 1-11.
182. Sokolov, V. and V.J.B. Kuz'min, *Measurement of the difference in the surface potentials of bilayer membranes from the second harmonic of the capacitance current.* 1980. **25**(1): p. 174-177.
183. Pohl, E.E., et al., *Changes of intrinsic membrane potentials induced by flip-flop of long-chain fatty acids.* Biochemistry, 2000. **39**(7): p. 1834-1839.
184. Sokolov, V., et al., *Voltage-sensitive styryl dyes as singlet oxygen targets on the surface of bilayer lipid membrane.* 2016. **161**: p. 162-169.
185. Passechnik, V.I. and V.S.J.B. Sokolov, *Estimation of electrochrome dyes position in the bilayer through the 2nd harmonic of capacitive current.* 2002. **55**(1-2): p. 47-51.
186. Mirsky, V.M., *Ultrathin electrochemical chemo-and biosensors: technology and performance*. Vol. 2. 2013: Springer Science & Business Media.
187. Passechnik, V.I., *Estimates of the intramembrane field through the harmonics of capacitive current in inhomogeneous bilayer lipid membranes.* Bioelectrochemistry, 2001. **54**(1): p. 63-73.
188. El-Beyrouthy, J. and E.C. Freeman. *Rapid and Real-Time Measurement of Membrane Potential Through Intramembrane Field Compensation*. in *Smart Materials, Adaptive Structures and Intelligent Systems*. 2020. American Society of Mechanical Engineers.
189. Freeman, E.C., et al., *The mechanoelectrical response of droplet interface bilayer membranes.* Soft Matter, 2016. **12**(12): p. 3021-31.
190. Najem, J.S., S. Sukharev, and D.J. Leo, *The Effect of Transmembrane Potential on the Gating of MscL Channels in Droplet Interface Bilayers.* 2016: p. V002T06A012.
191. Coster, H.G., et al., *Impedance spectroscopy of interfaces, membranes and ultrastructures.* 1996. **40**(2): p. 79-98.
192. Newman, J. and K.E. Thomas-Alyea, *Electrochemical systems*. 2012: John Wiley & Sons.
193. Chang, B.-Y. and S.-M.J.A.R.o.A.C. Park, *Electrochemical impedance spectroscopy.* 2010. **3**: p. 207-229.

194. Römer, W. and C.J.B.j. Steinem, *Impedance analysis and single-channel recordings on nano-black lipid membranes based on porous alumina.* 2004. **86**(2): p. 955-965.
195. Coster, H. and J. Smith, *The molecular organization of bimolecular lipid membranes. A study of the low frequency Maxwell-Wagner impedance dispersion.* Biochimica et Biophysica Acta (BBA)-Biomembranes, 1974. **373**(2): p. 151-164.
196. Raila, T., et al., *Clusters of protein pores in phospholipid bilayer membranes can be identified and characterized by electrochemical impedance spectroscopy.* 2020. **364**: p. 137179.
197. Wu, Z., et al., *Ion channel behavior of supported bilayer lipid membranes on a glassy carbon electrode.* 2000. **72**(24): p. 6030-6033.
198. Steinem, C., et al., *Impedance analysis of supported lipid bilayer membranes: a scrutiny of different preparation techniques.* 1996. **1279**(2): p. 169-180.
199. Valincius, G., T. Meškauskas, and F.J.L. Ivanauskas, *Electrochemical impedance spectroscopy of tethered bilayer membranes.* 2012. **28**(1): p. 977-990.
200. Alobeedallah, H., B. Cornell, and H. Coster, *The Effect of Cholesterol on the Dielectric Structure of Lipid Bilayers.* The Journal of membrane biology, 2018. **251**(1): p. 153-161.
201. Alobeedallah, H., B. Cornell, and H. Coster, *The effect of benzyl alcohol on the dielectric structure of lipid bilayers.* The Journal of membrane biology, 2016. **249**(6): p. 833-844.
202. Terrettaz, S., M. Mayer, and H.J.L. Vogel, *Highly electrically insulating tethered lipid bilayers for probing the function of ion channel proteins.* 2003. **19**(14): p. 5567-5569.
203. Karolis, C., et al., *Differential effects of cholesterol and oxidised-cholesterol in egg lecithin bilayers.* Biochimica et Biophysica Acta (BBA)-Biomembranes, 1998. **1368**(2): p. 247-255.
204. Korman, C.E., et al., *Nanopore-spanning lipid bilayers on silicon nitride membranes that seal and selectively transport ions.* 2013. **29**(14): p. 4421-4425.
205. Sarangi, N.K., A. Stalcup, and T.E.J.C. Keyes, *The impact of membrane composition and co-drug synergistic effects on vancomycin association with model membranes from electrochemical impedance spectroscopy.* 2020. **7**(22): p. 4535-4542.
206. Fujino, Y., et al., *Electrochemical impedance spectroscopy study of liposome adsorption and rupture on self-assembled monolayer: Effect of surface charge.* 2020. **878**: p. 114572.

# CHAPTER 3

# A NEW APPROACH FOR INVESTIGATING THE RESPONSE OF LIPID MEMBRANES TO ELECTROCOMPRESSION BY COUPLING DROPLET MECHANICS AND MEMBRANE BIOPHYSICS [2]

[2] El-Beyrouthy, J., et al. (2019). "A new approach for investigating the response of lipid membranes to electrocompression by coupling droplet mechanics and membrane biophysics." Journal of the Royal Society Interface **16**(161): 20190652.
Reprinted with the permission of publisher.

## Abstract

A new method for quantifying the effects of lipid frustration within model lipid bilayer membranes is demonstrated, coupling droplet mechanics and membrane biophysics. Lipid frustration is achieved by introducing cholesterol into lipid bilayers, generating an unfavourable lateral packing or reduction in area per lipid. Pendant drop tensiometry is used to measure lipid monolayer tensions at an oil-water interface with increasing cholesterol mole fractions. Next, two lipid-coated aqueous droplets are manipulated into contact to form a membrane at their adhered interface. The droplet geometry is captured from two angles to provide measurements of both the membrane area and the contact angle of the droplets. Combining the monolayer tension and contact angle measurements enables estimations of the bilayer tension with respect to composition. Next the membrane is electromechanically compressed. Electrostatic pressure, membrane tension, and the work necessary for bilayer thinning are tracked, and a model is proposed to capture the mechanics of membrane compression. The results highlight that an energetic term is produced during compression, reflecting changes in the lateral membrane structure. This residual energy is eliminated in cases with cholesterol mole fractions of 0.2 and higher, suggesting that cholesterol restricts adjustments in the lateral membrane structure.

## Introduction

Cellular organisms are surrounded by semi-permeable membranes that differentiate the cytoplasm and the extracellular fluid [1]. These membranes consist primarily of a double layer of amphiphilic phospholipids. Additional biomolecules are interwoven between the lipids, including proteins and sterols. The membrane composition varies by cellular functionality and location, suggesting that the lipid composition is adapted based on the requirements of the cell [2-4]. Furthermore, biological membranes contain multiple lipid types with varying properties [5] which in turn influence the properties of the membrane as a whole [6, 7]. One such property is the innate curvature or shape factor of the lipids produced by imbalances between the hydrophilic and hydrophobic groups [8, 9]. Different lipids packed together within the membrane reach a mutually agreeable configuration where many lipids are frustrated or out of equilibrium due to their inability to achieve their desired shape [10], producing energetic penalties [11].

These lipid-lipid interactions have been proposed as mechanisms for membrane trafficking [12] and for aiding phenomena such as membrane fusion and fission processes [13-15]. The membrane is able to distribute lipids in such a fashion to accommodate its own reshaping, which minimizes the necessary mechanical effort expense. Consequently, quantifying lipid-lipid interactions in membranes is crucial to better understanding cellular biophysics. Model membranes approximating cellular membranes have been created through various techniques with the purpose of studying biological processes in a controlled environment, but these are often not well-suited for directly quantifying these lipid-lipid interactions. This shortcoming is addressed here through a combination of

tensiometry, and electrophysiology measurements of lipid bilayers assembled via the droplet interface bilayer (DIB) technique [16-18].

In the DIB approach lipids are used as surfactants in a water-in-oil mixture, coating aqueous droplets in lipid monolayers. Manipulating lipid-coated droplets into contact within an oil reservoir spontaneously forms a lipid bilayer at their adhered interface, coupling membrane mechanics and adhesive droplet mechanics. This coupling allows for new investigations on membrane properties such as the impact of lipid-lipid interactions involved in lipid frustration by studying changes in the membrane tension with varying conditions.

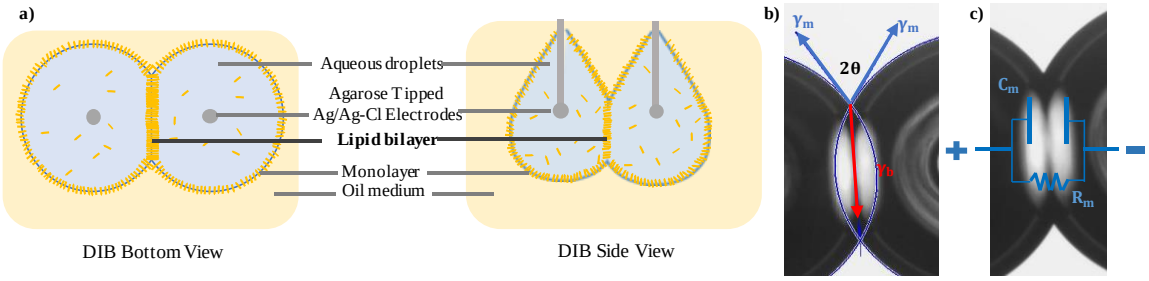


Figure 3.1: The DIB technique is used to create lipid membranes. a) DIB schematic showing the two droplets submerged in oil from two angles. Lipid monolayers are assembled at the water-oil interfaces. The lipid bilayer is formed at the interface of the two adhered droplets. b) Sum of the surface tensions at the annulus predicts the apparent bilayer tension based on the monolayer surface tension and the contact angle. c) The electrical model of the membrane consists of a capacitor and a resistor in parallel.

Figure 3.1 (a) shows two aqueous droplets submerged in oil, producing a lipid bilayer at their adhered interface. Lipids are dispersed in the aqueous phase, [19] and align and unfold at the water-oil interface to form the lipid monolayer. Monolayer stabilization takes several minutes dependent on the droplet size and selected oil [20]. The lipid bilayer is formed as the lipid-coated droplets are brought into contact, expelling the residual solvent between them. The growth of the bilayer is controlled by the equilibrium of tensions acting at the triple point, minimizing the total interfacial energy of the adhered

droplets pair (Figure 3.1 (b)) as described by an appropriate form of Young's equation (Equation (3.1)), linking the tensions to the measured contact angle. These tensions are dependent on the relative favourability of interface formation as well as the area per surfactant molecule [21]. An advantage of DIBs is the ability to estimate the lipid bilayer membrane tension or energy per area visually from the geometry of the connected droplets when both droplets have an equal composition using Young's equation [22-24]:

$$\gamma_b = 2\gamma_b \cos\theta \tag{3.1}$$

where $\gamma_b$ is the bilayer tension (mN/m), $\gamma_m$ is the monolayer surface tension (mN/m) and $\theta$ is half the angle between the two droplets.

The thermodynamic favourability of the bilayer formation is quantified by the energy of adhesion [18], which compares the bilayer tension to the two monolayer tensions (Equation (3.2)). The greater the energy of adhesion, the more favourable the formation of the bilayer. Thus, the adhesion energy reflects how much energy the system conserves per unit area by forming a as described by the Young – Dupre equation as the difference between the adhered bilayer tension and the original two monolayer tensions [25]:

$$\varepsilon = 2\gamma_m - \gamma_b = 2\gamma_m(1 - \cos\theta) \tag{3.2}$$

where $\varepsilon$ is the energy of adhesion per membrane area (mN/m). A positive adhesion energy allows for the favourable replacement of the monolayer areas of the two droplets with a single bilayer area.

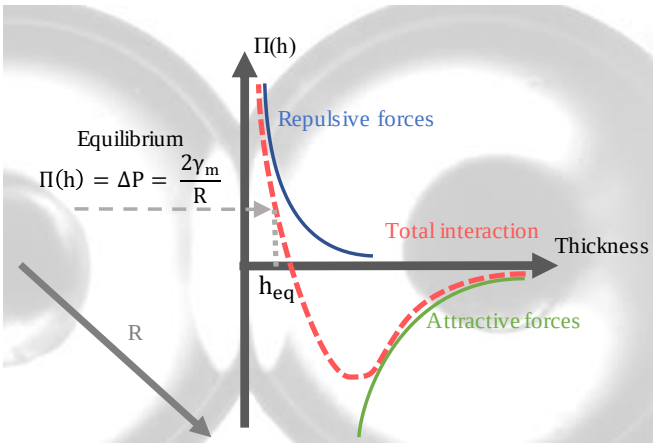


Figure 3.2: A sketch of the disjoining pressure versus the bilayer thickness. Attractive and repulsive forces act at the bilayer as a function of its thickness [26, 27]. At a relatively high thickness, molecular attractive forces pull the two leaflets close until steric repulsion balances the attraction and stabilizes the thin film at an equilibrium thickness. This equilibrium thickness is then defined where the disjoining pressure is balanced by the Laplace pressure.

The adhesion energy can also be defined as the integral over separation distance ($h$) of disjoining pressure ($\Pi$, Figure 3.2) from infinity to the equilibrium thickness ($h_{eq}$) [27-32]:

$$\varepsilon = \int_{\infty}^{h_{eq}} \Pi(h)dh \qquad (3.3).$$

Here we have defined the energy of adhesion as a positive value for adhesive systems. The disjoining pressure is the sum of multiple attractive and repulsive forces acting simultaneously on the thin film as a function of the distance $h$ between the leaflets. At a relatively high thickness, the attractive forces are dominant and drive the leaflets closer together. Once the thin film reaches an approximate thickness of ~5 nm [26], steric repulsions between the opposing leaflets begin to counteract the attraction until an equilibrium thickness is attained. In the DIB scenario, equilibrium is reached when the disjoining pressure in the thin film matches the Laplace pressure inside the droplets, as

illustrated in Figure 3.2. Thus, any supplied additional pressures that compress the bilayer below this equilibrium thickness will be further resisted through steric repulsion [33]. Combining Equation (3.3) with Equation (3.2) produces:

$$\gamma_b = 2\gamma_m - \int_{\infty}^{h_{eq}} \Pi(h)dh \qquad (3.4)$$

which describes how the bilayer tension varies as the membrane thins from a relatively infinite separation ($h = \infty$) to the equilibrium thickness determined by the balance of forces between the droplet surfaces, as shown in Figure 3.2 [27, 34]. With droplet-droplet adhesion in DIBs, the contact angle and droplet dimensions are sufficiently large to render contributions from film thickness and monolayer line tensions negligible [29].

Based on these physics, measuring changes in bilayer tension ($\gamma_b$) caused by alterations in membrane composition provides a new capability to assess lipid-lipid interactions. In this work the equilibrium monolayer tension ($\gamma_m$) was measured using the pendant drop approach [35], and the angle of contact between the droplets at equilibrium was used to compute bilayer tension (Equation (3.1)). Changes in the geometry of the droplet pair as well as in the electrical characteristics of the membrane are translated into changes in the structuring of molecules within the bilayer, recognizing that unfavourable interactions between the lipids are manifested as increases in the membrane energy per area or interfacial tension.

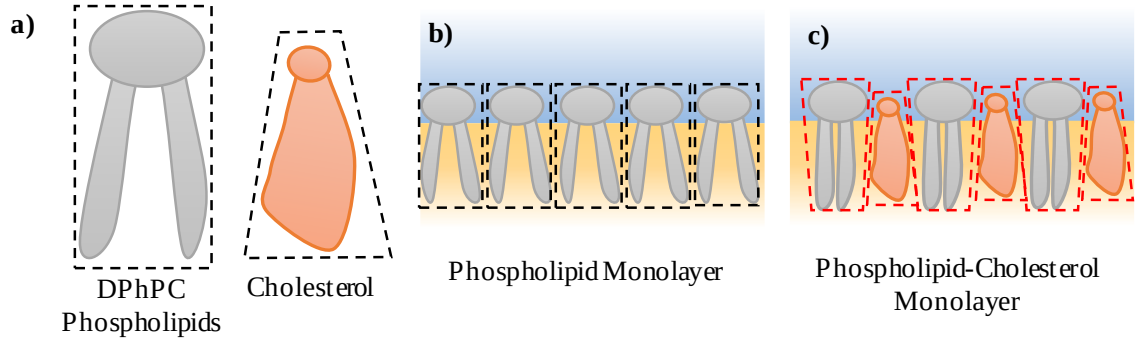


Figure 3.3: a) Illustrative comparison of phospholipid and cholesterol molecules. Cholesterol molecules possess a small hydrophilic region compared to its large hydrophobic one. b) At a water-oil surface, and due to their amphiphilic properties, phospholipids assemble at the interface and form the monolayer with minimal complications or distortion. c) Cholesterol incorporated into the monolayer causes deformation of the surrounding lipids and produces energetic penalties which manifests as changes in the surface tension or energy per area.

The impact of cholesterol on DPhPC membranes undergoing electrocompression is investigated here. DPhPC (1,2-diphytanoyl-sn-glycero-3-phosphocholine) is a synthetically formed phospholipid that is often used for DIBs [20, 36, 37]. DPhPC does not exhibit a phase transition from -120°C to 120°C [38], rendering the lipids temperature-invariant and its low spontaneous curvature provides a stable planar membrane [15]. In contrast, cholesterol does not self-assemble into vesicles or sheets when dispersed in an aqueous solution, preferring crystallization [5]. This is because cholesterol possesses a very low hydrophilic/hydrophobic ratio as depicted in Figure 3.3 (a), producing a cone shaped structure and a strong negative spontaneous curvature relative to DPhPC.

When cholesterol-laden lipid vesicles are introduced to a polar-apolar interface, cholesterol is dispersed between the phospholipids at the interface but struggles to limit unfavourable water-hydrophobic interactions without additional aid. Thus, mixtures of phospholipids and cholesterols adjust in a manner that minimizes these unfavourable interactions (Figure 3.3 (c)). Cholesterol molecules insert between the phospholipids,

finding the gaps in the surface and leading to a more condensed monolayer by limiting the motions of the phospholipids' hydrophobic tails, influencing the membrane structure. This is expected to produce energetic penalties associated with the frustration of the desired lateral spread of the lipids which will cause changes in the interfacial tension of the interface. Changes in the interfacial energetics and response to compression will be tracked as a function of cholesterol mole ratio.

This research is enabled by simultaneously measuring the lipid membrane area ($A_m$) and contact angle ($\theta$) between the droplets. While precise measurements of membrane area have been achieved using a droplet hydrogel bilayer (DHB) [23] and precise measurements of the angle of contact have been achieved using traditional DIBs [24], calibration factors or assumptions on the geometry were employed in both approaches to account for gravitational influences when estimating the remaining values. Here, a dual-view approach is used to provide simultaneous characterization of membrane area and contact angle without requiring additional assumptions allowing for greater clarity in the desired measurements. This clarity allows for a thorough investigation of the membrane properties, uncovering additional phenomena.

## Materials and methods

### Solution preparations

Lipid-in solutions were used in all the described experiments, where lipids are dispersed in the aqueous phases [20]. Buffer solutions (500 mM potassium chloride (KCl, ≥ 99.1% – Sigma-Aldrich), 10 mM of 3-(N-Morpholino) propane sulfonic acid (MOPS, ≥ 99.5% – Sigma-Aldrich), Sigma Aldrich) were prepared and then mixed with DPhPC (1,2-diphytanoyl-sn-glycero-3-phosphocholine – Avanti Polar Lipids) and cholesterol (ovine

wool, >98% – Avanti Polar Lipids) based on the desired mole fractions and following the protocol described in Appendix A, section A.1. Solutions were prepared with 0, 10, 20, and 30% mole fraction cholesterol in DPhPC. The maximum cholesterol mole fraction used in this work was 30%, ensuring cholesterol solubility in phospholipids and avoiding precipitation of cholesterol crystals [39-41]. Hexadecane (99% – Sigma-Aldrich) was used for the oil phase, as it has shown to produce stable bilayers in addition to its relatively large molecule enabling the assumption of a solvent-free model membrane in comparison to shorter-chain alkanes, such as decane [23, 42].

**Monolayer surface tension measurements**

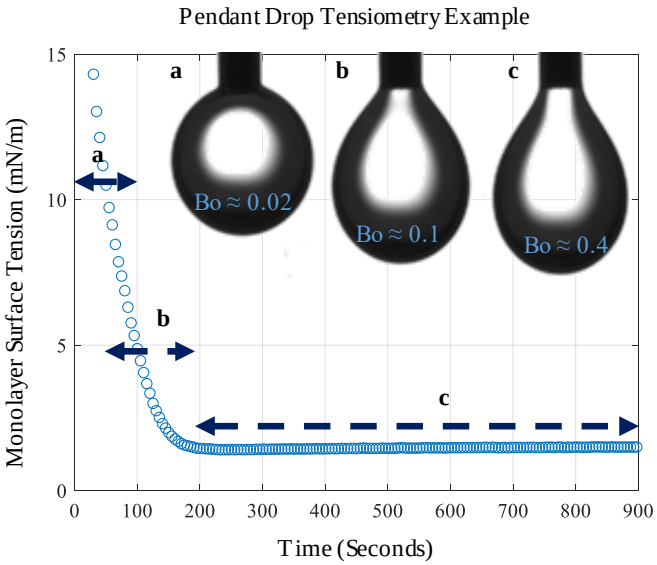


Figure 3.4: The pendant drop technique was used to quantify the monolayer surface tension. a) Initially, surface tension is dominant, leading to a sphere-shaped droplet. b) As lipids begin coating the interface, the surface tension is reduced, and gravitational effects become more significant. c) After a few minutes, equilibrium is reached where surface tension and gravity are in balance, and the interfacial tension can be accurately estimated from the droplet pendant shape.

Monolayer surface tensions were measured using the pendant drop technique [35]. An aqueous droplet is suspended from a needle inside a glass cuvette containing

hexadecane. Once the droplet is introduced to the oil reservoir, lipid molecules migrate towards the water-oil interface forming the monolayer and decreasing the surface tension. The droplet gradually sags from a spherical shape to a pendant shape and the monolayer tension can then be estimated (Figure 3.4). The process is recorded using a zoom lens camera (6.5X zoom lenses with a 0.7−4.5× magnification range, Thorlabs). Droplet images are used to obtain the interfacial tension using the open-source tensiometry software OpenDrop [35, 43]. The capability to vary the needle dimensions and magnification allows for the assessment of low surface tension cases which otherwise would be problematic. After the lipid monolayer is established the tension reaches a steady-state value and minimal drift is observed as shown in Figure 3.4. Additional experimental details can be found in Appendix A, section A.2.

**DIB creation and characterization**

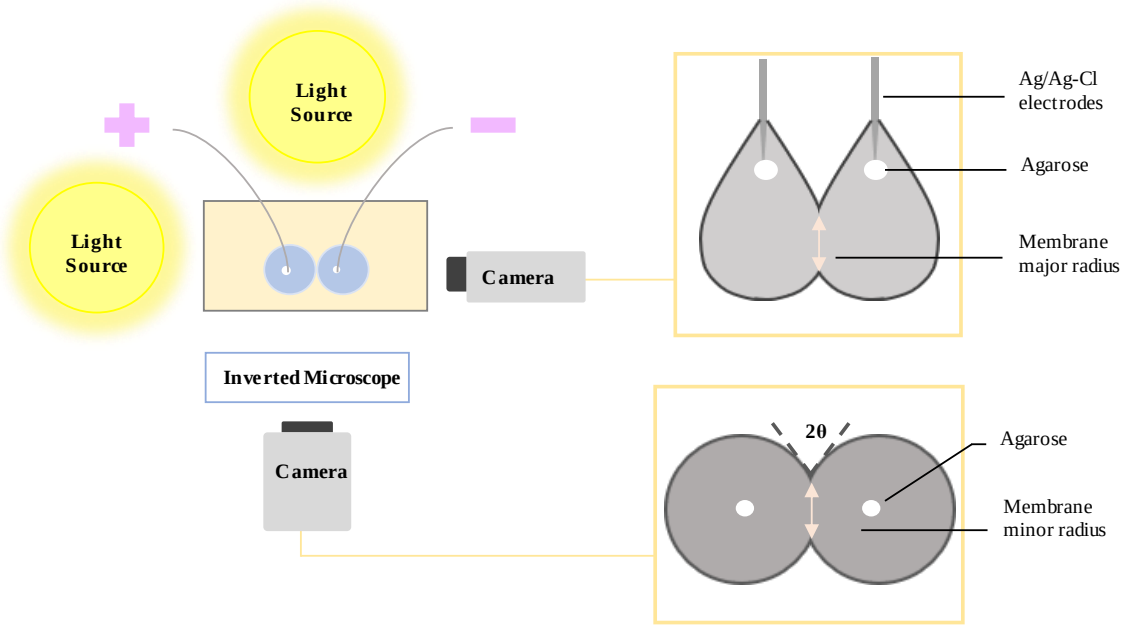


Figure 3.5: Experimental setup used for the creation and characterization of DIBs. The droplets are submerged in an acrylic glass dish with hexadecane and connected to electrophysiology equipment. An inverted microscope (x5.0 magnification) and a zoom

lens camera are used to provide droplet profiles from both sides, enabling simultaneous measurements of the bilayer area and contact angle.

Figure 3.5 describes the setup used for the experiments, intended for the formation, visualization and accurate characterization of DIBs with simultaneous measurements of membrane area ($A_m$) and contact angle ($\theta$). Aqueous droplets are transferred from a micropipette attached to a manual microinjector (Sutter) and manipulator (Siskiyou) onto two silver/silver-chloride (Ag/AgCl) electrodes, which are emerged in an acrylic glass cube (1 cm x 1 cm base, 1 mm thick walls) filled with hexadecane. The tips of the Ag/AgCl electrodes are coated with agarose gel (low EEO, Sigma-Aldrich Co.) to aid in droplet adhesion. The electrodes are connected back to an Axopatch 200B patch clamp amplifier and a Digidata 1440 data acquisition system (Molecular Devices). A prescribed voltage is maintained between the electrodes, and the current necessary to maintain this voltage is recorded. Voltage-clamp mode (whole cell $\beta = 1$) was used at a 5 kHz sampling frequency with a low pass filter of 1 kHz (using the embedded low-pass Bessel filter -80dB/decade). Prior to each experiment, the pipette offset was compensated for by generating a short circuit in between the electrodes and setting the voltage drop to zero. Residual electrode capacitance was eliminated using the patch clamp amplifier's built-in whole cell capacitance compensation prior to membrane formation.

The lipid membrane may be approximated as a capacitor and a resistor in parallel [44, 45] (Figure 3.5 (c)). Consequently, the recorded current may be split into a capacitive and a resistive current (Equation (3.5)):

$$i = \frac{V}{R_m} + C_m \frac{dV}{dt} \tag{3.5}$$

where $C_m$ and $R_m$ are the membrane's capacitance (F) and resistance (Ω) respectively. $i$ and $V$ are the measured current (A) and prescribed voltage (V). A 40 Hz, 10 mV sinusoidal voltage signal was typically used to avoid complications at higher frequencies due to the resistance of the electrode-electrolyte interface and provide a frequency-independent capacitance [27, 46] while generating sufficient current for precise measurements. At these frequencies the voltage drop falls primarily across the membrane itself and the measured current will be primarily capacitive due to the high resistance of DPhPC membranes [47]. Any residual conductive currents across the membrane may be eliminated by fitting the measured current and prescribed voltage to Equation (3.5) through nonlinear regression, isolating the capacitive current.

The key advantage of this approach is the ability to simultaneously measure the area of the adhered bilayer and contact angle. Gravitational forces and the adhesion of the droplet on the electrode surface distort the droplet, creating an elliptical rather than circular membrane. The droplet shape depends on a variety of factors such as the density of the oil, type of lipids used, diameter of the electrodes, volume of the droplets, and qualities of the hydrogel on the electrode. Consequently, it is difficult to estimate the correction factors necessary to account for the membrane ellipticity. The additional side camera addresses this limitation by capturing the droplet contours. When combined with the inverted microscope, both principal axes of the elliptical membrane area are available. The ratio of the major radius to the minor radius depends on the size of the droplets, electrode properties and oil-water density difference as noted in Appendix A, section A.5.

## Data analysis

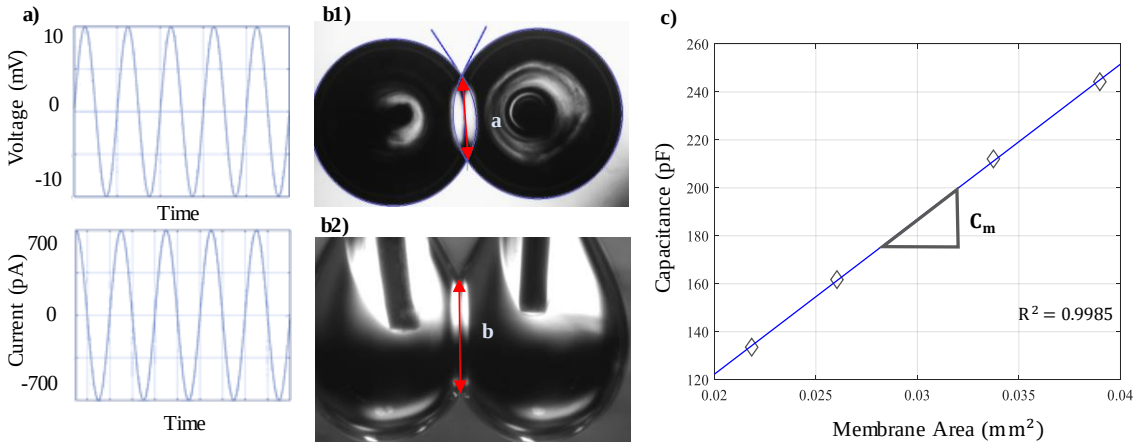


Figure 3.6: The sinusoidal voltage applied across the bilayer (Amplitude: 10 mV; Frequency: 40 Hz) along with the output current (pA) enable the calculation of the total capacitance. b) Both bottom and side views of the DIB are necessary to obtain the area, which is calculated as the area of an ellipse with the major and minor radii as the side and bottom radii, respectively. The contact angle is captured by a customized MATLAB code. c) Membrane's specific capacitance is the slope of capacitance versus area, which was controlled manually by micromanipulators.

The lipid membrane may be approximated as a parallel plate capacitor. Thus, the bilayer's thickness estimated in this study reflects the dielectric thickness or the distance between the two aqueous charged surfaces – in the case of a DIB, the dielectric thickness is the region occupied by lipid acyl chains and any residual oil solvent. The membrane capacitance is given by:

$$\begin{aligned} C_m &= C_s A_m \\ A_m &= \pi ab \\ C_s &= \frac{\varepsilon_0 \varepsilon_r}{h} \end{aligned} \tag{3.6}$$

where $C_s$ is the membrane specific capacitance or capacitance per area, $\varepsilon_0$ is the vacuum permittivity (F/m) and $\varepsilon_r$ is the relative permittivity of the hydrocarbon chains, assumed to be equal to 2.2 [24]. The total capacitance $C_m$ reflects the specific capacitance $C_s$ multiplied by the membrane area $A_m$. The total capacitance is obtained by sending a sinusoidal voltage

(Amplitude: 10mV; Frequency: 40Hz) across the membrane and recording the current output as shown in Figure 3.6 (a). These two recordings are then imported into MATLAB code that separates the capacitive and conductive currents using curve fitting and Equation (3.5). Due to the gravitational influences on the droplet shape, both bottom view and side view images are needed to measure the membrane area as shown in Figure 3.6 (b). Images from the inverted microscope were imported into MATLAB and the imfindcircles() command was used to locate the centre of each droplet as well as their radii. The distance between the centre of the droplets and their dimensions are used to identify the two overlapping points defining the membrane minor axis and the calculated outlines are exported to the original image to check for consistency. If the droplets are not perfectly circular, then some interference due to electrode positioning is assumed and the experiment is repeated. The contact angle between droplets is then calculated from the measured dimensions as shown in Figure 3.6 (b1). The intersection of the two circles denoted the point of tangency for defining the contact angle. The contact angle was then used for visually estimating the bilayer tension as a function of the monolayer tension measured through pendant drop tensiometry using Equation (3.1).

Images from the second camera were also imported into MATLAB and the locations of the two intersections are identified at the highest and lowest point of the membrane as shown in Figure 3.6 (b2), and the distance between them was calculated. This measurement was combined with the measurement for membrane dimensions from the previous step. The membrane's surface area was calculated as the area of an ellipse $A_m = \pi ab$, where the minor ($a$) and major ($b$) radii are the bottom and side radii, respectively.

Membrane capacitance $C_m$ and area $A_m$ are needed to calculate the specific capacitance $C_s$ of the membrane ($\mu F/cm^2$). For the specific capacitance measurements, the droplets were gradually pulled apart using micromanipulators to vary the membrane area and produce the relation between membrane capacitance and membrane. The measured capacitance at each step was plotted versus the corresponding area and the data points were fitted using a first order linear regression setting the intercept to zero where the resulting slope denotes the membrane's specific capacitance [24] (Figure 3.6). The membrane's dielectric thickness (in Angstroms) was calculated next using Equation (3.6). The dimensions of the inverted view were obtained manually for these measurements rather than in MATLAB, since the separation of the droplets led to non-circular projections. Ellipticity values may be found in Appendix A, section A.5.

## Results and discussion

Table 3.1. Results showing the influence of cholesterol on the monolayer surface as well as on the droplet interface bilayer. Measurements obtained at room temperature.

| **Cholesterol Mole Fraction** | **0** | **0.1** | **0.2** | **0.3** |
|---|---|---|---|---|
| $C_s$ ($\mu F/cm^2$) | 0.62 (± 0.01) N = 5 | 0.63 (± 0.01) N = 6 | 0.63 (± 0.02) N = 5 | 0. 63 (± 0.01) N = 5 |
| h (Å) | 31.5 (± 0.3) | 30.8 (± 0.4) | 30.9 (± 0.7) | 31.1 (± 0.5) |
| $\gamma_m$ (mN/m) | 1.14 (± 0.04) N = 10 | 1.17 (± 0.07) N = 5 | 1.30 (± 0.04) N = 7 | 1.43 (± 0.05) N = 11 |
| 2θ (degrees) | 48.8 (± 4.8) N = 12 | 49.0 (± 3.2) N = 17 | 52.4 (± 2.0) N = 12 | 47.4 (± 2.1) N=11 |
| $\gamma_b$ (mN/m) | 2.07 (± 0.12) | 2.13 (± 0.16) | 2.33 (± 0.10) | 2.61 (± 0.14) |
| ε (mN/m) | 0.20 (± 0.15) | 0.21 (± 0.21) | 0.27 (± 0.13) | 0.24 (± 0.18) |

Table 3.1 reports the averages and standard deviations of all variables for lipid monolayers and bilayers assembled with varying cholesterol concentrations. The values

for the specific capacitance ($C_s$), monolayer tension ($\gamma_m$), and contact angle ($\theta$) were directly measured and the standard deviations and sample sizes are reported in the table. Dielectric thickness ($h$), bilayer tension ($\gamma_b$) and adhesion energy ($\Delta F$) were then calculated from these average values, and uncertainty is determined using error propagation equations. The methodology is then validated by comparing the measured values against values in the literature. Measurements for the specific capacitance and thickness of DPhPC without cholesterol in hexadecane match those of the membrane area using the DHB technique [23], and the monolayer and bilayer tensions of DPhPC without cholesterol in hexadecane are within the standard deviation of previously reported values in the literature [22, 24].

**Influence of cholesterol on the bilayer and monolayer tensions**

The monolayer tension of the water-hexadecane interface increases in the presence of cholesterol as measured using pendant drop tensiometry (Table 3.1). Monolayer surface tension ranges from 1.14 mN/m (±0.04 mN/m) with no cholesterol included to 1.43 mN/m (±0.05 mN/m) for 30% cholesterol mole fraction (detailed results in Appendix A section A.2). Cholesterol disrupts the monolayer structure due to its higher negative curvature relative to DPhPC, increasing the surface tension. This increase generates a similar increase in the bilayer's tension as measured by the DIB contact angle and monolayer tension from Equation (3.1). Cholesterol-free lipid bilayers exhibit a surface tension of 2.07 mN/m (±0.12 mN/m) whereas the addition of 30% cholesterol increases the tension to 2.61 mN/m (±0.14 mN/m), reflecting the unfavourable lipid-lipid interactions between cholesterol and DPhPC. The contact angle does not show significant variation with respect to cholesterol

concentrations, and little can be said about the changes in the energy of adhesion as the calculated errors of interval are considerable.

**Influence of cholesterol on the bilayer's dielectric thickness**

Table 3.1 also presents the specific capacitance, and subsequently thickness, of DIBs for the different lipid concentrations. Cholesterol-free DIBs show a specific capacitance of 0.62 μF/cm$^2$ (±0.01 μF/cm$^2$). The addition of 10, 20 or 30% cholesterol increases the specific capacitance to an average value of 0.63 μF/cm$^2$ (±0.012 μF/cm$^2$). Subsequently, the membrane's thickness shows a slight change from 31.5 Å (±0.3 Å) with no cholesterol incorporation to 30.9 Å (±0.6 Å) as an average for all cholesterol concentrations (detailed experimental results can be found in Appendix A, section A.4). Cholesterol may slightly reduce the membrane's dielectric thickness, but a conclusion cannot be definitively stated as the change is minor, and the interval errors overlap.

**DIB response to applied voltage**

The membrane behaves as an elastic capacitor, thinning in response to electrostatic stresses [48, 49]. The applied voltage generates a compressive stress across the membrane as a function of the applied voltage *V*:

$$\sigma_{elec} = \frac{\varepsilon_0 \varepsilon_r}{2h^2} V^2 \qquad (3.7).$$

This also produces a reduction in the apparent bilayer tension through electrical energy [5, 50]:

$$\Delta\gamma_{b,V} = -\frac{\varepsilon_0 \varepsilon_r}{2h} V^2 \qquad (3.8).$$

This reduction in apparent surface tension of the adhered interface produces electrowetting [51], where the incorporation of additional membrane area becomes more energetically favourable [23, 24, 52]. As a result, the membrane simultaneously thins and

expands radially when a voltage is applied across the membrane. It is important to note that the majority of the expansion is primarily due to the incorporation of additional lipids within the membrane rather than lipid lateral distortion, as the membrane dimensions increase substantially. The changes in the bilayer's specific capacitance $C_s$ and total capacitance $C_m$ are quadratic with respect to the applied voltage. The symmetry of the bilayer centres the parabola at $V = 0$ mV, meaning that the membrane's lowest specific capacitance – i.e., highest thickness – is obtained at 0 mV. Thus, the changes can be fit into a parabolic equation of the form [23, 24, 53, 54]:

$$\begin{aligned} C_{s,V} &= C_{s,0}(1 + \beta V^2) \\ C_{m,V} &= C_{m,0}(1 + aV^2) \end{aligned} \tag{3.9}$$

where $\beta$ is the electro-thinning coefficient. These behaviours may be seen in Figure 3.7.

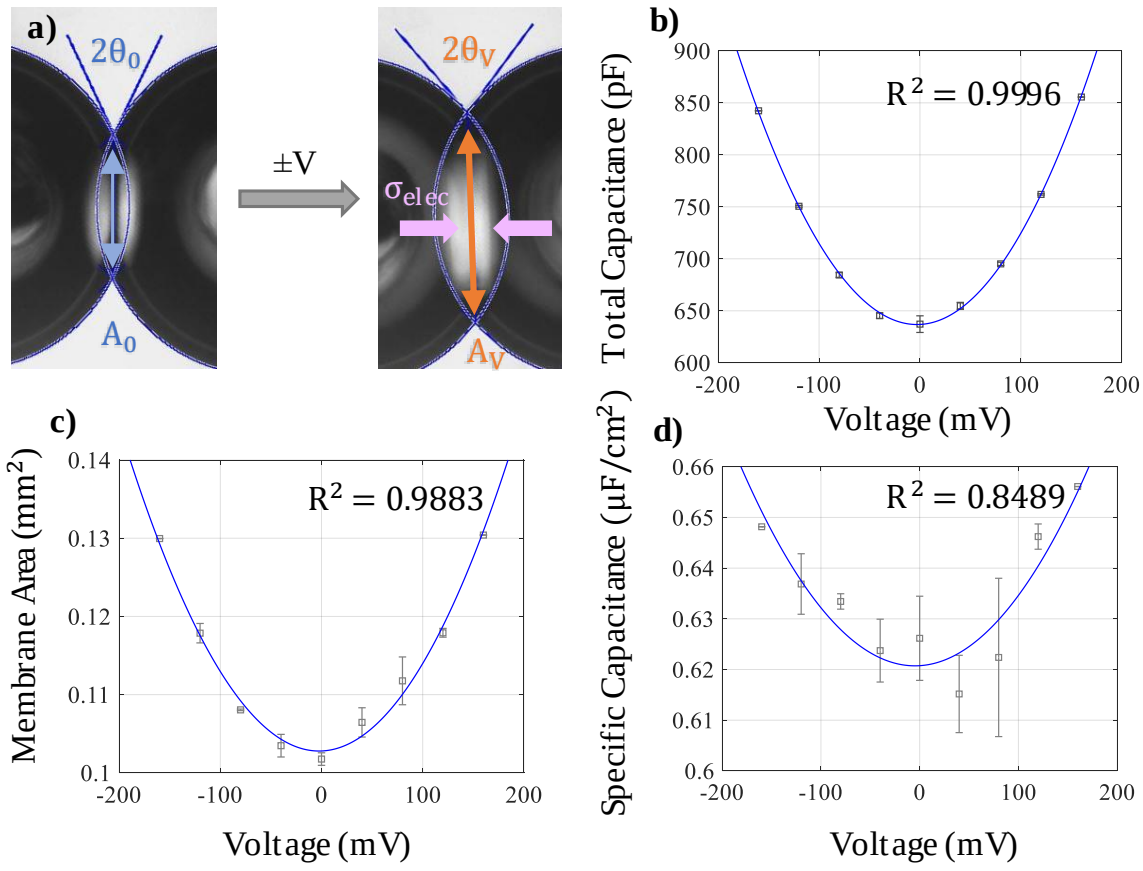


Figure 3.7: a) The application of a DC voltage increases bilayer area and contact angle while dielectric forces lead to bilayer thinning, i.e. increase in specific capacitance. The increase in b) total capacitance, c) membrane area and c) specific capacitance is quadratic with the voltage. Figures and data generated from a DPhPC DIB in hexadecane.

Measuring the changes in the membrane thickness under electrocompression provides information on the disjoining pressure and membrane mechanics (Figure 3.2). It has been observed that the thickness properties and behaviour depend considerably on the oil medium [23, 24, 42, 55]. As an example, Figure 3.8 shows the changes in specific capacitance of 3 separate DIBs – submerged in 3 different oils – with respect to an increasing DC voltage.

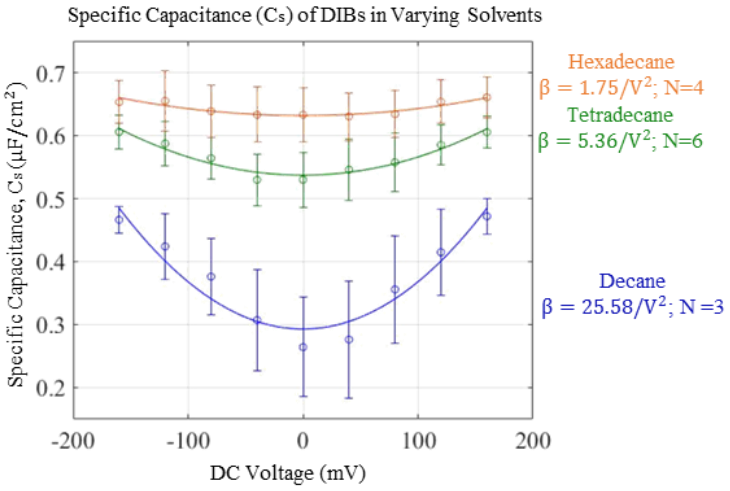


Figure 3.8: Changes in the membrane's specific capacitance (μF/cm$^2$) with respect to the applied voltage (V) for different oils. $\beta$ is the electro-thinning coefficient as the data for each experiment were fit into a parabolic curve (Equation (3.9)).

Figure 3.8 shows that decane oil – $C_{10}H_{22}$ – displays the smallest initial specific capacitance (0.26 μF/cm$^2$) and the highest $\beta$ value (25.58/V$^2$). This change in thickness is a function of the expulsion of residual oil within the membrane rather than lipid compression. As the carbon chain of the oil used increases in length, the amount of residual oil is reduced. In fact, hexadecane oil – $C_{16}H_{34}$ – demonstrates the highest initial specific capacitance (0.63 μF/cm$^2$) and the smallest electro-thinning coefficient of 1.75/V$^2$. Tetradecane – $C_{14}H_{30}$ – values fall in between those of decane and hexadecane, further confirming this dependency. This trend is dependent on the length of the alkane chain [23, 42, 55]. Hexadecane possesses a similar chain length as the selected lipid (DPhPC) in this study, and it is not expected to remain within the membrane. This hypothesis was recently tested by Tarun *et al* [42], examining the properties of lipid bilayer membranes with hexadecane, heptadecane, and squalene. They note that while heptadecane produces the thinnest membranes, hexadecane is an acceptable alternative as long as sufficient time is provided for membrane equilibration. Heptadecane requires elevated temperatures as its

melting point is just above room temperature ($T_m$ = 23 $^o$C). Consequently, hexadecane is selected for all remaining studies on membrane compression to produce "solvent-free" membranes and minimize the influence of the solvent. Sufficient equilibration time is provided for each experiment to ensure minimal solvent influence.

**Influence of cholesterol on membrane properties**

Next, the effect of cholesterol on the structure and mechanics of a solvent-free DPhPC bilayer is investigated using electrical fields producing electrowetting and electrocompression. Electrowetting is the apparent reduction in surface tension upon the application of an electric field causing an expansion of the membrane interface [51] as shown in Figure 3.9 (c) panel 2, and Equation (3.8). Electrocompression occurs as well, where the bilayer thickness is compressed by electrostatic forces (Equation (3.7)) as shown in Figure 3.9 (c) panel 3. These two phenomena – formation of new membrane area and reduction in the membrane thickness – combine to significantly increase the total capacitance as shown in Figure 3.9 (c) panel 1 and described in Equation (3.6).

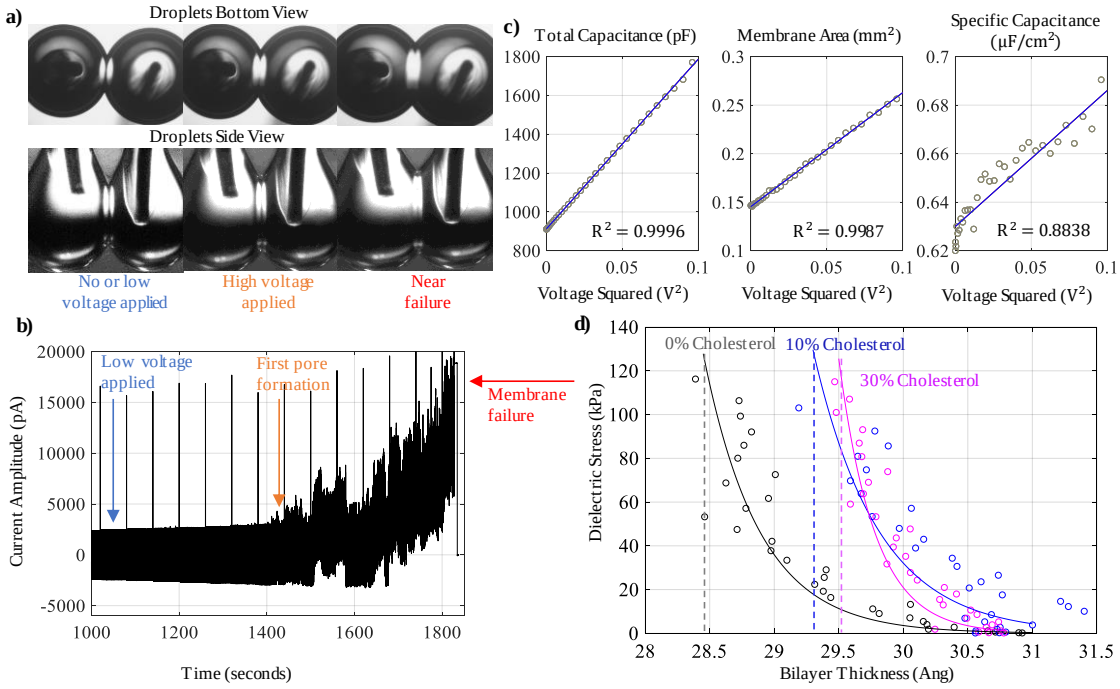


Figure 3.9: a) The bilayer area expands as the DC voltage increases up until failure. b) Pore formation is detected by the current offset from zero. This offset increases until complete failure (droplet coalescence). c) Total capacitance, membrane area, and the specific capacitance exhibit a linear increase with respect to the transmembrane voltage squared. d) The dielectric stress versus bilayer thickness represents the steric repulsion reaction to membrane's thinning. Plotting the calculated stress as a function of membrane thickness allows for estimation of the disjoining pressure curves. The data shown here is averaged from four separate experiments for each membrane composition. 20% cholesterol is not included due to excessive ionic leak observed for this particular membrane composition.

DC voltage increments of 10 mV are applied until membrane failure (≈ 330 mV) as shown in Figure 3.9 (b), holding the voltage for 60 seconds at each increment. The membrane's specific capacitance (Equation (3.6)) is obtained from the recorded membrane capacitance and area at each voltage, enabling the calculation of the dielectric stress applied on the leaflets $\sigma_{elec}$ (Equation (3.7)) and the corresponding bilayer dielectric thickness $h$, Figure 3.9 (a) and (b). As the voltage increases, pores form as measured by increasing in

the membrane conductance, beginning around 200 mV ( Figure 3.9 (b)). This is repeated for each cholesterol-lipid mixture.

Plots of the dielectric stress (kPa) versus membrane thickness (Angstroms) are shown in Figure 3.9 (d). The critical stress at failure does not significantly vary between cholesterol-free and cholesterol-embedded bilayers. The average maximum stress in the three cases is found to be roughly equivalent at ~100 ± 15 kPa. However it should be noted that the maximum voltage reached prior to membrane rupture does increase with cholesterol due to the changes in membrane thickness (Equation (3.7), Figure 3.9 (d)), agreeing with previous research on the influence of cholesterol on electroporation [56, 57]. For 0% cholesterol, a reduction in the membrane dielectric thickness of almost 2 angstroms is achieved before failure, while this compression reduces to 0.6 angstroms with the incorporation of 30% cholesterol. 20% cholesterol produces membranes with significant ion leakage or conductivity which compromises the recordings at higher voltages. As discussed in the introduction, cholesterol's primary influence on lipid bilayers is through condensing and ordering the membrane, even as the overall tension is increased. Cholesterol restricts the movement of phospholipids, leading to a more rigid, well-packed, bilayer structure. Thus, cholesterol-embedded bilayers show a significant increase in rigidity.

**Influence of cholesterol on membrane tension during electrocompression**

The application of an electrical field across the DIB compresses the leaflets [23, 24, 54]. This reduction in thickness leads to subsequent increases in the disjoining pressure (Figure 3.2), which is directly linked to the bilayer tension (Equation (3.4)). Therefore, the change in bilayer tension when a voltage is applied may be described as:

$$\gamma_{b,0} - \gamma_{b,V} = \left[\int_{\infty}^{h} \Pi(h)\,dh\right]_{V} - \left[\int_{\infty}^{h} \Pi(h)\,dh\right]_{0} \tag{3.10}$$

where the subscript *0* is without the voltage and the subscript *V* is with the applied voltage. At equilibrium, the disjoining pressure will match the pressure applied at the membrane surface from within the droplets. This may be approximated as a combination of the pressure from the electric field (Equation (3.7)) and the Laplace pressure [28]:

$$\Pi(h) = \frac{\varepsilon_0 \varepsilon_r}{2h^2} V^2 + \frac{2\gamma_m}{R} \tag{3.11}.$$

The electric field across the monolayer is negligible and the monolayer tension at equilibrium may be considered invariant with respect to the applied voltage. Therefore, the apparent change in bilayer tension may be estimated visually using Young's equation (Equation (3.1)). This apparent change in bilayer tension includes reductions from the electrical energy (Equation (3.8)) and increases from the strain energy (Equation (3.10) combined with Equation (3.11)). From experimental observations, the observed reduction in membrane tension is typically less than the estimated reduction provided by combination of the electric field and strain energy, suggesting that an additional energetic penalty associated with the compression is present. A residual term $E_{residual}$ is proposed to reflect changes in the leaflet lateral structure not captured by the integration of the disjoining pressure or electric field. All of these terms aside from $E_{residual}$ are available from the previously described experimental approach, resulting in Equation (3.12):

$$\underset{\Delta\gamma_{b,app}}{2\gamma_m\left(\cos\theta_0 - \cos\theta_V\right)} = \underset{\Delta\gamma_{b,elec}}{\frac{1}{2}\frac{\varepsilon_r \varepsilon_0}{h_V} V^2} - \underset{\Delta\gamma_{b,mech}}{\int_{h_0}^{h_V}\left(\frac{\varepsilon_0 \varepsilon_r}{2h^2} V^2 + \frac{2\gamma_m}{R}\right)dh} - E_{residual} \tag{3.12},$$

where the visually estimated reduction in membrane tension ($\Delta\gamma_{b,app}$) is on the left hand side and proposed mechanisms responsible for this apparent change are on the right hand side, including the electrical energy ($\Delta\gamma_{b,elec}$) and change in tension from Equations (3.10, 3.11) ($\Delta\gamma_{b,mech}$). If the final two terms on the right-hand side are omitted, this produces the classic Young-Lippmann equation for DIBs [23, 24]. This equation effectively compares the visually reported membrane tension against approximations for each term responsible for the change, with the final term $E_{residual}$ providing a "catch-all" for any unconsidered variables in the model.

Here, the radius of the droplets is assumed to remain constant as the membrane forms new area since these reductions in the Laplace pressure will have minimal influence. The strain energy is integrated numerically from the recorded membrane thickness with the increasing voltage similarly to Figure 3.9 (d).

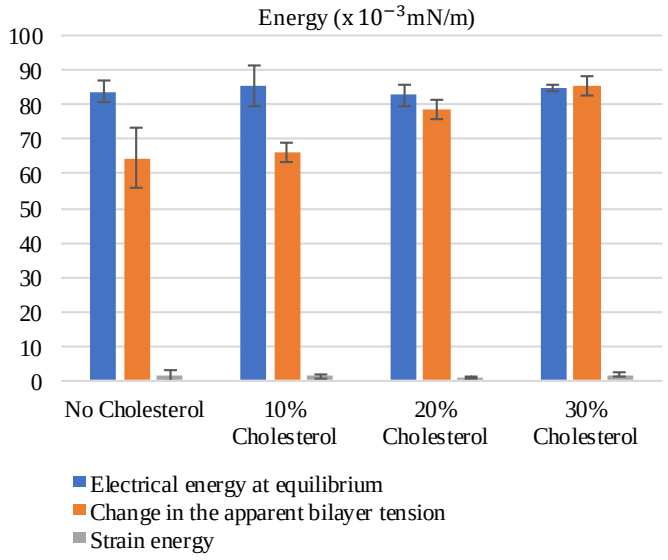


Figure 3.10: Electrical energy applied, change in apparent bilayer tension and strain energy for different cholesterol-DPhPC mole fractions. Each value is the average of 5 experiments. These values are all taken at ±160 mV DC Voltage applied.

A DC voltage ranging from 0 to 160 mV with 40 mV steps held at 60 second intervals is applied. At each voltage, the membrane area, capacitance and contact angle are obtained. These values are combined with the monolayer tensions recorded in Table 3.1 and the residual energy in Equation (3.12) is estimated from these recordings. Values for the first three terms in Equation (3.12) at 160 mV are presented in Figure 3.1 with an increasing cholesterol concentration. Membranes without cholesterol exhibit a notable deviation from the visually indicated change in tension and the measured reduction in membrane tension due to electrical energy, producing an energetic penalty that is not captured by Lippmann-Young equations.

As the cholesterol increases the residual energy becomes negligible. Figure 3.11 shows this residual term for each case plotted as a function of the dielectric stress. Membranes formed with $\leq 10\%$ mole fraction cholesterol exhibit an increase in the residual energy during electrocompression. Membranes formed with $\geq 20\%$ mole fraction cholesterol do not exhibit a similar increase. These changes in the residual energy reflect an increase in the base bilayer tension when placed under mechanical stress. The base membrane tension for cases with cholesterol is already elevated beyond cases without cholesterol as shown in Table 3.1 due to the packing constraints.

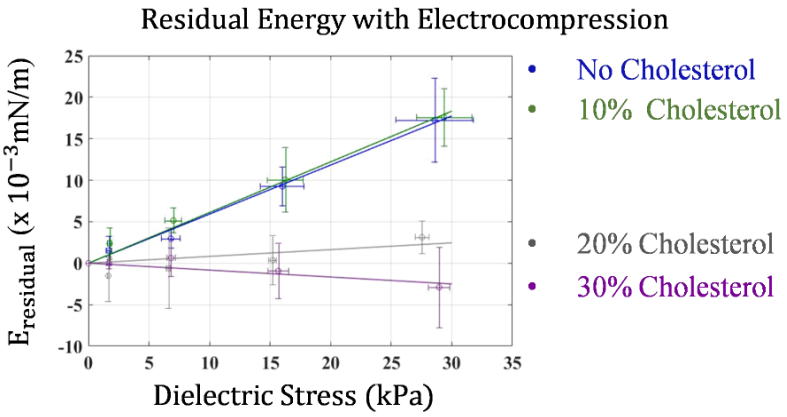


Figure 3.11: The residual energy in Equation (3.10) is plotted for different cholesterol concentrations as a function of the dielectric stress. The cases that exhibit greater change in the thickness – 0% and 10% cholesterol – exhibit an additional energetics term that is not accounted for in the original equation. Cases that exhibit almost no change in thickness – 20% and 30% cholesterol – abide to the original equation without any residual energies. This is hypothesized to be related to a change in lateral area per lipid as the membrane is transversely compressed.

Since the proposed model for membrane compression (Equation (3.12)) does not include lateral changes in the membrane properties, it is hypothesized that the compression leads to distortion in the lipids within the membrane. The presence of cholesterol limits these lateral rearrangements and provides rigidity as shown in Figure 3.9 (d). Complete membrane incompressibility cannot be assumed in DIBs due to the likely presence of residual oil [23, 42, 55], but some coupling of the lateral and transverse deformation is to be expected in "solvent-free" cases such as hexadecane. When the leaflets are compressed transversely, the rigid structure of the cholesterol-DPhPC membrane generated by lipid-lipid interactions resists deformation in both the transverse and lateral directions, leading to a relatively constant area per lipid during electrocompression.

Another hypothesis is cholesterol's reduction of lipid bilayers undulations. In fact, undulations in the lipid bilayer increases the real surface area of the bilayer compared to the projected one, leading to an underestimation of the membrane's specific capacitance.

The group has studied these undulations from a simulation and experimental point of view for DPhPC phospholipids [58]. Cholesterol addition reduces these undulations [59, 60] rendering the real area equals that measured microscopically. Interestingly, membrane specific capacitance did not change dramatically with cholesterol and since in the case of a DIB the bilayer tension is high enough to assume no undulation, the authors do not assign undulations the main cause of the energy unbalance.

These mechanics are detected through a combination of tensiometry and electrophysiology feasible using the DIB approach and demonstrate the capability to measure changes in the interfacial energetics of the membrane under loading.

## Conclusion

A new approach for investigating membrane energetics under electrocompression is proposed. The DIB technique was used as a platform for creating model membranes or lipid bilayers. The unique nature of the DIB approach allows for measuring changes in the interfacial properties by combining droplet and membrane mechanics. Two cameras were implemented to simultaneously track the membrane area ($A_m$) and contact angle ($\theta$), enhancing the precision of the measurements. Membrane properties with and without cholesterol were compared to study the influence of lipid frustration on membrane properties. Pendant drop monolayer tension measurements were used to provide estimations for bilayer tension through Young's equation, and changes in the contact angle were recorded with an increasing voltage across the membrane. Changes in the apparent bilayer tension were compared to a model including contributions from the electrical energy and strain energy with electrocompression. Bilayers without cholesterol exhibited positive residual energy under compression, suggesting the potential for lateral and

rotational rearrangements of lipids as further evidenced by measurements of membrane thickness vs. pressure. Cholesterol enhances the rigidity of the membrane by interdigitating within the lipids and restricts their movement during loading.

## References


1. Lodish, H. and A. Berk, *Molecular cell biology*. Vol. 3.
2. Fridriksson, E.K., et al., *Quantitative analysis of phospholipids in functionally important membrane domains from RBL-2H3 mast cells using tandem high-resolution mass spectrometry.* Biochemistry, 1999. **38**(25): p. 8056-8063.
3. Pike, L.J., et al., *Lipid rafts are enriched in arachidonic acid and plasmenylethanolamine and their composition is independent of caveolin-1 expression: a quantitative electrospray ionization/mass spectrometric analysis.* Biochemistry, 2002. **41**(6): p. 2075-2088.
4. Pike, L.J., *Lipid rafts bringing order to chaos.* Journal of lipid research, 2003. **44**(4): p. 655-667.
5. Heimburg, T., *Thermal biophysics of membranes*. 2008: John Wiley & Sons.
6. Evans, E. and D. Needham, *Physical properties of surfactant bilayer membranes: thermal transitions, elasticity, rigidity, cohesion and colloidal interactions.* Journal of Physical Chemistry, 1987. **91**(16): p. 4219-4228.
7. Needham, D., *Cohesion and permeability of lipid bilayer vesicles*, in *Permeability and Stability of Lipid Bilayers*. 1995, CRC Press, Boca Raton, FL. p. 49-76.
8. Marsh, D., *Lateral pressure profile, spontaneous curvature frustration, and the incorporation and conformation of proteins in membranes.* Biophys J, 2007. **93**(11): p. 3884-99.
9. Cullis, P.R., M.J. Hope, and C.P. Tilcock, *Lipid polymorphism and the roles of lipids in membranes.* Chemistry and physics of lipids, 1986. **40**(2-4): p. 127-144.
10. Sadoc, J. and J. Charvolin, *Frustration in bilayers and topologies of liquid crystals of amphiphilic molecules.* Journal de Physique, 1986. **47**(4): p. 683-691.
11. Nielsen, C. and O.S. Andersen, *Inclusion-induced bilayer deformations: effects of monolayer equilibrium curvature.* Biophysical Journal, 2000. **79**(5): p. 2583-2604.
12. Chorlay, A., et al., *Membrane Asymmetry Imposes Directionality on Lipid Droplet Emergence from the ER.* Developmental Cell, 2019.
13. Kawamoto, S. and W. Shinoda, *Free energy analysis along the stalk mechanism of membrane fusion.* Soft Matter, 2014. **10**(17): p. 3048-54.
14. Kawamoto, S., M.L. Klein, and W. Shinoda, *Coarse-grained molecular dynamics study of membrane fusion: Curvature effects on free energy barriers along the stalk mechanism.* J Chem Phys, 2015. **143**(24): p. 243112.
15. Kollmitzer, B., et al., *Monolayer spontaneous curvature of raft-forming membrane lipids.* Soft matter, 2013. **9**(45): p. 10877-10884.
16. Bayley, H., et al., *Droplet interface bilayers.* Mol Biosyst, 2008. **4**(12): p. 1191-208.
17. Funakoshi, K., H. Suzuki, and S. Takeuchi, *Lipid bilayer formation by contacting monolayers in a microfluidic device for membrane protein analysis.* Anal Chem, 2006. **78**(24): p. 8169-74.
18. Poulin, P. and J. Bibette, *Adhesion of water droplets in organic solvent.* Langmuir, 1998. **14**(22): p. 6341-6343.
19. Hwang, W.L., et al., *Asymmetric droplet interface bilayers.* J Am Chem Soc, 2008. **130**(18): p. 5878-9.

20. Venkatesan, G.A., et al., *Adsorption Kinetics Dictate Monolayer Self-Assembly for Both Lipid-In and Lipid-Out Approaches to Droplet Interface Bilayer Formation.* Langmuir, 2015. **31**(47): p. 12883-93.
21. Chen, Y., C. Helm, and J. Israelachvili, *Molecular mechanisms associated with adhesion and contact angle hysteresis of monolayer surfaces.* The journal of physical chemistry, 1991. **95**(26): p. 10736-10747.
22. Barlow, N.E., et al., *Measuring Bilayer Surface Energy and Curvature in Asymmetric Droplet Interface Bilayers.* arXiv preprint arXiv:1810.09919, 2018.
23. Gross, L.C., et al., *Determining membrane capacitance by dynamic control of droplet interface bilayer area.* Langmuir, 2011. **27**(23): p. 14335-42.
24. isTaylor, G.J., et al., *Direct in situ measurement of specific capacitance, monolayer tension, and bilayer tension in a droplet interface bilayer.* Soft Matter, 2015. **11**(38): p. 7592-605.
25. Schrader, M.E., *Young-dupre revisited.* Langmuir, 1995. **11**(9): p. 3585-3589.
26. Bergeron, V., *Forces and structure in thin liquid soap films.* Journal of Physics: Condensed Matter, 1999. **11**(19): p. R215.
27. Andrews, D., E. Manev, and D. Haydon, *Composition and energy relationships for some thin lipid films, and the chain conformation in monolayers at liquid-liquid interfaces.* Special Discussions of the Faraday Society, 1970. **1**: p. 46-56.
28. Anklam, M., D. Saville, and R. Prud'Homme, *Disjoining Pressure and Film Tension in Comb− Graft Copolymer-Stabilized Oil Films.* Langmuir, 1999. **15**(21): p. 7299-7307.
29. De Feijter, J.A. and A. Vrij, *I. Transition regions, line tensions and contact angles in soap films.* Journal of Electroanalytical Chemistry and Interfacial Electrochemistry, 1972. **37**(1): p. 9-22.
30. De Feijter, J., J. Rijnbout, and A. Vrij, *Contact angles in thin liquid films. I. Thermodynamic description.* Journal of Colloid and Interface Science, 1978. **64**(2): p. 258-268.
31. Leal-Calderon, F., V. Schmitt, and J. Bibette, *Emulsion science: basic principles*. 2007: Springer Science & Business Media.
32. Haydon, D. and V.B. Myers, *Surface charge, surface dipoles and membrane conductance.* Biochimica et Biophysica Acta (BBA)-Biomembranes, 1973. **307**(3): p. 429-443.
33. Liu, Z., et al., *Droplet-based electro-coalescence for probing threshold disjoining pressure.* Lab Chip, 2015. **15**(9): p. 2018-24.
34. Bergeron, V., *Forces and structure in thin liquid soap films.* Journal of Physics-Condensed Matter, 1999. **11**(19): p. R215-R238.
35. Berry, J.D., et al., *Measurement of surface and interfacial tension using pendant drop tensiometry.* J Colloid Interface Sci, 2015. **454**: p. 226-37.
36. Milianta, P.J., et al., *Water Permeability across Symmetric and Asymmetric Droplet Interface Bilayers: Interaction of Cholesterol Sulfate with DPhPC.* Langmuir, 2015. **31**(44): p. 12187-96.
37. Baba, T., et al., *Formation and characterization of planar lipid bilayer membranes from synthetic phytanyl-chained glycolipids.* Biochimica et Biophysica Acta (BBA)-Biomembranes, 1999. **1421**(1): p. 91-102.

38. Husslein, T., et al., *Constant pressure and temperature molecular-dynamics simulation of the hydrated diphytanolphosphatidylcholine lipid bilayer.* The Journal of chemical physics, 1998. **109**(7): p. 2826-2832.
39. Huang, J., J.T. Buboltz, and G.W. Feigenson, *Maximum solubility of cholesterol in phosphatidylcholine and phosphatidylethanolamine bilayers.* Biochimica et Biophysica Acta (BBA)-Biomembranes, 1999. **1417**(1): p. 89-100.
40. Hung, W.-C., et al., *The condensing effect of cholesterol in lipid bilayers.* Biophysical journal, 2007. **92**(11): p. 3960-3967.
41. Parker, A., et al., *Lateral distribution of cholesterol in dioleoylphosphatidylcholine lipid bilayers: cholesterol-phospholipid interactions at high cholesterol limit.* Biophysical journal, 2004. **86**(3): p. 1532-1544.
42. Tarun, O.B., M.Y. Eremchev, and S. Roke, *Interaction of Oil and Lipids in Freestanding Lipid Bilayer Membranes Studied with Label-Free High-Throughput Wide-Field Second-Harmonic Microscopy.* Langmuir, 2018. **34**(38): p. 11305-11310.
43. Lin, S.-Y., et al., *An examination on the accuracy of interfacial tension measurement from pendant drop profiles.* Langmuir, 1995. **11**(10): p. 4159-4166.
44. Schoch, P., D.F. Sargent, and R. Schwyzer, *Capacitance and conductance as tools for the measurement of asymmetric surface potentials and energy barriers of lipid bilayer membranes.* The Journal of Membrane Biology, 1979. **46**(1): p. 71-89.
45. Hodgkin, A.L., A. Huxley, and B. Katz, *Measurement of current-voltage relations in the membrane of the giant axon of Loligo.* The Journal of Physiology, 1952. **116**(4): p. 424-448.
46. Creasy, M.A., et al., *Deterministic model of biomolecular networks with stimuli-responsive properties.* Journal of Intelligent Material Systems and Structures, 2014: p. 1045389X14536004.
47. Sarles, S.A. and D.J. Leo, *Tailored Current—Voltage Relationships of Droplet-Interface Bilayers Using Biomolecules and External Feedback Control.* Journal of Intelligent Material Systems and Structures, 2009. **20**(10): p. 1233-1247.
48. Mosgaard, L.D., K.A. Zecchi, and T. Heimburg, *Mechano-capacitive properties of polarized membranes.* Soft Matter, 2015. **11**(40): p. 7899-910.
49. Sokolov, V. and V. Mirsky, *Electrostatic potentials of bilayer lipid membranes: basic principles and analytical applications*, in *Ultrathin Electrochemical Chemo- and Biosensors*. 2004, Springer. p. 255-291.
50. Berthier, J., *Micro-drops and digital microfluidics*. 2012: William Andrew.
51. Mugele, F. and J.-C. Baret, *Electrowetting: from basics to applications.* Journal of Physics: Condensed Matter, 2005. **17**(28): p. R705-R774.
52. Punnamaraju, S. and A.J. Steckl, *Voltage control of droplet interface bilayer lipid membrane dimensions.* Langmuir, 2011. **27**(2): p. 618-26.
53. Alvarez, O. and R. Latorre, *Voltage-dependent capacitance in lipid bilayers made from monolayers.* Biophysical journal, 1978. **21**(1): p. 1-17.
54. Toyama, S., A. Nakamura, and F. Toda, *Measurement of voltage dependence of capacitance of planar bilayer lipid membrane with a patch clamp amplifier.* Biophysical journal, 1991. **59**(4): p. 939-944.

55. Beltramo, P.J., L. Scheidegger, and J. Vermant, *Towards realistic large area cell membrane mimics: Excluding oil, controlling composition and including ion channels.* Langmuir, 2018.
56. Kotnik, T., et al., *Membrane electroporation and electropermeabilization: mechanisms and models.* Annual review of biophysics, 2019. **48**.
57. Koronkiewicz, S. and S. Kalinowski, *Influence of cholesterol on electroporation of bilayer lipid membranes: chronopotentiometric studies.* Biochimica et Biophysica Acta (BBA)-Biomembranes, 2004. **1661**(2): p. 196-203.
58. Chaurasia, A.K., et al., *Evaluation of bending modulus of lipid bilayers using undulation and orientation analysis.* Physical Review E, 2018. **97**(3): p. 032421.
59. Marsh, D., *Renormalization of the tension and area expansion modulus in fluid membranes.* Biophysical journal, 1997. **73**(2): p. 865-869.
60. Evans, E. and W. Rawicz, *Entropy-driven tension and bending elasticity in condensed-fluid membranes.* Physical review letters, 1990. **64**(17): p. 2094.

# CHAPTER 4

# STUDYING THE MECHANICS OF MEMBRANE PERMEABILIZATION THROUGH MECHANOELECTRICITY [3]

[3] El-Beyrouthy, J., Makhoul-Mansour, M. M., & Freeman, E. C. (2022). Studying the Mechanics of Membrane Permeabilization through Mechanoelectricity. *ACS Applied Materials & Interfaces*.
Reprinted with the permission of publisher.

**Abstract**

In this research real-time monitoring of lipid membrane disruption is made possible by exploiting the dynamic properties of model lipid bilayers formed at oil-water interfaces. This involves tracking a voltage signal generated through rhythmic membrane perturbation translated into adsorption and penetration of charged species within the membrane. Importantly, this allows for the detection of membrane surface interactions that occur prior to pore formation that may be otherwise undetected.

The requisite dynamic membranes for this approach are made possible through the droplet interface bilayer (DIB) technique. Membranes are formed at the interface of lipid monolayer-coated aqueous droplets, submerged in oil. We present how cyclically alternating the membrane area leads to the generation of mechanoelectric current. This current is negligible until a composition mismatch between the membrane monolayers is produced, such as a one-sided accumulation of disruptive agents. The generated mechanoelectric current is then eliminated when an applied electric field compensates for this asymmetry, enabling measurement of the transmembrane potential offset. Tracking the minimizing voltage with respect to time then reveals gradual accumulation of disruptive agents prior to permeabilization. The innovation of this work is emphasized in its ability to continuously track membrane surface activity, highlighting the initial interaction steps of membrane disruption.

In this chapter we begin by validating our proposed approach against measurements taken for fixed composition membranes using standard electrophysiological techniques. Next, we investigate surfactant adsorption, including hexadecyltrimethylammonium

bromide (CTAB, cationic) and sodium decyl sulfate (SDS, anionic), demonstrating the ability to track adsorption prior to disruption. Finally, we investigate the penetration of lipid membranes by melittin, confirming that the peptide insertion and disruption mechanics are in-part modulated by membrane composition.

## Introduction

The characterization of interactions between dispersed species in aqueous environments and the boundaries surrounding cellular organisms is key for understanding agent-aided membrane permeabilization and transport, including the functionalities of peptides [1], synthetically formulated nanoparticles such as biodegradable nanocarriers [2], antimicrobial polymers [1], and detergents [3, 4]. These cellular boundaries are semi-permeable membranes enclosing the intracellular components and isolating the cytosol from the extracellular environment, crucial for healthy cellular functionality [5]. The membrane provides a protective barrier regulating transport of dissolved species into and out of the cell, making it the first point of interaction between a targeting agent and the desired cells [6, 7]. Hence, this work proposes a technique to test these interactions and characterize membrane disruption process to assist in the design of pharmaceuticals [8], nanoparticle design [9] and material engineering [10].

Cellular membranes are fundamentally structured as double layers of phospholipids possessing a hydrophobic interior and two hydrophilic outer layers [11]. The bulk membrane properties are largely dictated by lipid composition and organization within the membrane. For example, the exoplasmic leaflet of gram bacteria presents a negative surface charge from the abundant presence of anionic headgroups, rendering them more susceptible to cationic antibacterial agents [12]. These properties are the driving forces for nonselective membrane surface interactions, such as micelle-forming detergents and some cationic antimicrobial peptides [1, 13]. These nonselective interactions are mediated by a combination of properties of the disruptive agent and the membrane. Electrostatic forces

attract positively charged species to a typically negatively-charged membrane surface where initial attachment occurs, followed by membrane penetration through hydrophobic affinity [1]. These types of interactions are the main focus of this work, where alterations in the membrane electrostatic profile are tracked.

Membrane disruption mechanics are often studied in a tailorable environment through the formation of model lipid membranes [14]. These lipid membranes mimic the fundamental structure of biological membranes and contain a double layer of phospholipids, produced *in vitro* through a variety of methods [15]. Model membranes present a simplified yet tunable architecture, providing a repeatable, and adjustable platform for investigating membrane interactions through various approaches [16-18]. For example, super-resolution microscopy allows for the characterization of lipid domains [19], interferometry has been utilized to observe real-time binding of proteins to liposomes [20] and X-ray and neutron techniques allow for the characterization of functional nanoparticles with planar supported model membranes [21]. Combining two techniques largely enhances their advantages, such as combining AFM (atomic force microscopy) and X-ray reflectivity provides simultaneous structure and electrostatic characterization [22], or using optical trapping with confocal Raman spectra allows for longer data acquisition period [23]. Furthermore, computational simulations provide an indispensable tool to predict the behavior of these interactions on a molecular level [24, 25].

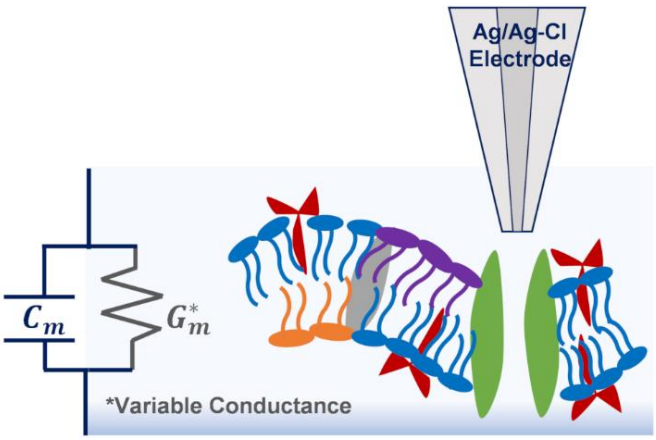


Figure 4. 1: Membrane electrophysiology enables the investigation of membrane active agents, through membrane electrical representation: a capacitor and a resistor in parallel. The introduction of a membrane-solubilizing agent leads to changes in these properties, driven by the formation of pores, or conductive pathways, allowing ionic transport across the double layer. Traditional electrophysiology studies focus on tracking the dynamic changes in membrane conductance to reveal information about the adsorption mechanism and the model of pore formation. Ag/Ag-Cl electrodes allow for controlling the voltage drop across the membrane and for measuring the corresponding generated current.

Herein we propose a new technique for tracking membrane surface interactions prior to permeabilization. This technique is based on membrane electrophysiology for understanding membrane-nanoparticles interactions. Electrophysiology relies on monitoring changes in the bilayer's electrical properties [15, 26-30], where the membrane is approximated as a capacitor and a resistor in parallel [26, 31, 32] as illustrated in Figure 4. 1**.** The membrane capacitance arises due to the difference in hydrophilic-hydrophobic permittivity of the lipid regions [31, 33], whereas its resistance is a result of its well-packed hydrophobic interior. Changes in these properties are used to detect membrane activity [34]. The commonly adopted approach is tracking changes in membrane conductance as the latter varies in response to membrane permeabilization [26, 35]. Sudden changes in the membrane conductance signify the formation of pores within the membrane, and the characteristics and intensity of these events are used to describe the pore-forming

mechanism [26]. However, these measurements typically capture the point at which pores are generated rather than providing insights into interactions prior to failure such as accumulation within the membrane.

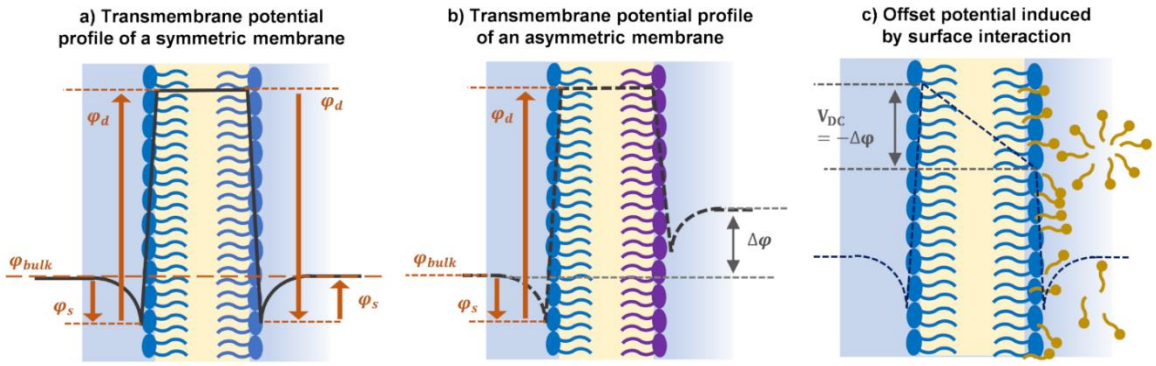


Figure 4. 2: Lipid monolayers possess a surface, $\varphi_s$, and a dipole, $\varphi_d$, potential. The amplitude and distribution of these potentials outline the transmembrane potential profile. a) In the case of monolayers formed from similar lipid mixtures, the membrane is called symmetric, and these potentials are well-balanced across the double layer. b) In the case where monolayers are formed from different lipid compositions, the membrane is called asymmetric, and the potential profile shows an imbalance, denoted as the membrane potential offset, $\Delta\varphi$. c) This offset may also be variable if induced by an unequal and fluctuating adhesion of nanoparticles across the membrane. In all cases, membrane potential offset can be compensated for through the introduction of an external electric field reestablishing the charge distribution and membrane symmetry.

The technique proposed herein expands on the capacitor-resistor model of the membrane, and focuses on localized electric fields within the membrane interior [36]. Phospholipids are amphiphilic molecules possessing a specific charge distribution across their molecular structure, which leads to localized potentials within the lipid leaflets, including surface ($\varphi_s$) and dipole ($\varphi_d$) potentials [31]. The surface potential depends on the leaflet surface charge governed by the phospholipids headgroup interactions with the surrounding electrolyte solution [37], whereas the dipole potential arises due to dipolar residues at the linking group of the amphiphilic molecule [38]. The amplitude and

distribution of these localized potentials across the two lipid layers dictate the overall transmembrane potential profile illustrated in Figure 4. 2**.** In the case where the two leaflets have similar lipid compositions, the identical surface and dipole potentials produce a symmetric transmembrane potential profile as illustrated in Figure 4. 2 (a). In the case where the membrane leaflets are formed with different lipid compositions, the dissimilarity between the potentials generates an imbalance across the membrane profile, as presented in Figure 4. 2 (b). When the membrane is short-circuited through electrodes placed in the neighboring solution, this imbalance in potentials combined with a prescribed bulk potential produces an offset in the transmembrane electric field, denoted as membrane potential offset, $\Delta\varphi$ [39]. Previous electrophysiology analyses [31, 40] showed that it is possible to compensate for this offset by applying a matching voltage at the boundaries, as represented by the dashed lines of Figure 4. 2 (c), eliminating the total field across the membrane. This compensating voltage is equivalent to the membrane potential offset, and resolving this value provides measurements for the developing membrane asymmetry.

The membrane potential offset is often measured using the minimum capacitance technique based on electrowetting principles [41, 42]. This method is reliable and accurate and has been successfully applied to many studies of membrane asymmetry [41, 43, 44]. However, the membrane must reach its equilibrium dimensions for each voltage to produce the desired quadratic trend [42]. Consequently the frequency of the measurement is often insufficient to resolve rapid membrane-nanoparticle interactions [3]. An alternative approach is necessary for the analysis of quickly developing changes in the membrane structure. The use of the intramembrane field compensation technique allows for

investigating dynamic membrane mechanics through electrocompression [45-48]. This technique works best with softer model membranes exhibiting a higher degree of thinning under an applied voltage [48, 49].

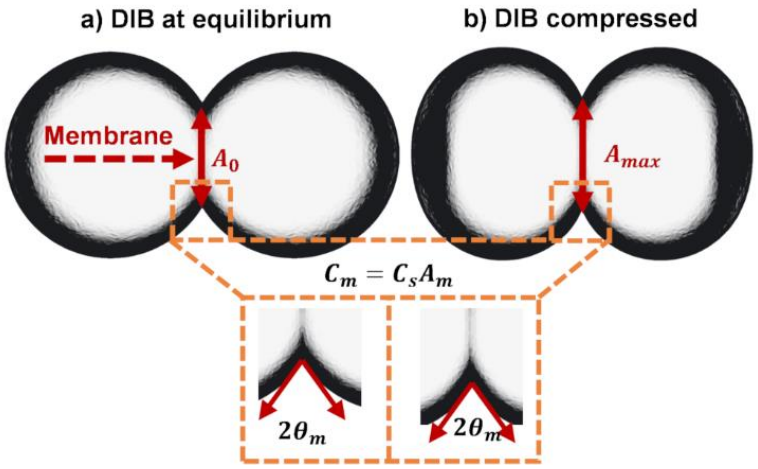


Figure 4. 3: The droplet interface bilayer, or DIB, is a model membrane formed at the interface of two lipid monolayer-coated droplets in an oil medium. a) At equilibrium, the membrane area is at its resting initial value minimizing the system's total energy. b) The DIB setup allows for the displacement of one droplet with respect to the other, causing the membrane area to oscillate. Due to the area-capacitance relationship of lipid membranes, these oscillations lead to the generation of a capacitive-current: mechanoelectricity. Images are produced using the Surface Evolver software with varying constraints [50, 51].

The presented approach is based on the droplet interface bilayer (DIB) as the model membrane [52, 53]. As illustrated in Figure 4. 3 (a), DIBs form lipid membranes at the interface of two lipid-coated aqueous droplets in an oil medium. These emulsion-based systems are advantageous as they allow for the creation of asymmetric membranes [41, 43] as well as tunable membrane areas [42, 49] through compression [54] as depicted in Figure 4. 3 (b). Alternating the membrane area through harmonic compression combined with an electric field across the membrane produces capacitive currents [42, 49]. This capacitive-

induced current is denoted as the mechanoelectric current and assuming negligible membrane leak, the equation describing it is as follows [54]:

$$I(t)_{mech} = (V_{DC} + \Delta\varphi)\frac{dC(t)}{dt} \tag{4.1}$$

where $I(t)_{mech}$ is the mechanoelectric current, $V_{DC}$ is the applied direct voltage, $\Delta\varphi$ is the membrane potential offset and $C(t)$ is the alternating change in membrane capacitance. Notably, $I_{mech} = 0$ when $V_{DC} = -\Delta\varphi$, minimizing the current when the applied direct voltage balances any offset generated by membrane asymmetry.

This work utilizes Equation (4.1) as the fundamental link for characterizing membrane asymmetry through mechanoelectricity. The necessary voltage for eliminating the mechanoelectric current is set to be equal in magnitude and opposite in sign to the potential offset. The Grahame equation is then used to approximate the corresponding surface charge when desired, requiring the assumption of minimal agent translocation across the membrane [55].

We examine the mechanoelectric approach in several steps, first validating the technique against other methods then extending to new capabilities. To begin, results for quasi-fixed voltage offsets produced through membrane asymmetry are compared against results from the minimum capacitance technique. Afterwards, mechanoelectricity is used to characterize micelle-forming CTAB (hexadecyltrimethylammonium bromide, ≥98%, Sigma-Aldrich) and SDS (sodium dodecyl sulfate, ≥ 99.9%, Research Products International) detergents to demonstrate tracking of membrane-detergent interactions.

These agents are selected as they have been thoroughly studied with model membranes providing a basis for evaluating our approach [56, 57]. Following, surface charge dependent interactions of the membrane-permeabilizing peptide, melittin (Honeybee venom, ≥ 85%, HPLC) were investigated. Melittin is a membrane-active cationic antimicrobial peptide, that interacts differently with zwitterionic and anionic membranes [58-61]. We use melittin's dependency on membrane composition to further demonstrate applications of the mechanoelectricity technique by examining surface accumulation prior to pore formation for varying membrane surface charges.

## Experimental approach

This section briefly discusses the experimental apparatus used for generating and minimizing the mechanoelectric current. Additional experimental details and results are provided in appendix B as follows: Section B.1 Lipids and Agents Solution Preparations; Section B.2 Freely Hanging Droplet Interface Bilayers and The Minimum Capacitance Technique; Section B.3 Surface Charge Calculations; Section B.4 Mechanoelectricity Setup and Optimization; Section B.5 Fixed Potential Offset Measurement; Section B.6 Resolving Lipid Flip-Flop in Static Membranes; Section B.7 Membrane-Agent Dynamic Studies; Section B.8 Diffusion in the Droplet Observed Through Calcein; Section B. 9 Full Detergents Results; and Section B.10 Full Melittin Results.

## Mechanoelectric current generation and calculation

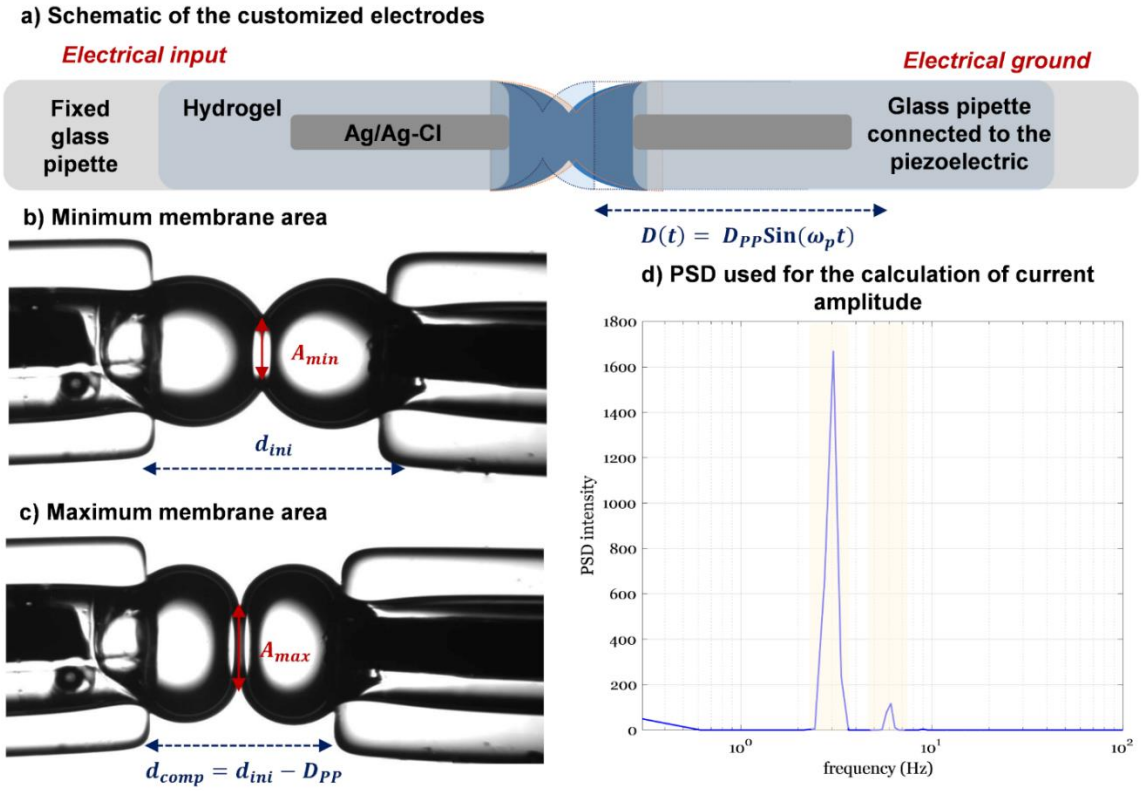


Figure 4. 4: DIB customized experimental setup. a) Lipid-dispersed droplets are placed on the tip of two parallel glass pipettes forming the lipid membrane at their adhered interface. The glass pipettes contain Ag/Ag-Cl electrodes secured in place through hydrogels. The electrical ground pipette is attached to the piezoelectric actuator providing the mechanical displacement. b) and c) show the droplet compression leading to the membrane area expansion. This harmonic displacement is followed by a similar change in membrane area and thus capacitance, leading to the generation of mechanoelectricity. d) Power Spectral Density (PSD) of the generated mechanoelectric current is used to calculate its amplitude. The peak at the displacement frequency $f_p$ (3 Hz) and at the second harmonic $2f_p$ (6 Hz) were both considered in the calculations.

The experimental platform adopted for generating mechanoelectricity is shown in Figure 4. 4 (a). Two glass pipette electrodes are first prepared to hold the lipids-dispersed droplets [10, 54, 62, 63]. Silver/silver-chloride electrodes are then inserted into these cylindrical glass pipettes and fixed in place by filling the surrounding gaps with hydrogels.

After solidifying the hydrogels, pipettes are submerged into a circular oil dish, while ensuring their parallel alignment for even compression. One pipette is connected to the headstage of an Axopatch 200B amplifier and remains immobile. The facing pipette is connected to the electrical ground and to the piezoelectric actuator. A function generator is used to provide the displacement of the piezoelectric actuator according to the following equation: $D(t) = D_{PP}\, sin(2\pi f_p t)$, where $D_{PP}$ is the peak-to-peak amplitude and $f_p$ is the oscillations frequency. This displacement induces a change in membrane area as seen in Figure 4. 4 (b) and (c). The following parameters were adopted for all experiments shown in this work: $D_{PP}$ = 150µm *and* $f_p$ = 3Hz. This displacement amplitude was chosen as the one that generates a substantial current amplitude while avoiding excessive droplets perturbation or coalescence. This frequency value was selected as the optimum between excessive change in membrane tension [63] and accurate measurements of the mechanoelectric current [54]. More on the effect of displacement amplitude and frequency is discussed in appendix B sections B.4.2 and B.4.3. Figure 4. 4 (d) shows the power spectral density of the current signal, with clear peaks observed at the displacement's first and second frequencies.

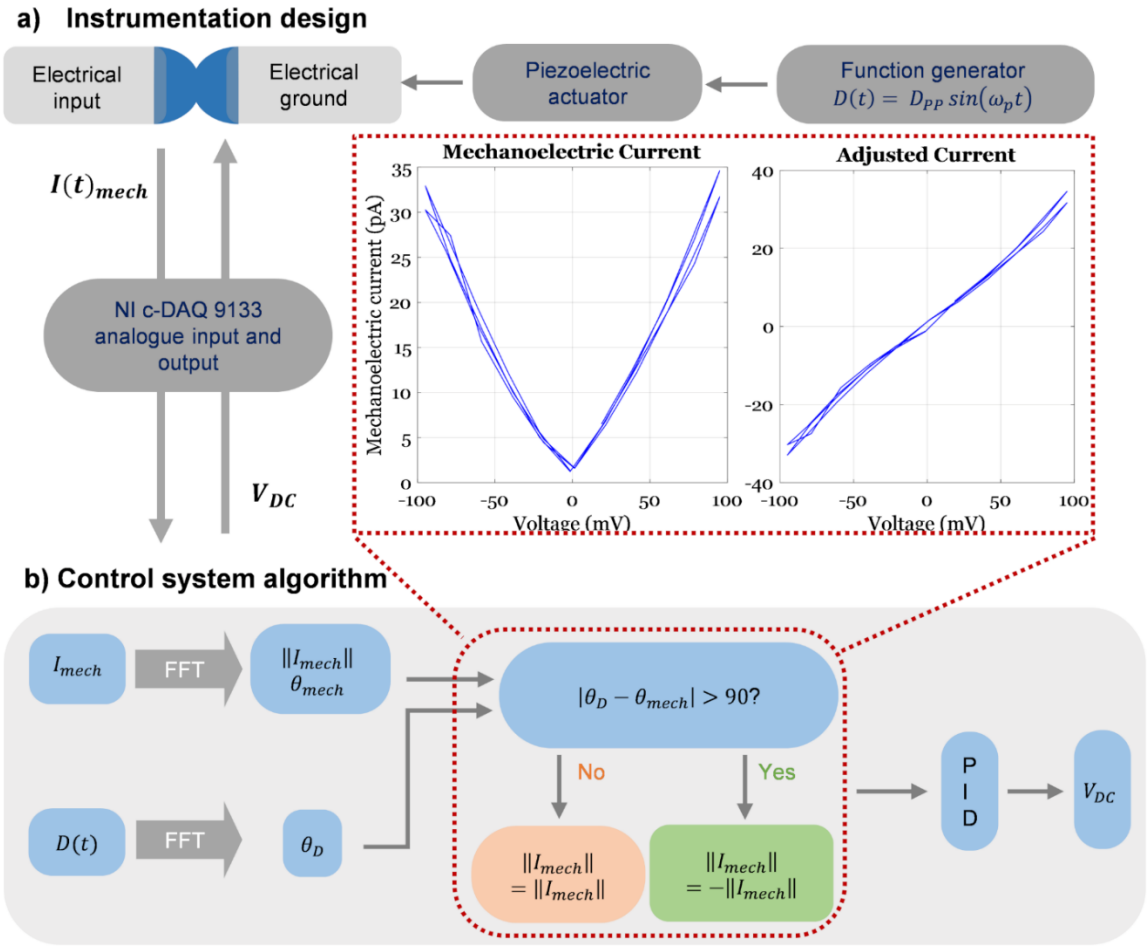


Figure 4.5: Summary of the instrumentation and control design for the real-time measurement of membrane potential offset using mechanoelectricity. a) A function generator supplies the displacement function to the piezoelectric actuator and the membrane transduces the mechanical displacement into an electrical signal. The signal is then sent to the NI-cDAQ analogue reader to extract the value associated with droplet compression. b) A LabVIEW control algorithm is developed for the acquisition and minimization of the mechanoelectric current. Current and displacement amplitudes and phase angles are calculated using an FFT sub-VI. The phase angles are used to linearize the current-voltage relation as shown in the red-dotted plots. Influenced by the tuned PID gains and its output range, the $V_{DC}$ necessary for minimizing the mechanoelectric current is calculated and provided to the membrane electrical input through the NI-cDAQ analogue output.

A summary of the instrumentation and control design developed for membrane surface characterization is shown in Figure 4.5. An Agilent 3322A function/arbitrary

waveform generator is utilized to specify the displacement frequency and amplitude to the piezoelectric (P601-Physik Instrumente) actuator according to the voltage-to-distance calibration. Upon initiating droplet compression, the mechanoelectric current is routed through the NI-cDAQ analogue input to a custom-designed LabVIEW VI summarized in Figure 4.5 (b). The fast Fourier transform (FFT) is generated through a sub-VI that calculates the amplitude and the phase angle of the current and the displacement. Some adjustments were made to ensure a reliable performance of the control system. First, $I_{mech}$ includes both the first and second peak of the FFT to account for signal distortion and a one cell averaging constant false alarm rate (CFAR) algorithm was applied to separate the noise floor from the signal. Second, the relationship between the mechanoelectric amplitude and voltage is not linear but follows $y = \|x\|$. Since the proportional-integrative-derivative (PID) controller is best suited for linear systems, the voltage-current relationship is adjusted based on the measured phase angle difference between the displacement and the current. The controller then calculates the necessary $V_{DC}$ to minimize the mechanoelectric current, which is sent through the NI-cDAQ analogue output, and this voltage is recorded over time.

## Results and discussion

### Initial testing of the control system response

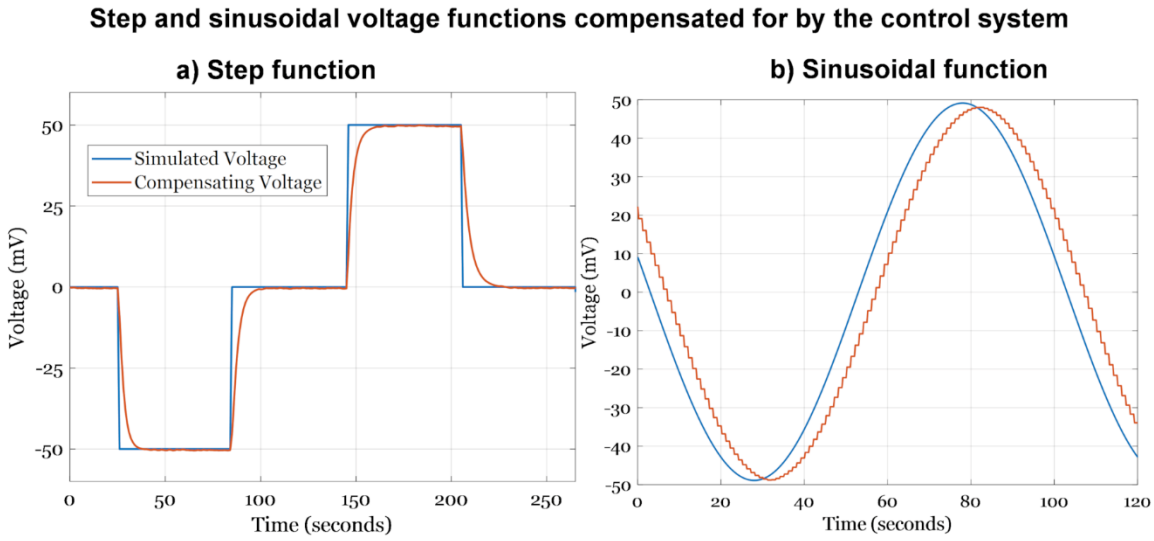


Figure 4. 6: Simulated and compensating voltage showing the controller's response in tracking the membrane potential offset. An initially symmetric membrane, $\Delta\varphi \sim 0$ mV, was formed and a simulated a) step, and b) sinusoidal voltage functions were applied across this symmetric bilayer. Results show that the system is able to follow the applied voltage within few seconds lag and with least steady state error.

Prior to investigating transient membrane surface interactions, it is important to test and validate the reported compensating voltages provided by the mechanoelectricity technique. First, the LabVIEW built-in PID controller was tuned, aiming for a short rise and settling time, while reducing overshoot and oscillations. For this fluidic system and for a hemisphere droplet size of approximately 1 mm in diameter submerged in hexadecane oil with the provided oscillation characteristics, the PID gains were calibrated as follows: $K_d$ = 10, $T_i$ = 0.002 and $T_d$ = 0.001. Note that membrane dimensions and rate of response depend on experimental parameters and might influence the controller's performance. The tuned controller was then tested using an offset voltage provided by a function generator

as shown in Figure 4. 6. Results show that the steady state error is minimal, with an approximately 10-second lag between the tracked compensating voltage and the externally applied voltage. This lag may be reduced if necessary by increasing the compression frequency and reducing the cycles per measurement at the expense of precision and membrane stability.

**Fixed membrane potential offsets results**

a) Phospholipids with different surface and/or dipole potential

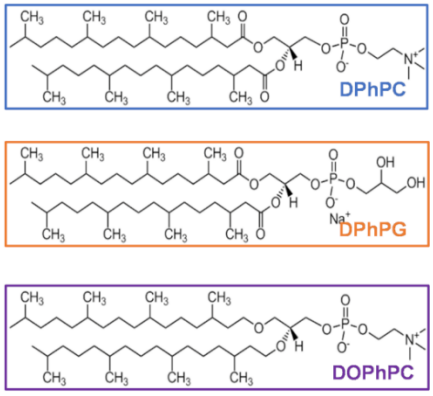


b) Membrane potential as calculated by the minimum capacitance technique and mechanoelectric (N≥5)

| Input Side Leaflet | Ground Side Leaflet | Type of Asymmetry | Potential Offset (mV) | |
|---|---|---|---|---|
| | | | Minimum Capacitance | Mechano-electricity |
| DPhPC | DPhPC | None | - 0.5 (±3.2) | - 0.1 (±0.3) |
| DPhPC | DPhPG:DPhPC 1:4 | Surface Potential Difference | 26.5 (±3.1) | 28.7 (±2.5) |
| DPhPG:DPhPC 1:4 | DPhPC | | -29.7 (±1.8) | - 32.0(±1.4) |
| DPhPC | DOPhPC | Dipole Potential Difference | 125.8 (±2.5) | 132.5 (±11 ) |
| DOPhPC | DPhPC | | -133.0 (±4.3) | - 128.2 (±4.3) |

Figure 4.7: Steady state membrane potential offset as measured by the traditional minimum capacitance technique and mechanoelectricity. a) Three phospholipids are used herein as they present surface and dipole potential dissimilarities with respect to each other. DPhPC is a zwitterionic ester phospholipid, DPhPG is an anionic ester phospholipid and DOPhPC is a zwitterionic ether phospholipid. Molecular structures were obtained from Avanti Polar Lipids (http://www.avantilipids.com). b) Symmetric membranes were formed with DPhPC/DPhPC; asymmetric membranes with surface potential difference were formed as DPhPC/1:4 DPhPG:DPhPC; asymmetric membranes with dipole potential difference were formed as DPhPC/DOPhPC. For asymmetric membranes, the electric field direction was switched by switching the sides of the monolayers with respect to the electrical input. This led to similar magnitude but opposite sign potentials. All experiments were conducted in hexadecane oil and for $N \geq 5$.

After verifying that the compensating voltage is able to follow a provided boundary potential as shown in Figure 4. 6, we next move to measuring fixed offset asymmetric membranes. Three phospholipids were selected for generating asymmetric surface and

dipole potentials as described in Figure 4.7 (a). 1,2-diphytanoyl-sn-glycero-3-phosphocholine (DPhPC) is a zwitterionic ester phospholipid, used as a standard electrically neutral phospholipid. 1,2-diphytanoyl-sn-glycero-3-phospho-(1'-rac-glycerol) (sodium salt) (DPhPG) is an anionic ester phospholipid, when mixed with DPhPC the resulting monolayer presents an established negative surface charge that depends on the mass ratio of these two lipids as well as their area per lipid. The resulting monolayer presents a surface potential asymmetry with the neutral DPhPC monolayer. Lastly, 1,2-di-O-phytanyl-sn-glycero-3-phosphocholine (DOPhPC) is a zwitterionic ether phospholipid, whose monolayer possesses a dipole potential difference in comparison to that of DPhPC.

Three membrane compositions were formed from these lipids as follows: symmetric DPhPC/DPhPC membranes, surface potential asymmetric DPhPC/1:4 DPhPG:DPhPC membranes, and dipole potential asymmetric DPhPC/DOPhPC membranes. First, the potential offsets of these three membranes were calculated using the established minimum capacitance technique [41, 43], then compared to the values measured using mechanoelectricity. Note that the potential offsets of these cases are expected to remain constant, as these membranes exhibit minimal lipids flip-flop [41], even under constant oscillations as confirmed in appendix B section B.6.

For dipole asymmetric DPhPC/DOPhPC membranes, the potential offset obtained lies within the standard deviation of previously published work [41]. As for the surface asymmetric DPhPC/1:4 DPhPG:DPhPC membranes, the potential offset agrees with Grahame equation describing the surface potential [55], considering the ratio of anionic to zwitterionic phospholipids and the hydrating buffer solution described in appendix B

section B.1. Next, mechanoelectricity was utilized to measure the potential offset of these same membranes. Averages and standard deviations are shown in the table of Figure 4.7 (b). It is concluded that the potential offsets measured by mechanoelectricity align with those calculated from the minimum capacitance technique. Additional examples of these mechanoelectricity measurements are found in appendix B section B.5.

**Characterizing membrane-detergents interactions**

The goal of this research is to identify membrane surface activities prior to membrane permeabilization through electrophysiology which were previously undetected in measurements of membrane conductance. The interactions of active agents at the membrane surface include the initial parallel surface attachment driven by electrostatic forces, followed by the transverse penetration driven by hydrophobic affinity [1]. These preliminary interactions are not observed in traditional conductance measurements. In the following two sections, we successfully track the transient processes of membrane permeabilization through the continuous and real-time detection of membrane surface activity initiated by slow-acting detergents and cationic antibacterial peptide.

First, symmetric membranes are formed, and rhythmic compressions are initiated using the piezoelectric actuator. At $t$ = 0 seconds, a microdroplet containing the desired disruptive agent at a known concentration is added into the fixed droplet. The volume of the added microdroplet is used to estimate the in-droplet concentration after equilibrium is reached. The compensating voltage is tracked over time until membrane permeabilization occurs i.e., sudden jumps in membrane conductance. While it is possible to continue the measurements of the offset voltage after the formation of pores, these jumps in the

membrane conductance introduce excessive noise in the measured current which threaten the precision of the compensating voltage, even after appropriate modifications to remove the noise floor. Furthermore, since pore formation is linked to the agents traversing the membrane and interacting with both leaflets, the measured leaflet asymmetry is reduced after permeabilization and may no longer accurately link to the one-sided surface charge. Additional experimental details are found in Appendix B, Sections B.7 and B.8.

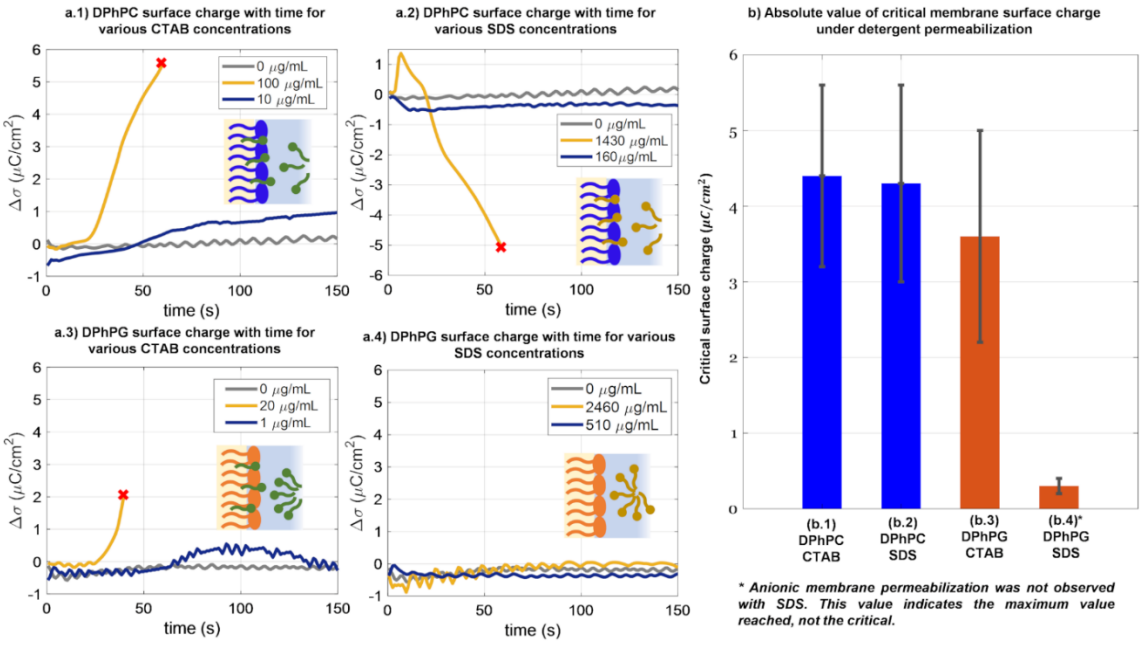


Figure 4.8: a) Example traces of membrane surface charge after injection of solubilizing detergents. Changes in the membrane surface charge with respect to time for neutral DPhPC and negatively charged 1:4 DPhPG:DPhPC membranes after injection of cationic CTAB and anionic SDS solubilizing detergents. Four cases were considered: a.1) DPhPC and CTAB, a.2) DPhPC and SDS, a.3) DPhPG and CTAB, a.4) DPhPG and SDS. For each case, three examples are shown here with varying detergent concentrations and behavior. The red marks indicate the beginning of membrane failure as observed through pore formation. Full results are found in Section SI.9. 2) The change in surface charge right before the first sign of membrane degradation is denoted as the critical surface charge. The average and standard deviation of its absolute value are shown for each case. *Note that for the case of DPhPG and SDS (2.d), this surface charge indicates the maximum value reached rather than the critical one as these cases did not show any pore formation for more than 10 minutes observation.

Figure 4.8 shows the result of membrane-detergent interactions using the presented mechanoelectricity approach. Cationic CTAB and anionic SDS solubilizing detergents were selected for testing transient adsorption behaviors as they are well-characterized in the literature [3, 4, 56, 57]**.** The 4 membrane-detergent cases considered are: neutral DPhPC membranes with cationic CTAB detergent, neutral DPhPC with anionic SDS detergent, anionic 1:4 DPhPG:DPhPC membranes with cationic CTAB, and anionic 1:4 DPhPG:DPhPC with anionic SDS. In these plots, anionic membranes are denoted as "DPhPG" for simplicity, only the first 2.5 minutes of the recordings are shown, and the red marks indicate the start of membrane disruption at which the offset measurements are halted.

Plots shown in Figure 4.8 provide representative examples, highlighting the difference in behavior depending on the membrane properties and detergent concentrations. Figure 4.8 (a.1) shows cationic CTAB disrupting DPhPC membranes. This case was observed over various detergent concentrations, where only the lowest concentration of $C_{CTAB} = 10\ \mu g/mL$ failed to solubilize the membrane. For higher concentrations, the critical surface charge required to initialize membrane permeability showed an average of $\Delta\sigma$ = + 4.4μC/cm$^2$ (± 1.2μC/cm$^2$) prior to disruption, as shown in Figure 4.8 (b.1). Following, Figure 4.8 (a.2) shows the effect of the anionic detergent SDS on these neutral membranes. Multiple detergent concentrations were adopted to test this interaction, out of which only $C_{SDS}$=160 μg/mL was unsuccessful at solubilizing the membrane even after 10 minutes. The remaining trials showed an average critical surface charge of $\Delta\sigma$ = - 4.3μC/cm$^2$ (± 1.3μC/cm$^2$), as shown in Figure 4.8 (b.2).

Figure 4.8 (a.3) shows CTAB solubilizing the negatively charged DPhPG membrane. Low concentration cases, $C_{CTAB} \leq 7\ \mu g/mL$,did not solubilize the membrane, rather a slight peak in membrane surface charge was observed, which after several minutes, converged back to the original value. Higher concentrations lead to membrane solubilization with an average critical surface charge of $\Delta\sigma$ = + 3.6μC/cm$^2$ (± 1.4μC/cm$^2$), as shown in Figure 4.8 (b.3). Finally, Figure 4.8 (a.4) shows the effect of anionic SDS detergents on DPhPG membranes. No interactions were observed in these cases. This is expected as the anionic detergent monomers are repelled from the negatively charged membrane surface.

Figure 4.8 (b) shows the average and standard deviations of the absolute value of the critical surface charge for each case. The critical surface charge is defined as the change in surface charge density right before membrane permeabilization, estimated through the offset potential. Absolute value was adopted simply to be able to compare cationic and anionic detergents noting that CTAB and SDS are both monovalent. Comparing the DPhPC cases for CTAB (b.1) and SDS (b.2), the permeabilization of this electrically neutral membrane is less dependent on the concentration of detergent within the droplet but rather on the magnitude of the change in surface charge, or detergent accumulation. For both detergents, the average critical surface charge needed to initiate membrane permeabilization was similar (P(T<=t) two tail = 0.91), even where the SDS concentration within the droplet was typically an order of magnitude higher than the amount of CTAB necessary for permeabilization.

CTAB and SDS pinch off lipids from the exoplasmic layer prior to flipping into the inner leaflet and forming pores [57]. These interactions were observed prior to any membrane deterioration through mechanoelectricity as the detergents accumulated on one surface of the membrane before successfully forming pores. The data following initial pore formation is not shown in the plots of Figure 4.8 (a) as conductance variations are not a focus of this work but rather the surface activity that precedes them.

**Characterizing membrane-melittin surface interactions**

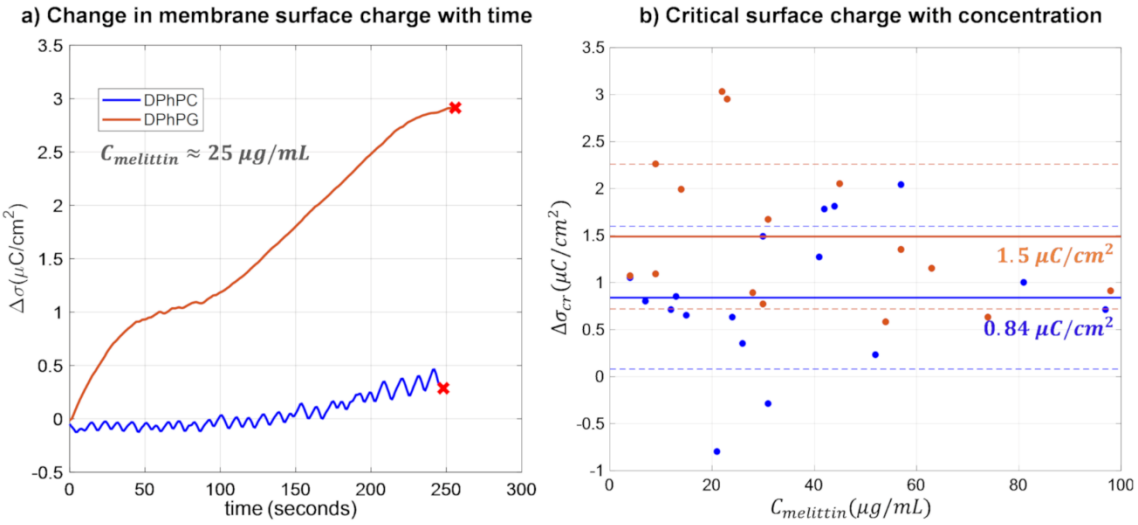


Figure 4. 9: a) An example showing the change in membrane surface charge with melittin until membrane permeabilization, for electrically neutral membrane formed with zwitterionic DPhPC phospholipids, and negatively charged membrane formed with anionic 1:4 DPhPG:DPhPC lipids mixture. Red marks indicate the beginning of membrane degradation and data beyond this point was not considered. The surface charge right before initial membrane permeabilization is denoted as the critical surface charge. b) The critical surface charge is plotted with respect to various melittin concentrations. Solid lines indicate the average value for each membrane and the dashed lines indicate the range calculated considering the standard deviations. Detailed results are shown in appendix B section B.10.

Investigating the activity of membrane-permeabilizing detergents in the previous section highlighted mechanoelectricity ability to detect accumulation prior to disruption.

In this final section, similar experiments are conducted for the antimicrobial toxin, melittin [58, 60, 64-66]. Melittin is a cationic antimicrobial peptide that permeabilizes membranes [58, 60, 66, 67], while showing different disruption mechanisms depending on the membrane electrostatics [61, 64, 68]. Herein, we utilize mechanoelectricity to examine these differences in melittin surface accumulation prior to permeabilization with varying membrane compositions.

Multiple experiments were conducted with neutral and anionic membranes, while varying melittin concentration. A total of $N$=21 and $N$=23 trials were conducted with DPhPC and DPhPG membranes, respectively. Out of which, $N$=4 (of DPhPC) and $N$=8 (of DPhPG) showed no permeabilization within 10 minutes of observations. The remaining cases showed membrane disruption leading to total failure and only these experiments were considered in our calculations. Detailed results are found in appendix B section B.10.

Figure 4. 9 (a) shows an example of the change in membrane surface charge density with respect to time for $C_{melittin}$ ~ 25μg/mL comparing DPhPC and DPhPG membranes. Note the amplified surface activity induced by melittin on the anionic surface compared to the neutral case. In this specific example, similar time was needed to initiate permeabilization, noting that this is a happenstance and was not the case for all experiments. The red marks indicate the onset of membrane poration and the corresponding surface charge was denoted as the critical surface charge and obtained for all experiments and shown in Figure 4. 9 (b). The dashed lines indicate the average value for all cases of each membrane: $\sigma_{cr} = 0.84\ \mu C/cm^2$ ($\pm 0.76 \mu C/cm^2$) was calculated for neutral membranes, compared to an average of $\sigma_{cr} = 1.5\ \mu C/cm^2$ ($\pm 0.77 \mu C/cm^2$) for anionic

membranes. This significant difference (P(T<=t) two tail = 0.02) in the surface accumulation of melittin between neutral and anionic membranes prior to the formation of pores reinforces literature findings [61, 64, 68-70], noting that anionic membranes have been observed to be more resistant to melittin permeabilization [61, 68]. Our results further support this understanding as 19% of DPhPC membranes resisted permeabilization compared to 35% of DPhPG membranes. The electrostatic attraction between the cationic peptide and the anionic membrane surface drives melittin to rapidly accumulate onto the membrane leading to a surface dominant behavior that is not observed in the case of neutral membranes [61]. A higher surface charge value indicates more peptide accumulation on the membrane leaflets as previously described in Figure 4. 2 (c). Furthermore, the average presented in Figure 4. 9 (b) can be translated into peptide-to-lipid ratio considering the charge of melittin [70] and the area per lipid of these phospholipids [71]: $P/L^{*}$~ 0.015 and 0.0085 for anionic and neutral membranes, respectively. The literature presents this characteristic in various studies [66, 67, 69, 70]. Specifically, Benachir *et al.*, showed that a $P/L$ = 0.004 is needed to release calcein from neutral liposomes, and this value increased to $P/L$ = 0.03 when 30% anionic phospholipids were added [69]. Our results produce a similar trend, while measuring accumulation prior to pore formation rather than vesicle leakage.

## Conclusion

This manuscript investigates the use of mechanoelectricity for tracking membrane disruption prior to pore formation. The approach involves exploitation of the liquid-in-liquid nature of the droplet interface bilayer for the generation of capacitance-induced

mechanoelectric current based on the voltage drop across the membrane. Continuous minimization of this current via a customized control system produces measurements of membrane disruption previously hidden in electrophysiology studies. The innovation of this approach lies within its ability to characterize membrane-nanoparticle interactions in real-time prior to membrane permeabilization.

The technique was validated against electrowetting results using asymmetric lipid membranes. Next, the technique was applied towards characterizing detergent-membrane interactions for cationic and anionic model detergents. The accumulation immediately prior to pore formation for both detergents was comparable, and the technique is able to distinguish between membrane accumulation and the concentration in the solution. Finally, the technique was applied towards the interaction of melittin within lipid membranes confirming that the peptide's insertion mechanics are modulated by membrane composition.

In each of the presented measurements for membrane accumulation the produced values are obtained prior to the formation of conductive pores. These are changes in the membrane properties that are often invisible in standard electrophysiological recordings because they are not reflected in the membrane conductance or capacitance. The mechanoelectric technique permits for measurements of membrane accumulation that may be combined with standard measurements of pore formation and provides another tool to investigate membrane permeabilization. Future research using this approach may be used to resolve crucial first steps in membrane-aided disruption for topics ranging from antimicrobial development to optimizing drug delivery vectors.

## References


1. Jenssen, H., P. Hamill, and R.E. Hancock, *Peptide antimicrobial agents.* Clinical microbiology reviews, 2006. **19**(3): p. 491-511.
2. Chamundeeswari, M., J. Jeslin, and M.L.J.E.C.L. Verma, *Nanocarriers for drug delivery applications.* 2019. **17**(2): p. 849-865.
3. Vaidyanathan, S., B.G. Orr, and M.M.J.T.J.o.P.C.B. Banaszak Holl, *Detergent induction of HEK 293A cell membrane permeability measured under quiescent and superfusion conditions using whole cell patch clamp.* 2014. **118**(8): p. 2112-2123.
4. Pata, V., et al., *Membrane solubilization by detergent: resistance conferred by thickness.* 2004. **20**(10): p. 3888-3893.
5. Lodish, H. and A. Berk, *Molecular cell biology*. Vol. 3.
6. Peetla, C., et al., *Drug resistance in breast cancer cells: biophysical characterization of and doxorubicin interactions with membrane lipids.* 2010. **7**(6): p. 2334-2348.
7. Simelane, L.P., et al., *Response of bacterial biosorbents to chemical treatment as influenced by cell membrane structure and impact on the adsorption behaviour of dyes.* 2018. **114**(4): p. 826-834.
8. Mehier-Humbert, S., et al., *Plasma membrane poration induced by ultrasound exposure: implication for drug delivery*. Journal of controlled release, 2005. **104**(1): p. 213-222.
9. Majd, S., et al., *Applications of biological pores in nanomedicine, sensing, and nanoelectronics.* 2010. **21**(4): p. 439-476.
10. Kancharala, A., et al., *A comprehensive flexoelectric model for droplet interface bilayers acting as sensors and energy harvesters.* 2016. **25**(10): p. 104007.
11. Korn, E.D.J.S., *Structure of biological membranes.* 1966. **153**(3743): p. 1491-1498.
12. Malanovic, N. and K.J.B.e.B.A.-B. Lohner, *Gram-positive bacterial cell envelopes: The impact on the activity of antimicrobial peptides.* 2016. **1858**(5): p. 936-946.
13. Shai, Y.J.B.e.B.A.-B., *Mechanism of the binding, insertion and destabilization of phospholipid bilayer membranes by α-helical antimicrobial and cell non-selective membrane-lytic peptides.* 1999. **1462**(1-2): p. 55-70.
14. Mueller, P., et al., *Reconstitution of cell membrane structure in vitro and its transformation into an excitable system.* 1962. **194**(4832): p. 979-980.
15. El-Beyrouthy, J. and E. Freeman, *Characterizing the Structure and Interactions of Model Lipid Membranes Using Electrophysiology.* 2021. **11**(5): p. 319.
16. Bunea, A.-I., et al., *Membrane interactions in drug delivery: Model cell membranes and orthogonal techniques.* 2020. **281**: p. 102177.
17. Al Nahas, K. and U.F.J.B. Keyser, *Standardizing characterization of membrane active peptides with microfluidics.* 2021. **15**(4): p. 041301.
18. Tsemperouli, M., et al., *Black lipid membranes: Challenges in simultaneous quantitative characterization by electrophysiology and fluorescence microscopy.* 2019. **35**(26): p. 8748-8757.
19. Sezgin, E.J.J.o.P.C.M., *Super-resolution optical microscopy for studying membrane structure and dynamics.* 2017. **29**(27): p. 273001.

20. Wallner, J., et al., *Application of Bio-Layer Interferometry for the analysis of protein/liposome interactions.* 2013. **72**: p. 150-154.
21. Luchini, A., et al., *Neutron Reflectometry reveals the interaction between functionalized SPIONs and the surface of lipid bilayers.* 2017. **151**: p. 76-87.
22. Biswas, N., et al., *Interplay of electrostatics and lipid packing determines the binding of charged polymer coated nanoparticles to model membranes.* 2015. **17**(37): p. 24238-24247.
23. Rusciano, G., et al., *On the interaction of nano-sized organic carbon particles with model lipid membranes.* 2009. **47**(13): p. 2950-2957.
24. Li, Y., X. Chen, and N.J.T.J.o.P.C.B. Gu, *Computational investigation of interaction between nanoparticles and membranes: hydrophobic/hydrophilic effect.* 2008. **112**(51): p. 16647-16653.
25. Lee, O.-S. and G.C. Schatz, *Computational simulations of the interaction of lipid membranes with DNA-functionalized gold nanoparticles*, in *Biomedical Nanotechnology*. 2011, Springer. p. 283-296.
26. Sekiya, Y., et al., *Electrophysiological analysis of membrane disruption by bombinin and its isomer using the lipid bilayer system.* 2019. **2**(4): p. 1542-1548.
27. Ashrafuzzaman, M., O. Andersen, and R.J.B.e.B.A.-B. McElhaney, *The antimicrobial peptide gramicidin S permeabilizes phospholipid bilayer membranes without forming discrete ion channels.* 2008. **1778**(12): p. 2814-2822.
28. Hancock, R.E. and A. Rozek, *Role of membranes in the activities of antimicrobial cationic peptides.* FEMS microbiology letters, 2002. **206**(2): p. 143-149.
29. Kagan, B.L., et al., *Antimicrobial defensin peptides form voltage-dependent ion-permeable channels in planar lipid bilayer membranes.* 1990. **87**(1): p. 210-214.
30. Wu, M., et al., *Mechanism of interaction of different classes of cationic antimicrobial peptides with planar bilayers and with the cytoplasmic membrane of Escherichia coli.* Biochemistry, 1999. **38**(22): p. 7235-7242.
31. Schoch, P., D.F. Sargent, and R. Schwyzer, *Capacitance and conductance as tools for the measurement of asymmetric surface potentials and energy barriers of lipid bilayer membranes.* The Journal of Membrane Biology, 1979. **46**(1): p. 71-89.
32. Fuks, B. and F.J.B.j. Homble, *Permeability and electrical properties of planar lipid membranes from thylakoid lipids.* 1994. **66**(5): p. 1404-1414.
33. Alvarez, O. and R. Latorre, *Voltage-dependent capacitance in lipid bilayers made from monolayers.* Biophysical journal, 1978. **21**(1): p. 1-17.
34. Hamill, O.P., et al., *Improved patch-clamp techniques for high-resolution current recording from cells and cell-free membrane patches.* 1981. **391**(2): p. 85-100.
35. Montal, M. and P. Mueller, *Formation of bimolecular membranes from lipid monolayers and a study of their electrical properties.* Proceedings of the National Academy of Sciences, 1972. **69**(12): p. 3561-3566.
36. Cevc, G., *Membrane electrostatics.* Biochimica et Biophysica Acta (BBA)-Reviews on Biomembranes, 1990. **1031**(3): p. 311-382.
37. Kinraide, T.B.J.P.P., *Use of a Gouy-Chapman-Stern model for membrane-surface electrical potential to interpret some features of mineral rhizotoxicity.* 1994. **106**(4): p. 1583-1592.

38. Clarke, R.J.J.A.i.c. and i. science, *The dipole potential of phospholipid membranes and methods for its detection.* 2001. **89**: p. 263-281.
39. Sokolov, V. and V. Mirsky, *Electrostatic potentials of bilayer lipid membranes: basic principles and analytical applications*, in *Ultrathin electrochemical chemo- and biosensors*. 2004, Springer. p. 255-291.
40. Pohl, E.E., et al., *Changes of intrinsic membrane potentials induced by flip-flop of long-chain fatty acids.* Biochemistry, 2000. **39**(7): p. 1834-1839.
41. Taylor, G., et al., *Electrophysiological interrogation of asymmetric droplet interface bilayers reveals surface-bound alamethicin induces lipid flip-flop.* Biochimica et Biophysica Acta (BBA)-Biomembranes, 2018.
42. El-Beyrouthy, J., et al., *A new approach for investigating the response of lipid membranes to electrocompression by coupling droplet mechanics and membrane biophysics.* Journal of the Royal Society Interface, 2019. **16**(161): p. 20190652.
43. Makhoul-Mansour, M.M., et al., *Photopolymerized microdomains in both lipid leaflets establish diffusive transport pathways across biomimetic membranes.* Soft matter, 2019. **15**(43): p. 8718-8727.
44. Heimburg, T., *The capacitance and electromechanical coupling of lipid membranes close to transitions: the effect of electrostriction.* Biophysical journal, 2012. **103**(5): p. 918-929.
45. Passechnik, V.I. and V.S.J.B. Sokolov, *Estimation of electrochrome dyes position in the bilayer through the 2nd harmonic of capacitive current.* 2002. **55**(1-2): p. 47-51.
46. Sokolov, V., V. Chernyi, and V.J.B. Markin, *Measurement of potential jumps on adsorption of phloretin and phlorezin on the surface of lipid membranes by the intramembrane field compensation method.* 1984. **29**(3): p. 464-470.
47. Sokolov, V. and V.J.B. Kuz'min, *Measurement of the difference in the surface potentials of bilayer membranes from the second harmonic of the capacitance current.* 1980. **25**(1): p. 174-177.
48. El-Beyrouthy, J. and E.C. Freeman. *Rapid and Real-Time Measurement of Membrane Potential Through Intramembrane Field Compensation*. in *Smart Materials, Adaptive Structures and Intelligent Systems*. 2020. American Society of Mechanical Engineers.
49. Gross, L.C., et al., *Determining membrane capacitance by dynamic control of droplet interface bilayer area.* Langmuir, 2011. **27**(23): p. 14335-42.
50. Berthier, J. and K. Brakke, *The physics of microdrops.* Scrivener-Wiley publishing. doi, 2012. **10**: p. 9781118401323.
51. Challita, E.J., M.M. Makhoul-Mansour, and E.C.J.B. Freeman, *Reconfiguring droplet interface bilayer networks through sacrificial membranes.* 2018. **12**(3): p. 034112.
52. Bayley, H., et al., *Droplet interface bilayers.* Mol Biosyst, 2008. **4**(12): p. 1191-208.
53. Poulin, P. and J. Bibette, *Adhesion of water droplets in organic solvent.* Langmuir, 1998. **14**(22): p. 6341-6343.
54. Freeman, E.C., et al., *The mechanoelectrical response of droplet interface bilayer membranes.* Soft Matter, 2016. **12**(12): p. 3021-31.

55. Grahame, D.C.J.C.r., *The electrical double layer and the theory of electrocapillarity.* 1947. **41**(3): p. 441-501.
56. Lichtenberg, D., H. Ahyayauch, and F.M.J.B.j. Goñi, *The mechanism of detergent solubilization of lipid bilayers.* 2013. **105**(2): p. 289-299.
57. Lete, M.G., et al., *Fast and slow biomembrane solubilizing detergents: Insights into their mechanism of action.* 2019. **183**: p. 110430.
58. Allende, D., S. Simon, and T.J.J.B.j. McIntosh, *Melittin-induced bilayer leakage depends on lipid material properties: evidence for toroidal pores.* 2005. **88**(3): p. 1828-1837.
59. Liu, J., et al., *Molecular details on the intermediate states of melittin action on a cell membrane.* 2018. **1860**(11): p. 2234-2241.
60. Yang, L., et al., *Barrel-stave model or toroidal model? A case study on melittin pores.* 2001. **81**(3): p. 1475-1485.
61. Pandidan, S. and A.J.S.r. Mechler, *Nano-viscosimetry analysis of the membrane disrupting action of the bee venom peptide melittin.* 2019. **9**(1): p. 1-12.
62. Najem, J.S., et al., *Activation of bacterial channel MscL in mechanically stimulated droplet interface bilayers.* Sci Rep, 2015. **5**: p. 13726.
63. Najem, J.S., et al., *Mechanics of droplet interface bilayer "unzipping" defines the bandwidth for the mechanotransduction response of reconstituted MscL*. 2017. **4**(3): p. 1600805.
64. Lee, T.H., H. Mozsolits, and M.I.J.T.J.o.p.r. Aguilar, *Measurement of the affinity of melittin for zwitterionic and anionic membranes using immobilized lipid biosensors.* 2001. **58**(6): p. 464-476.
65. Van Den Bogaart, G., et al., *On the mechanism of pore formation by melittin.* 2008. **283**(49): p. 33854-33857.
66. Lee, M.-T., et al., *Process of inducing pores in membranes by melittin.* 2013. **110**(35): p. 14243-14248.
67. Huang, H.W.J.B.j., *Free energies of molecular bound states in lipid bilayers: lethal concentrations of antimicrobial peptides.* 2009. **96**(8): p. 3263-3272.
68. Strömstedt, A.A., et al., *Effect of lipid headgroup composition on the interaction between melittin and lipid bilayers.* 2007. **311**(1): p. 59-69.
69. Benachir, T. and M.J.B.e.B.A.-B. Lafleur, *Study of vesicle leakage induced by melittin.* 1995. **1235**(2): p. 452-460.
70. Ohki, S., et al., *Interaction of melittin with lipid membranes.* 1994. **1194**(2): p. 223-232.
71. Yasmann, A. and S. Sukharev, *Properties of diphytanoyl phospholipids at the air–water interface.* Langmuir, 2014. **31**(1): p. 350-357.

# CHAPTER 5

# MODEL AND EXPERIMENTAL OBSERVATIONS OF VOLTAGE-MANIPULATED MEMBRANE NETWORKS [4]

[4] El-Beyrouthy J., Makhoul-Mansour M., Gulle J., Choe J., Wang X., Freeman E. "Model and experimental observations of voltage-manipulated membrane networks"
To be submitted to Soft Matter (2021).

**Abstract**

In this chapter, we develop a multiphysics model predicting the response of droplet-based membranes network to electrical signaling, highlighting the effect of asymmetric distribution of membranes properties and validating the model through experimental comparisons. The droplet interface bilayer (DIB) is an emulsion-based model membrane that presents unique electrical properties due to its fluidic nature. DIBs are formed at the interface of two monolayer lipid-coated droplets submerged in an organic solvent. This leads to intertwined electrostatic properties as the equilibrium of these stabilized emulsions relies on the balance of surface tensions, which may be altered by the presence of an electric field. The response of one DIB under electric stress is well studied and follows the electrowetting phenomena, where a reduction in membrane tension, and thus increase in membrane area, accommodates for the electrical energy introduced. In this manuscript, we investigate how electrowetting applies to a network of these membranes. We first explore the proposed approach through a coupled electrical-mechanical model for predicting the mechanics of networks of adhered droplets, then we validate the model by comparing it to experimental results. This work provides the first electrical-mechanical modeling of these membranes and can be expanded to further understand complex droplet mechanics and reconfigurations.

## Introduction

Droplet interface bilayers, or DIBs, are model membranes formed at the adhered interface of aqueous droplets dispersed in an oil medium [1-4]. This is possible through the dispersion of phospholipids in the aqueous phase acting as natural surfactants and forming organized lipid sheets at the water-oil interface surrounding the droplets [5]. When these lipid-coated droplets are brought into contact, they adhere forming a lipid bilayer at their interface. DIBs intertwined emulsive-membrane properties distinguishes them from other model membranes [6], allowing for advancements in the study of membrane structure and biophysics [6-10]. Importantly, DIBs enable the formation of compact networks of membranes mirroring the geometrical structure of cellular tissues through lipid bilayers interconnected in varying configurations [11, 12]. In this chapter, we form these membrane networks using DIBs and we investigate their response under electrical stimuli highlighting the intertwined membrane electrostatics and surface tension interactions.

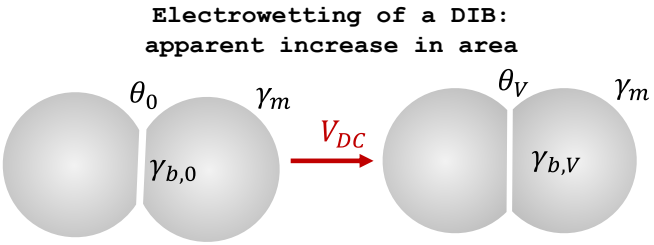


Figure 5. 1: Electrowetting of DIBs is based on the minimization of its total energy. At rest, the bilayer tension ($\gamma_b$) is balanced by the two monolayers tensions ($\gamma_m$) according to Neuman's constant specific to DIBs. In the presence of an electric field, the membrane readjusts its tension leading to an increase in the apparent membrane area and minimizing the system's total energy.

The equilibrium configuration of DIBs consistently aims at minimizing the system's total energy, considering various energetics [7]. In the absence of an applied electric field the membrane dimensions are determined by the interfacial tensions of the

bilayer and monolayer [7, 13], where the bilayer tension ($\gamma_b$) is balanced by the two monolayer tensions ($\gamma_m$) according to the Neumann's surface equilibrium [14, 15], as seen in Figure 5. 1. The balance of these surface tensions defines several membrane properties, including its wetting favorability or membrane area [16]. Electrically driven variable wetting of the membrane is possible through electrowetting, where an applied voltage across the interface temporarily increases the favorability of formation, causing the droplets to draw closer together [7, 17-20]. The new equilibrium in the presence of an external electric field is then described by introducing the electric energy to the system's total energy and determining the new minimum shape of the adhered droplet pair [13]. The coupled mechanical-electrical model introduced here considers this minimized energy and expands its feasibility to a network of DIBs, highlighting the effect of asymmetric distributions in membrane wetting.

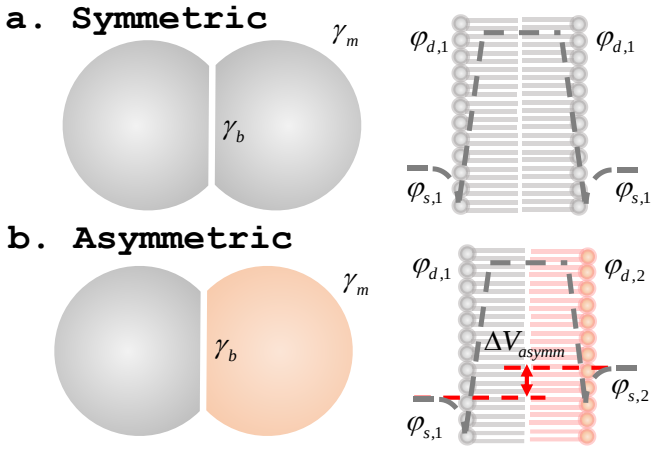


Figure 5. 2: Lipid monolayers possess localized electrical potentials dictated by the electrostatic structure of phospholipids. The lipid bilayer then possesses a transmembrane potential profile dependent on the lipids type used. a) Typically, this electrostatic profile is symmetric and the boundary potentials are equal. b) However, the DIB configuration allows for the formation of asymmetric membranes, where the two droplets contain different lipids type. This asymmetry leads to a transmembrane potential offset ($\Delta V_{asymm}$) when the membrane is short-circuited through electroctrophysiology equipements.

A recent application of interest has been the study of asymmetric bilayer interfaces undergoing electrowetting [21-23]. DIB enables the formation of asymmetric interfaces by simply varying the lipid compositions in the adjacent droplets leading to membranes with two different lipid leaflets [21, 24], as illustrated in Figure 5. 2. Since each phospholipid possesses an electrostatic profile containing dipole ($\varphi_d$) and surface ($\varphi_s$) potentials [25-27], a transmembrane potential offset is produced within the short-circuited membrane when the profiles of the two leaflets are varied . This shifts the electrowetting phenomena, causing minimal membrane dimensions at the voltage that compensates this internal offset, $\Delta V_{asymm}$ [21, 23, 28], rather than zero voltage as in the case of symmetric membranes. This variation in the electrowetting behavior is considered in our model by accounting for the asymmetric distribution in droplets wetting across the network.

In the literature, the individual membrane response to electrowetting has been studied and modeled in detail [7, 13, 29]. Additionally, the distribution of voltages within DIB networks has been successfully modeled using nodal voltage analysis [24, 25, 30], demonstrating that the membranes within the network act as voltage dividers which would drive expansion of each interface and draw the network closer together. However, wetting and voltage distributions in DIB networks, symmetric and asymmetric, have not been combined in a modeling effort to date. Herein, we combine the couple electrical-mechanical behavior of DIB networks with collections of asymmetric membranes producing offsets in the internal membrane fields. This will be explored in this chapter through a novel multiphysics model combining the electrical and mechanical properties of adhered droplet structures and confirmed through experimental replication.

## Modeling methodology

DIBs consist of two immiscible fluid phases that respond at longer time scales (>1 second) at the macrolevel, while joined together with biomolecular membranes approximately 3-5 nm thick that typically respond at considerably shorter time scales. This renders the problem ill-suited for continuum level approaches (finite element, computational fluid dynamics) and particle level (atomistic, coarse-grained). Herein, we propose a method similar to the one adapted by Brakke in the Surface Evolver model [15, 31] and later adapted for use in DIBs [32], wherein the material configuration is determined by minimization of interfacial energies. We propose coupling this with a particle-based approach wherein each droplet is capable of motion coupled with an electrical overlay to simulate electrowetting. While models exist for replicating the mechanics of droplet-based tissues [12, 33], this model allows for the incorporation of mechanical-electrical coupling by calculating the droplet-droplet forces as functions of interfacial tensions and transmembrane potentials.

### Droplet energy model

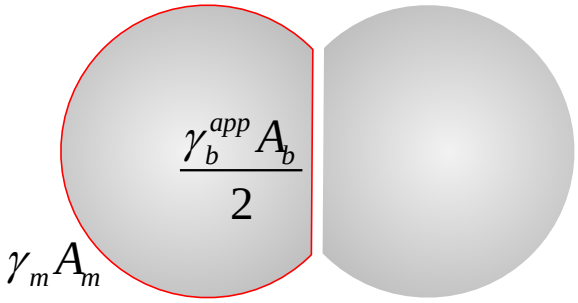


Figure 5. 3: Each droplet within the DIB possesses an interfacial energy that may be estimated by multiplying the area devoted to each interface (monolayer and bilayer) by their respective cost of formation. Monolayer tension is a constant parameter and it is obtained experimentally through tensiometry. Apparent bilayer tension relies on a base value otained through DIB microscopy but varies with electrical input.

The equilibrium structure of the droplets is based on the minimization of the interfacial energies contained within the adhered configuration, assuming negligible gravitational influence on the droplet shape. The base tension for each interface (bilayer and monolayer) are assumed to be constant and are obtained experimentally [7, 34, 35]. Any transient increases in these values due to distortion of the interfaces are assumed to occur at a faster timescale than the droplet motion. Consequently, the energy per one droplet as shown in Figure 5. 3 is written as:

$$E_{drop} = \gamma_m A_m + \frac{1}{2}\gamma_b^{app} A_b \qquad (5.1),$$

where the energy associated with a single droplet ($E_{drop}$) is equal to the monolayer tension multiplied by the monolayer area plus half the bilayer tension multiplied by the bilayer area, as the latter area is shared between two droplets. The apparent bilayer tension ($\gamma_b^{app}$) presents a base value and will be adjusted through electrowetting [13, 36-38], as described later in this methodology.

The droplet shape may be determined using the calculus of variations, examining all possible morphologies of the droplet surface bounding a fixed internal volume [39]. Unfortunately, this approach is problematic when working with adhered interfaces, as the sharp angle of contact defies a continuous description of the droplet surface. Microdroplets free of external perturbations or gravitational influences adapt a spherical shape to minimize their interfacial energetics [40], consequently we approximate each droplet using spherical cap approximations, as outlined in Appendix C, Section C.1. Once a mutually agreeable configuration is found, the total energy for the structure is calculated by multiplying the interfacial tensions by their respective areas (monolayer and bilayer).

**Electrical network model**

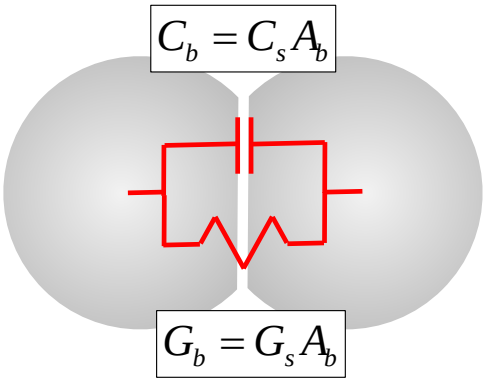


Figure 5. 4: Each membrane is approximated as a capacitor in parallel with a resistor. Values for the capacitance ($C_b$) and conductance ($G_b$) are obtained by multiplying the area of the adhered interface by standard values for the specific capacitance ($C_s$) and specific conductance ($G_s$) of lipid bilayers assumed constant.

Each membrane may be approximated as a capacitor and resistor in parallel as shown in Figure 5. 4 [28, 41]. In this model, we assume that the resistance of the droplet interior is negligible [42, 43], meaning that each droplet may be represented as a single node with a uniform voltage, *Vi*. The electrical properties of each interface are scaled from the membrane area, considering their specific capacitance and conductance, which are assumed to be constant in this model. Based on this representation, the current across each membrane is written as:

$$I = C_b\left(\frac{dV_j}{dt} - \frac{dV_i}{dt}\right) + \frac{dC_b}{dt}(V_j - V_i) + G_b(V_j - V_i) \qquad (5.2),$$

where $C_b$ is the membrane capacitance, and $G_b$ is the membrane conductance. Using nodal voltage analysis and Kirchoff's current law (KCL), the summed current entering or leaving each droplet is set to zero. The change in capacitance ($dC_b/dt$) is estimated using a backwards finite difference scheme. This creates the following system of coupled differential equations:

$$\underset{nxn}{[C]}\underbrace{\left\{\frac{dV}{dt}\right\}}_{nx1}+\left(\underbrace{[dC/dt]}_{nxn}+\underset{nxn}{[G]}\right)\underset{nx1}{\{V\}}=0$$

$$\underbrace{\left\{\frac{dV}{dt}\right\}}_{nx1}=-\underset{nxn}{[C]^{-1}}\left(\left(\underbrace{[dC/dt]}_{nxn}+\underset{nxn}{[G]}\right)\underset{nx1}{\{V\}}\right) \tag{5.3}$$

The derivative of the voltage within each droplet may be isolated by taking the inverse of the capacitance matrix [C] and multiplying it by the remaining terms. This produces a system of differential equations for the voltage within each droplet that is dependent on the voltages of their surrounding neighbors. The capacitance *($C_b$)* and conductance ($G_b$) of each membrane is calculated by multiplying the interfacial areas by values for the specific capacitance ($C_s$) and specific conductance ($G_s$), as shown in Figure 5. 4. While the specific capacitance is variable with respect to the voltage considering electrothinning [7, 36, 44], this effect is assumed negligible for simplicity and only cases with reduced residual solvent inside the membranes are simulated [13, 36].

The capacitance and conductance matrices are originally assumed to be *n* x *n* in dimension, where *n* is the total number of droplets – this assumes that an electrical connection exists between every droplet. However, terms where the interfacial area between the droplets is zero are removed from the system of equations, and the change in the droplet voltage is set to zero. Boundary conditions are applied for the source and ground droplets to produce the solution, by adding current to the source droplet to simulate charging and setting the ground droplet to a constant potential.

### Combining electrical and mechanical models

The electrical and mechanical models are combined through considering the reduction of apparent interfacial tension due to electrowetting, established by balancing the charged capacitor energy to the change in membrane surface energy. The bilayer tension for each interface is then adjusted by:

$$\gamma_b^{app} = \gamma_{b,0} - \frac{1}{2} C_s V_b^2 \qquad (5.4).$$

### Asymmetric electrowetting

The value of $V_b$ in Equation 5.5 represents the voltage across the bilayer, or the intramembrane voltage. This is defined as the difference between the voltage in the two adjacent droplets, combined with the internal field produced in the case of differences in lipid monolayers. To simulate asymmetry, each droplet entity is assigned an internal offset voltage dependent on the dissolved lipid type, defining DPhPC as the default, $V_{asymm}$ = 0 mV, and DOPhPC as $V_{asymm}$ = 135 mV. The difference between these offset voltages and between the droplets that comprise each membrane is considered when describing the total voltage across the membrane as follows:

$$V_b = \left(V_j - V_i\right) + \underbrace{\left(V_{l,j} - V_{l,i}\right)}_{\Delta V_{asymm}} \qquad (5.5).$$

While asymmetric DIBs have been characterized extensively in the literature [25, 45-48], all previous studies have involved a single membrane. Aside from one study [48], single membranes present electrodes in both droplets, clamping the boundaries to the prescribed voltage from the electrophysiology apparatus. This creates a cross-membrane electric field due to the potential difference, charging the asymmetric membrane and

alternating its area from its resting size even if no voltage is applied. The one instance in the literature without electrodes present reported that the asymmetry still enhances transport through charged membranes [48], but at a lower rate. This suggests that asymmetric membranes are not necessarily charged in isolation as the asymmetry in the membrane is thus produced by separation of charged groups within the lipid leaflets, typically divided into dipole and surface contributions [49]. Each droplet containing a lipid monolayer and dissolved salts is assumed to be initially electroneutral. Therefore, while there is a difference in the potential at the boundaries within the droplet interior, this does not produce an electric field across the membrane associated with electrowetting, and the initial bilayer tension and geometry upon formation remains unmodified. This aligns with experimental observations in the literature, and is linked to the spatial variations in the electrostatic potential across the membrane surface [50].

**Solution**

To estimate the forces on each droplet, their locations are minutely perturbed in the *x*, *y*, and *z* directions and the change in the energy per droplet is calculated. These changes are used to estimate the gradient of the internal energy for each droplet using finite central difference approximations, and the negative gradient of the energy produces the force on each droplet [38, 51] associated with capillary effects, as follows:

$$\vec{F}_{E,drop} \approx -\vec{\nabla}E_{drop} \approx -\begin{Bmatrix} \dfrac{E_{drop}\left(x+\Delta x,y,z\right)-E_{drop}\left(x-\Delta x,y,z\right)}{2\Delta x} \\ \dfrac{E_{drop}\left(x,y+\Delta y,z\right)-E_{drop}\left(x,y-\Delta y,z\right)}{2\Delta y} \\ \dfrac{E_{drop}\left(x,y,z+\Delta z\right)-E_{drop}\left(x,y,z-\Delta z\right)}{2\Delta z} \end{Bmatrix} \qquad (5.6).$$

This force is then combined with a single damping dependent on the current droplet velocity defined by a viscous damping coefficient $\beta$. While we recognize that there are multiple damping forces present involved in the combination of immiscible fluids and droplet wetting [52], this damping value is simply added to produce dissipation and replicate the observed behavior of the droplets.

Furthermore, we assume that the inertial effects are negligible. Droplets are exceedingly small in mass, and they will rapidly reach their terminal velocity as described by Durian [53]. Consequently, the velocity is directly taken from the necessary drag force for counterbalancing the forces estimated from the previous equation, greatly reducing the necessary computational time for integration. Friction between the droplets is assumed negligible since the lipids are able to glide laterally across there adhered surfaces [54]. Thus, droplets velocity is expressed as:

$$\sum \vec{F}_{drop} = 0 = \vec{F}_{E,drop} - \vec{v}\beta$$
$$\vec{v} = \frac{\vec{F}_{E,drop}}{\beta} \qquad (5.7).$$

The result is a large collection of differential equations, which is then integrated using Runge-Kutta methods, specifically Dormand-Prince as described in Appendix C, Section C.2. Results are then post-processed and plotted in MATLAB for visualization when desired. Tracked variables include the voltage within each droplet, transmembrane potentials, current supplied across the electrodes, and membrane dimensions in response to perturbation.

## Model inputs

Simulation input values (summarized in Table 5.1) are based on water droplets containing DPhPC or DOPhPC phospholipids and buffer solutions dispersed in a continuous hexadecane phase. Values for the monolayer and bilayer tension are obtained from previous experimental works [7, 13]. The damping coefficient which serves to regulate droplet motion and vibrations is selected to best match experimental behaviors. Values for the specific capacitance and specific conductance are supplied for DPhPC-Hexadecane combinations in DIBs and are the established baselines for these values from multiple studies [7, 13, 36, 42, 44, 55].

Table 5.1: Model inputs utilized to predict the electrowetting behavior of symmetric DPhPC and asymmetric DOPhPC-DPhPC membrane networks in hexadecane oil.

| Variable | Value | Source |
|---|---|---|
| Monolayer Tension ($\gamma_m$) | 1.18 mN/m | Expected Range [7, 13] |
| Bilayer Tension ($\gamma_b$) | 2.04 mN/m | Expected Range [7, 13] |
| Damping ($\beta$) | ~$10^{-3}$ Ns/m | Variable, Curve-Fitting |
| Specific Capacitance ($C_s$) | 0.6 μF/cm$^2$ | Expected Range [7, 13, 36, 44] |
| Specific Conductance ($G_s$) | 10 nS/cm$^2$ | ~GΩ Range [42, 55, 56] |

## Experimental methodology and materials

### Lipid solutions

Lipids-in-droplets are prepared by first dissolving 250 mM of potassium chloride (KCl, ≥99.1%—Sigma-Aldrich) with 10 mM MOPS (of 3-(N-Morpholino) propane sulfonic acid (MOPS, ≥99.5%—Sigma-Aldrich) in DI water. DPhPC (1,2-diphytanoyl-sn-glycero-3-phosphocholine) is purchased in its powder form from Avanti Polar Lipids. The

powder is directly mixed with the aqueous buffer solution leading to the desired 2 mg/mL lipids-in-water concentration. DOPhPC (1,2-di-O-phytanyl-sn-glycero-3-phosphocholine) is purchased dissolved in chloroform at a concentration of 10 mg/mL. The calculated volume is extracted and placed in a glass vial where chloroform is evaporated through a two-step process: argon gas exposure followed by placing the vial in a vacuum chamber overnight. The resulting dry lipid films are then hydrated with the buffer solution leading to a 2 mg/mL concentration.

Once the lipids are dispersed, at least 4 freeze– thaw cycles (freeze at -20◦C, and thaw at room temperature) are performed to ensured proper distribution of liposomes. Before usage, the needed volume is extracted and sonicated using a probe tip sonicator (Q55 QSONICA, LLC), ensuring smaller and evenly distributed liposomes. Finally, the solvent adopted here is hexadecane oil (Sigma-Aldrich) as it has been proven to create solvent-free membranes reassuring the constant thickness assumption [36].

**Network assembly**

Large circular (2.5 x 2.5 x 0.3 cm) polyurethane dishes are adhered to a glass slide and used as the oil reservoir for membrane network assembly. Glass capillary tubes (1 mm wide) are sharpened to fine tips, filled with the desired lipid solution, and connected to a microinjector for droplets formation and positioning. Micromanipulators are strategically placed around the oil dish allowing for adjustment of pipette location in the dish. The droplet is then slowly formed at its desired size and left hanging mid-depth of the well for a few minutes allowing for lipid monolayer formation. This ensures the lipids coating on the droplet inhibiting droplets total wetting at the glass surface. For asymmetric networks, the microinjector is flushed with DI water prior to switching solutions avoiding cross-

solution contamination in the microinjector. Once the droplets are placed in their approximate end position, the network is formed by bringing the droplets into contact. The formation and characterization of the network is then observed through microscopy and electrophysiology as will be discussed in the following paragraphs.

## Electrophysiology

Electrodes are prepared by submerging 125 μm silver wires in sodium hypochlorite (NaClO) solution for several minutes forming silver/silver-chloride (Ag/Ag-Cl) electrodes. The tips are then dipped in agarose hydrogel (2.5% w:v low EEO, Sigma-Aldrich Co.) allowing for improved adhesion of the droplets and enhanced electrical conductance. Care must be taken not to add excess agarose at the electrodes tip to not interfere with the size and shape of the droplets. The input electrode is connected to the headstage of the Axopatch amplifier, while the other one is connected to the ground. Noise is excluded from the electrical signal by grounding the equipment and by placing the membrane network and both electrodes within a Faraday cage. Electrophysiology is conducted using an axopatch amplifier connected back to a Digidata 1440 (Molecular Devices). This analogue input/output reader provides the voltage signal and reads the membrane-generated current. The sinusoidal voltage provided in these experiments had an amplitude of 5-mV and a frequency of 40-Hz.

## Microscopy

An inverted microscope is utilized to observe the formed network and responses to the applied voltage. This light microscopy allows for clear images of the network and its rearrangements. Depending on the size and the location of the droplets, an amplification of x4 or x6.4 is utilized to observe changes in droplets location and membrane size. Obtaining

the bottom view of the droplets allows for exact contact angle measurements [7], as they are seen as perfect circles. Frames are captured at 0.5 frames per second, and videos are extracted with 3 frames per second, leading to videos 6x faster than real-time.

## Results and discussion

### Asymmetric electrowetting predictions

First, we model the change in single membrane area with voltage for symmetric and asymmetric two-droplets cases. This is accomplished by generating the two droplets, including their corresponding potentials, dimensions and surface tensions, then plotting the change in the interfacial area with respect to a specified voltage range (-250 to +250 mV). Electrowetting in droplets is defined by the following equation [47, 57]:

$$A_b = A_0(1 + \alpha V_b^2) \qquad (5.8).$$

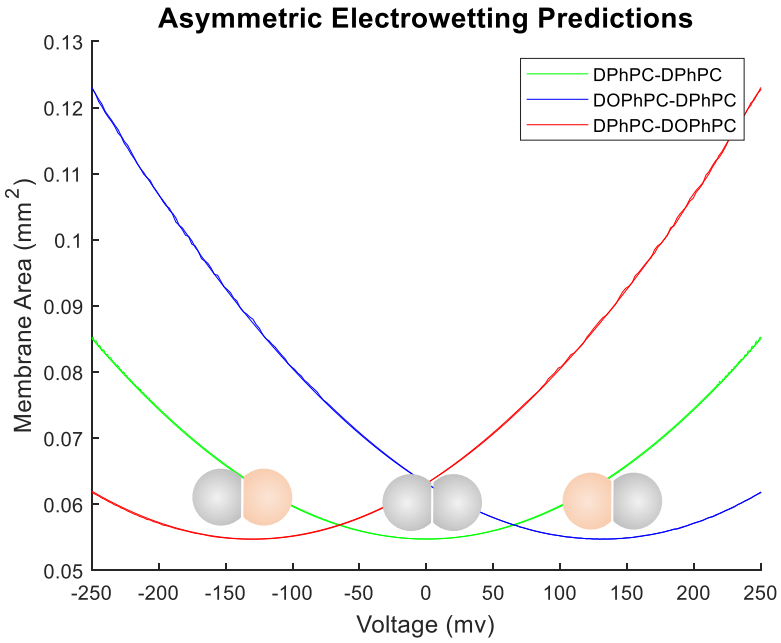


Figure 5. 5: Simulated behavior of membrane area with voltage using our developed model. Results obtained follow the expected parabola equation, where each case is centered at the transmembrane potential offset, $\Delta V_{asymm}$. In the case of symmetric membrane shown in

green, the plot is centered at 0 mV, whereas asymmetric membranes are centered at positive and negative 135 mV corresponding to the monolayer offset introduced for DOPhPC droplets. The model successfully differentiates between DOPhPC monolayer on the electrical ground versus the input by switching the offset sign.

We simulate the response of a symmetric (DPhPC) and two asymmetric membranes where droplets with varying internal potentials produce a 135-mV offset (DPhPC and DOPhPC [47, 58, 59]). These behaviors are well-documented in the literature and serve as simple calibration cases. As shown in Figure 5. 5, the change in the membrane area is well approximated by a quadratic relationship (Equation 5.8), where the minimum capacitance indicates the asymmetric potential. This phenomenon is unsurprising, since this is an energy minimization experiment replicated within a dynamic environment. These results provide reassurance that the equations are based on simple physical principals and reproduce observed experimental phenomena, and that describing the behavior of the droplets through minimization of their interfacial energy captures their behavior [38].

**Asymmetric two-droplets membrane**

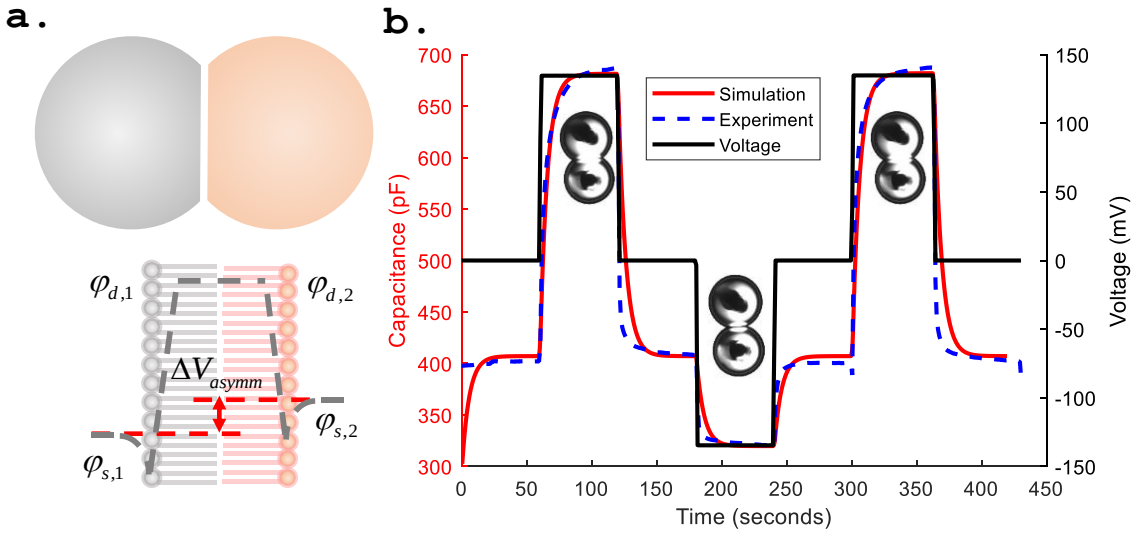


Figure 5. 6: a) DPhPC and DOPhPC droplets form an asymmetric bilayer at their adhered interface. b) This leads to the generation of an internal electric field across the membrane shifting the electrowetting behavior to be centered at the voltage compensating this offset,

$\Delta V_{asymm}$. c) Simulated and experimental total capacitance for the asymmetric membrane under voltage steps are shown, and their significantly similar behavior further validates our model.

Next, we compare the simulated response of an asymmetric membrane to its experimental behavior. Single lipid membrane was formed using DPhPC-DOPhPC phospholipids, where the latter monolayer corresponds to the electrical ground side. Based on our results shown in Chapter 3, having the DOPhPC monolayer on the ground side leads to a membrane offset of a positive value ($\Delta V_{asymm}$ = 135 mV). This centers the parabola at negative 135 mV, leading to the smallest membrane area, as seen in Figure 5. 5. The following voltage inputs are introduced in the experimental work: 0 and +/-135 mV, each held for 60 seconds. This voltage input is then utilized as the input of the model.

Figure 5. 6 (c) shows the results of the model (red line) and experimental data (blue dotted line). The black curve indicates the applied voltage. Note that the lowest capacitance value is indeed obtained at the negative voltage, as this voltage is the closest to compensate for the membrane's potential offset as expected from the electrowetting equation. Simulated and experimental results are well compatible highlighting our model's ability to predict the capacitance change of asymmetric membranes.

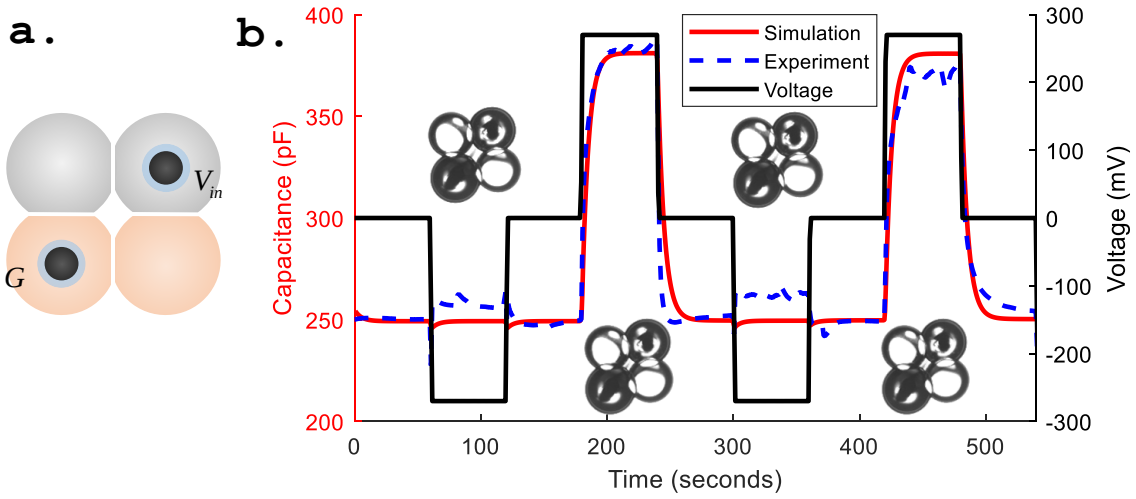


Figure 5. 7: a) Four-droplets asymmetric network is formed by having 2 DOPhPC-dispersed droplets, including the ground droplet, placed in parallel with 2 DPhPC-dispersed droplets, including the input droplet. b) Simulated and experimental capacitance as well as the applied voltage are shown with respect to time. Results show significant compatibility between the expected network total capacitance and its experimentally calculated value.

Next, we explore a larger network of droplets, demonstrating electrowetting and directional compaction in asymmetric membranes network. This has not been investigated in the literature and represents a novel approach to adjustable adhesion in these droplet-based membranes. In these cases, the phenomenon is not as straight forward as single membranes, as the distribution of voltages are dependent on the distribution of membrane area and vice versa, producing complex coupled behaviors. The case investigated herein involves two parallel chains of droplets containing two membranes each.

Four droplets are deposited as shown in Figure 5. 7 (a). Asymmetric membranes are produced by using two droplets containing DPhPC (grey droplets), and two containing DOPhPC (pink droplets). Figure 5. 7 (b) presents the voltage overlapped with the simulated and experimental network capacitance. Similar to the two-droplets case, 0 and +/-270 mV

were cyclically applied for 60 seconds each. Note that 270 mV is applied here instead of 135 mV as the electric field is divided in this configuration across two membranes in series.

Since the ground droplets correspond to DOPhPC lipids, we expect the lowest capacitance to occur at the negative voltage as in the two-droplets case of Figure 5. 6 (b). However, Figure 5. 7 (b) shows that the network capacitance is almost the same (~250 pF and ~260 pF) for zero and negative voltages, and significantly higher (~375 pF) for the positive voltage. This behavior fundamentally highlights a unique property in asymmetric networks under electrowetting: directional contraction due to uneven wetting in two dimensions. In fact, the network shown herein ultimately presents two symmetric (intramembrane field compensated at 0 mV) and two asymmetric (intramembrane field compensated at negative 135 mV) membranes. Thus, at 0 mV, the droplets forming the asymmetric membranes are compact and compressing towards each other whereas those forming the symmetric membranes are in their relaxed state. The opposite is true when a negative voltage is applied. At negative 270 mV, the droplets compaction is switched from asymmetric to symmetric membranes which are now wetting a larger area leading to droplets compression. However, even though the compaction is switched, the overall electrowetting across the network is maintained. This is denoted as directional compaction and is visible in the droplets network. Since all droplets are formed relatively with the same size, the total membrane capacitance remains almost the same, as seen in Figure 5. 7 (b). The significant increase in network capacitance is then observed when all four droplets are compressed at the positive voltage, while asymmetric membranes are under a higher electrocompression than symmetric ones as shown in Figure 5. 5.

In summary, the results shown in Figure 5. 5, Figure 5. 6, and Figure 5. 7 are satisfying, as a general agreement is clear between the model and experimental results. We do not ignore the discrepancies due to the more complex phenomena present in the experimental data, but the overall trend is replicated. Therefore, we can confidently use the produced model to predict the behavior of DIB networks under electrowetting and move towards larger and more complex networks and utilizing the directional compaction phenomenon.

## Conclusions

In this chapter, we develop and test a coupled electrical-mechanical model for networks of adhered droplets exploring voltage-driven manipulations in membrane networks. This model is built on the principle of minimizing interfacial energies in emulsive systems and allows for predictions of coupled mechanical and electrical effects through electrowetting phenomenon. While previous research efforts successfully modeled the electrical properties of these membranes as networks of capacitors and resistors, this represents the first model to link these electrical elements to the geometries of the adhered droplets and use them to successfully simulate electrowetting. Electrowetting reduces the apparent tension across the interfaces, causing the network to dynamically adjust and contract. Herein, we validate the developed model by simulating two-droplets asymmetric membrane and four-droplets asymmetric network as a first step towards utilizing the model for more complex and bio-inspired systems.

## References


1. Poulin, P. and J. Bibette, *Adhesion of water droplets in organic solvent.* Langmuir, 1998. **14**(22): p. 6341-6343.
2. Bayley, H., et al., *Droplet interface bilayers.* Mol Biosyst, 2008. **4**(12): p. 1191-208.
3. Funakoshi, K., H. Suzuki, and S. Takeuchi, *Lipid bilayer formation by contacting monolayers in a microfluidic device for membrane protein analysis.* Analytical chemistry, 2006. **78**(24): p. 8169-8174.
4. Booth, M.J., et al., *Functional aqueous droplet networks.* 2017. **13**(9): p. 1658-1691.
5. Israelachvili, J.N., D.J. Mitchell, and B.W.J.B.e.B.A.-B. Ninham, *Theory of self-assembly of lipid bilayers and vesicles.* 1977. **470**(2): p. 185-201.
6. El-Beyrouthy, J. and E. Freeman, *Characterizing the Structure and Interactions of Model Lipid Membranes Using Electrophysiology.* 2021. **11**(5): p. 319.
7. El-Beyrouthy, J., et al., *A new approach for investigating the response of lipid membranes to electrocompression by coupling droplet mechanics and membrane biophysics.* Journal of the Royal Society Interface, 2019. **16**(161): p. 20190652.
8. Najem, J.S., et al., *Activation of bacterial channel MscL in mechanically stimulated droplet interface bilayers.* Sci Rep, 2015. **5**: p. 13726.
9. Kancharala, A., et al., *A comprehensive flexoelectric model for droplet interface bilayers acting as sensors and energy harvesters.* 2016. **25**(10): p. 104007.
10. Mruetusatorn, P., et al., *Dynamic morphologies of microscale droplet interface bilayers.* Soft Matter, 2014. **10**(15): p. 2530-2538.
11. Challita, E.J., et al., *Encapsulating Networks of Droplet Interface Bilayers in a Thermoreversible Organogel.* Scientific reports, 2018. **8**.
12. Villar, G., A.D. Graham, and H.J.S. Bayley, *A tissue-like printed material.* 2013. **340**(6128): p. 48-52.
13. Taylor, G.J., et al., *Direct in situ measurement of specific capacitance, monolayer tension, and bilayer tension in a droplet interface bilayer.* Soft Matter, 2015. **11**(38): p. 7592-605.
14. Style, R.W. and E.R. Dufresne, *Static wetting on deformable substrates, from liquids to soft solids.* Soft Matter, 2012. **8**(27): p. 7177.
15. Berthier, J., *Micro-drops and digital microfluidics*. 2012: William Andrew.
16. Aronson, M. and H. Princen, *Contact angles associated with thin liquid films in emulsions.* Nature, 1980. **286**(5771): p. 370.
17. Quilliet, C. and B. Berge, *Electrowetting: a recent outbreak.* Current Opinion in Colloid & Interface Science, 2001. **6**(1): p. 34-39.
18. Mugele, F. and J.-C. Baret, *Electrowetting: from basics to applications.* Journal of Physics: Condensed Matter, 2005. **17**(28): p. R705-R774.
19. Punnamaraju, S. and A.J.J.L. Steckl, *Voltage control of droplet interface bilayer lipid membrane dimensions.* 2011. **27**(2): p. 618-626.
20. Tamaddoni, N., et al., *Reversible, voltage-activated formation of biomimetic membranes between triblock copolymer-coated aqueous droplets in good solvents.* 2016. **12**(23): p. 5096-5109.

21. Taylor, G., et al., *Electrophysiological interrogation of asymmetric droplet interface bilayers reveals surface-bound alamethicin induces lipid flip-flop.* Biochimica et Biophysica Acta (BBA)-Biomembranes, 2018.
22. Challita, E.J. and E.C.J.L. Freeman, *Hydrogel Microelectrodes for the Rapid, Reliable, and Repeatable Characterization of Lipid Membranes.* 2018. **34**(50): p. 15166-15173.
23. Mosgaard, L.D., K.A. Zecchi, and T.J.S.M. Heimburg, *Mechano-capacitive properties of polarized membranes.* 2015. **11**(40): p. 7899-7910.
24. Hwang, W.L., et al., *Asymmetric droplet interface bilayers.* 2008. **130**(18): p. 5878-5879.
25. Freeman, E.C., et al., *The mechanoelectrical response of droplet interface bilayer membranes.* Soft Matter, 2016. **12**(12): p. 3021-31.
26. Ermakov, Y.A. and A. Nesterenko. *Boundary potential of lipid bilayers: methods and interpretations*. in *Journal of Physics: Conference Series*. 2017. IOP Publishing.
27. Cevc, G., *Membrane electrostatics.* Biochimica et Biophysica Acta (BBA)-Reviews on Biomembranes, 1990. **1031**(3): p. 311-382.
28. Schoch, P., D.F. Sargent, and R. Schwyzer, *Capacitance and conductance as tools for the measurement of asymmetric surface potentials and energy barriers of lipid bilayer membranes.* The Journal of Membrane Biology, 1979. **46**(1): p. 71-89.
29. Najem, J.S., et al., *Dynamical nonlinear memory capacitance in biomimetic membranes.* 2019. **10**(1): p. 1-11.
30. Creasy, M.A., et al., *Deterministic model of biomolecular networks with stimuli-responsive properties.* Journal of Intelligent Material Systems and Structures, 2015. **26**(8): p. 921-930.
31. Brakke, K.A.J.E.m., *The surface evolver.* 1992. **1**(2): p. 141-165.
32. Challita, E.J., M.M. Makhoul-Mansour, and E.C.J.B. Freeman, *Reconfiguring droplet interface bilayer networks through sacrificial membranes.* 2018. **12**(3): p. 034112.
33. Zhang, T., et al., *Shape-shifting droplet networks.* 2016. **116**(10): p. 108301.
34. Makhoul-Mansour, M., et al., *Ferrofluid-Based Droplet Interface Bilayer Networks.* Langmuir, 2017. **33**(45): p. 13000-13007.
35. Berry, J.D., et al., *Measurement of surface and interfacial tension using pendant drop tensiometry.* J Colloid Interface Sci, 2015. **454**: p. 226-37.
36. Gross, L.C., et al., *Determining membrane capacitance by dynamic control of droplet interface bilayer area.* Langmuir, 2011. **27**(23): p. 14335-42.
37. Anklam, M., D. Saville, and R. Prud'Homme, *Disjoining Pressure and Film Tension in Comb− Graft Copolymer-Stabilized Oil Films.* Langmuir, 1999. **15**(21): p. 7299-7307.
38. Bahadur, V. and S. Garimella, *An energy-based model for electrowetting-induced droplet actuation.* Journal of Micromechanics and Microengineering, 2006. **16**(8): p. 1494.
39. Lacasse, M.D., G.S. Grest, and D. Levine, *Deformation of small compressed droplets.* Phys Rev E Stat Phys Plasmas Fluids Relat Interdiscip Topics, 1996. **54**(5): p. 5436-5446.

40. Berthier, J. and K.A. Brakke, *The physics of microdroplets*. 2012: John Wiley & Sons.
41. Alvarez, O. and R. Latorre, *Voltage-dependent capacitance in lipid bilayers made from monolayers.* Biophysical journal, 1978. **21**(1): p. 1-17.
42. Creasy, M.A., et al., *Deterministic model of biomolecular networks with stimuli-responsive properties.* Journal of Intelligent Material Systems and Structures, 2014: p. 1045389X14536004.
43. Challita, E.J., M.M. Makhoul-Mansour, and E.C. Freeman, *Reconfiguring droplet interface bilayer networks through sacrificial membranes.* Biomicrofluidics, 2018. **12**(3): p. 034112.
44. Beltramo, P.J., L. Scheidegger, and J. Vermant, *Towards realistic large area cell membrane mimics: Excluding oil, controlling composition and including ion channels.* Langmuir, 2018.
45. Najem, J.S., et al., *The voltage-dependence of MscL has dipolar and dielectric contributions and is governed by local intramembrane electric field.* Scientific Reports, 2018. **8**(1): p. 13607.
46. Najem, J.S., et al., *Dynamical nonlinear memory capacitance in biomimetic membranes.* Nature communications, 2019. **10**(1): p. 1-11.
47. Taylor, G., et al., *Electrophysiological interrogation of asymmetric droplet interface bilayers reveals surface-bound alamethicin induces lipid flip-flop.* Biochimica et Biophysica Acta (BBA) - Biomembranes, 2018.
48. Li, X., et al., *Peptide-Mediated Membrane Transport of Macromolecular Cargo Driven by Membrane Asymmetry.* Anal Chem, 2017.
49. Cevc, G., *Membrane electrostatics.* Biochim Biophys Acta, 1990. **1031**(3): p. 311-82.
50. Aguilella, V.M. and S.M. Bezrukov, *Alamethicin channel conductance modified by lipid charge.* European Biophysics Journal, 2001. **30**(4): p. 233-241.
51. Zhang, T., et al., *Shape-shifting droplet networks.* arXiv preprint arXiv:1505.01108, 2015.
52. Li, Y.-J., et al., *Non-linearity and dynamics of low-voltage electrowetting and dewetting.* Physical Chemistry Chemical Physics, 2019. **21**(33): p. 18290-18299.
53. Durian, D.J., *Foam mechanics at the bubble scale.* Physical review letters, 1995. **75**(26): p. 4780.
54. Zhang, H. and H. Makse, *Jamming transition in emulsions and granular materials.* Physical Review E, 2005. **72**(1): p. 011301.
55. Creasy, M.A., *Bilayer Network Modeling*. 2011, Virginia Polytechnic Institute and State University.
56. Hwang, W.L., et al., *Electrical behavior of droplet interface bilayer networks: experimental analysis and modeling.* Journal of the American Chemical Society, 2007. **129**(38): p. 11854-11864.
57. El-Beyrouthy, J. and E. Freeman, *Characterizing the Structure and Interactions of Model Lipid Membranes Using Electrophysiology.* Membranes, 2021. **11**(5): p. 319.
58. Yasmann, A. and S. Sukharev, *Properties of diphytanoyl phospholipids at the air-water interface.* Langmuir, 2014.

59. Challita, E.J. and E.C. Freeman, *Hydrogel Microelectrodes for the Rapid, Reliable, and Repeatable Characterization of Lipid Membranes.* Langmuir, 2018.

# CHAPTER 6

# CONCLUSION

Electrophysiology is a useful tool for the characterization of model lipid membranes, translating the recorded membrane electrical responses to membrane properties and structure. The droplet interface bilayer (DIB) is a model membrane whose unique composition introduces an additional layer of complexity as these soft membranous systems are stabilized water-in-oil emulsions. This dissertation investigates traditional electrophysiology characterization tools and showcases the development and implementation of novel techniques by utilizing the fluidic properties of the DIB.

This dissertation advanced the field of membrane electrophysiology for DIBs beyond the traditional understandings in various ways. First, it comprehensively investigated model membrane formation methodologies focusing on their resulting properties and how these properties influence membrane electrophysiology. Then, a new technique for inferring changes in lipids lateral packing under electrocompression was presented. This was possible through an improved DIB experimental setup allowing for full visualization of the droplet geometries, and thus of the membrane energetics Analyzing changes in the membrane energetics under electrocompression for various lipid compositions was utilized as a proof-of-concept for the use of this novel approach studying membrane lateral rearrangements. Following these equilibrium studies was a dynamic study of the membrane transient mechanics in the presence of a membrane-active agent.

DIB's mechanoelectricity property allows for the rapid, real-time, and continuous detection of cross-membrane potential offset which is translated into membrane surface interactions. This allowed for the investigation of membrane solubilization mechanics prior to initial signs of membrane poration. Finally, the response of a network of DIBs under electric manipulations was modeled and validated through experimental examinations. The electrical response of a DIB follows the electrowetting effect where the system adjusts its geometry to minimize its total energy, including surface tension and electrical stress. This concept is adopted and expanded to a network of these model membranes, interestingly investigating how membrane asymmetry within the network can be utilized for droplets reconfigurations and membrane electrical manipulations.

# APPENDIX A

# A NEW APPROACH FOR INVESTIGATING THE RESPONSE OF LIPID MEMBRANES TO ELECTROCOMPRESSION BY COUPLING DROPLET MECHANICS AND MEMBRANE BIOPHYSICS

## SUPPLEMENTARY INFORMATION [2]

[2] El-Beyrouthy, J., et al. (2019). "A new approach for investigating the response of lipid membranes to electrocompression by coupling droplet mechanics and membrane biophysics." Journal of the Royal Society Interface **16**(161): 20190652.
Reprinted with the permission of publisher.

## Lipid solutions preparation

Lipid-in solutions were used in all the experiments, where lipids are dispersed in the aqueous phase as compared to lipids-out where lipids would be dispersed in oil [1]. Buffer solutions were first prepared by mixing 500 mM of potassium chloride (KCl, ≥ 99.1% – Sigma-Aldrich) and 10 mM of 3-(N-Morpholino) propane sulfonic acid (MOPS, ≥ 99.5% – Sigma-Aldrich) in distilled water. Then, for solutions containing DPhPC (1,2-diphytanoyl-sn-glycero-3-phosphocholine – Avanti Polar Lipids) only, the phospholipids stored at -20°C were directly mixed with the buffer solution at a concentration of 2.0 mg/mL. A minimum of six freeze-thaw cycles were used to reduce aggregation in the solution. Extrusion was performed immediately before experiments to ensure uniform liposome dimensions. For solutions containing cholesterol, DPhPC and cholesterol (ovine wool, >98% – Avanti Polar Lipids) were each dispersed in chloroform first, and then volumes of the solutions were mixed depending on the desired cholesterol mole fraction. After mixing the two lipids in a glass vial, the chloroform was evaporated by applying argon gas. To ensure total evaporation, the vial was also placed under vacuum for a few hours. The lipids were then hydrated with the buffer solution and stored at -20$^{o}$C. The solutions were then subjected to the same six freeze-thaw cycles. At this point, cholesterol may still be in its crystalized form, and since extrusion may remove cholesterol crystals [2], sonication was used instead to break down dispersed lipid aggregates. A probe sonicator (Q55 QSONICA, LLC) was used and sonication was performed over cycles, each lasting 2 minutes with 2 minutes in between to prevent overheating of the solution. The cycles were repeated until the solution became transparent. Sonicator tip, syringes used for extrusion and the O-ring channel were cleaned using isopropanol or acetone, rinsed with

DI water then placed until air flow to ensure total alcohol evaporation. Oil cuvettes and dishes were cleaned between each experiment using soap (Laboratory detergent for sparkleen clean glassware, Fisher scientific) then rinsed with DI. Solutions were prepared with 0, 10, 20, and 30% mole fraction cholesterol in DPhPC. The maximum cholesterol mole fraction adopted in this work was 30% ensuring cholesterol solubility in phospholipids and avoiding cholesterol crystals precipitation [3-5]. Hexadecane (99% – Sigma-Aldrich) was used as the primary oil phase, as it has shown to handle stable bilayers in addition to its relatively large molecule enabling the assumption of a relatively solvent-free model membrane [6, 7].

**Pendant drop tensiometry technique**

Monolayer surface tensions were measured using the pendant drop technique [8], which relies on the balance between surface tension and gravitational force. When an aqueous droplet is suspended inside a lower density medium, surface tension attempts to minimize the droplet's surface area while gravity pulls it downwards. This balance of tension and gravitational influence produces a pendant-shaped droplet. Measuring the contour of the droplet and the density of the two phases allows for the estimation of the surface tension at the oil-water interface. Based on this concept, the experimental apparatus consists of an aqueous droplet suspended from a needle inside a 3 mL glass cuvette containing the desired oil. Once the droplet is expelled from the needle into the oil reservoir, lipids molecules migrate towards the water-oil interface forming the monolayer and decreasing the surface tension. The droplet's shape gradually sags from a spherical shape to a pendant shape as the lipid monolayer develops.

This process is recorded using a zoom lens camera (6.5X zoom lenses with a 0.7−4.5× magnification range, Thorlabs). Frames are extracted using MATLAB and then used to obtain the interfacial tension by the open-source tensiometry software OpenDrop [8, 9]. Between experiments and to avoid any contamination, the needles were first washed with DI water, then isopropanol or acetone, then again with DI water and placed under vacuum to ensure complete evaporation.

The success of each experiment was determined by two dimensionless numbers, the Worthington and Bond number. The Worthington number is the ratio of the calculated droplet volume to the maximum volume each needle size can withstand without droplet falling [8]. A value higher than 0.6 indicates acceptably accurate measurements. Since the lipid monolayers measured here are prone to detaching from the needle prior to reaching equilibrium due to the sharp reduction in surface tension, a value as low as 0.4 was also accepted when using needles with a diameter greater than 0.51 mm [8]; however most measurements satisfied the > 0.6 criteria. The Bond number is the ratio of the gravitational force to the surface tension, which must have a value of 0.3 or higher. Any experiment with a Worthington number or a Bond number lower that 0.4 or 0.3, respectively, was not used. The capability to vary the needle dimensions and the magnification provided allows for the assessment of low surface tension cases which otherwise would be problematic.

## Monolayer surface tension results

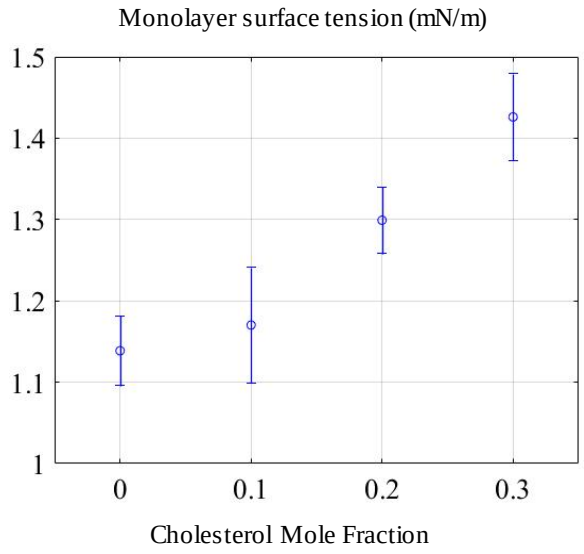


Figure A. 1: Monolayer surface tension – mean value and standard deviations – with hexadecane oil for different cholesterol percentages.

The monolayer surface tension with varying lipid compositions was measured through the pendant drop tensiometry. Figure A. 1 shows the interfacial tension average value and interval of error, whereas Table A.1 shows all the values considered. Each data point tabulated represents the stable surface tension value calculated from one separate experiment. An experiment is considered successful when the hanging droplet is stable – not shrinking up nor falling down – for more than ten minutes. High resolution frames of the pendant droplet, the exact size of the needle used as well as the exact oil and water densities are key for accurate calculations. Before accepting the tension value, Bond and Worthington numbers were compared to the threshold values. As explained in the previous section, the Bond number must be higher than 0.3 whereas Worthington number depends on the needle size. In fact, a Worthington number higher than 0.6 was accepted for all needle sizes however and for relatively bigger size needles (≈ 0.51 mm in diameter) a value

higher than 0.4 was accepted. Any value lower than 0.4 was ignored and the experiment was considered unsuccessful [8].

Table A.1: Pendant drop tensiometry experiments for different oil-lipid combinations. Below are all the values used leading to the average and standard deviation presented in Figure A.1. These experiments comply with the requirements of a stable droplet while maintaining the recommended Worthington and Bond numbers depending on the needle size used. Monolayer surface tensions shown are in mN/m.

| **Oil** | **Hexadecane** | | | |
|---|---|---|---|---|
| **Cholesterol mole fraction** | **0** | **0.1** | **0.2** | **0.3** |
| Trial 1 | 1.154 | 1.192 | 1.307 | 1.379 |
| Trial 2 | 1.196 | 1.208 | 1.245 | 1.478 |
| Trial 3 | 1.177 | 1.063 | 1.352 | 1.408 |
| Trial 4 | 1.063 | 1.120 | 1.264 | 1.376 |
| Trial 5 | 1.145 | 1.266 | 1.361 | 1.474 |
| Trial 6 | 1.134 | | 1.270 | 1.456 |
| Trial 7 | 1.198 | | 1.294 | 1.400 |
| Trial 8 | 1.098 | | | 1.473 |
| Trial 9 | 1.091 | | | 1.515 |
| Trial 10 | 1.130 | | | 1.396 |
| Trial 11 | | | | 1.333 |
| **Average** | **1.139** | **1.170** | **1.299** | **1.426** |
| **STDEV** | **0.043** | **0.071** | **0.041** | **0.053** |

## Membrane specific capacitance measurements

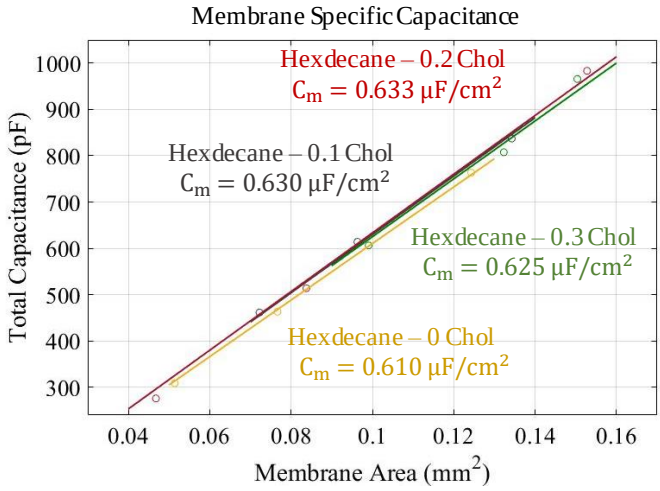


Figure A.2: One example from each cholesterol composition showing the linear fit of the total capacitance with respect to the membrane area. The slope indicates the membrane's specific capacitance.

Table A.2: The values of the specific capacitance used to obtain the average and standard deviation presented in the manuscript. Units are $\mu F/cm^2$.

| **Oil** | **Hexadecane** | | | |
|---|---|---|---|---|
| **Cholesterol mole fraction** | **0** | **0.1** | **0.2** | **0.3** |
| Trial 1 | 0.628 | 0.624 | 0.633 | 0.616 |
| Trial 2 | 0.623 | 0.631 | 0.608 | 0.613 |
| Trial 3 | 0.611 | 0.631 | 0.648 | 0.634 |
| Trial 4 | 0.613 | 0.630 | 0.642 | 0.643 |
| Trial 5 | 0.622 | 0.646 | 0.618 | 0.625 |
| Trial 6 | 0.610 | | | |
| **Average** | **0.618** | **0.632** | **0.630** | **0.626** |
| **STDEV** | **0.007** | **0.007** | **0.015** | **0.011** |

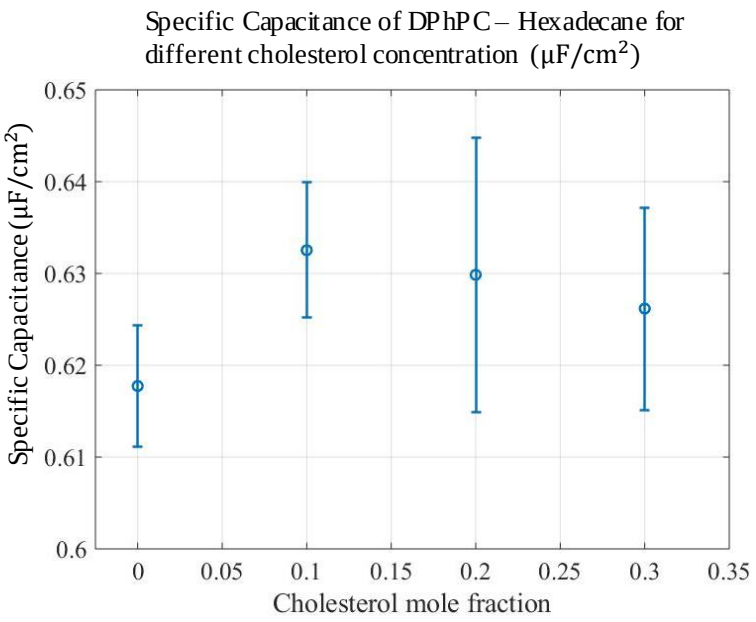


Figure A. 3: Mean and standard deviation of the membrane's specific capacitance (μF/cm$^2$) with hexadecane for different cholesterol mole fractions. These values correspond to the last two rows of Table 2.

Figure A.2 shows a few examples of the linear fit regression method used to calculate the specific capacitance for each oil-lipids combination. As discussed in the manuscript, the specific capacitance was obtained by plotting the membrane's total capacitance versus its area [2]. The latter was modified manually by pulling the micromanipulators slightly apart for a few times - 3 to 4, depending on the membrane's initial size - until the droplets are total separate. Thus, each experiment consisted of 3 to 4 data points that were fit into a straight line passing through the origin. Any linear fit that showed an $R^2$ value of less than 0.97 was ignored and the experiment was repeated. The slope unit (pF/mm$^2$) was adjusted to the conventional unit of μF/cm$^2$. Table A.2 shows all the values used to obtain the average and the standard deviations, which are plotted in Figure A. 3.

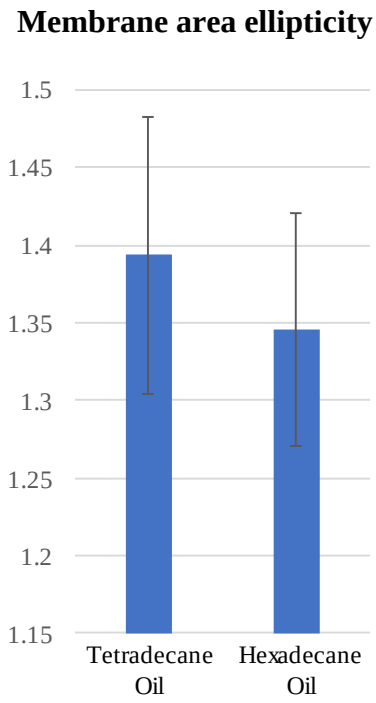


Figure A. 4: Ellipticity factor – ratio of the major radius of membrane area to the minor one – for tetradecane oil ($\rho$ = 764 kg/m$^3$) as well as for hexadecane oil ($\rho$ = 773 kg/m$^3$). The average value shown is the mean of the ellipticity factor when the droplets are at rest – no electrical field applied.

The droplets used in this study were approximately 250 nL in volume (800 µm in diameter). The difference in densities between the aqueous droplet and the oil medium as well as the reduction in surface tension enhanced by surfactants are two primary causes for the droplet distortion from a spherical shape. The ellipticity factor was calculated as the ratio of the major radius of the membrane area to the minor one. For hexadecane oil (773 kg/m$^3$), the ellipticity factor is 1.35 (± 0.075), whereas tetradecane (764 kg/m$^3$) showed a slightly higher value of 1.39 (± 0.089). Since tetradecane shows a higher difference in density with respect to the aqueous solution (≈ 1040 kg/m$^3$) more pendant effect is expected as the gravitational effect is more influential.

## Contact angle measurements

Contact angle measurements used in this study were obtained using geometric manipulations of the droplets bottom images. In fact, findcircles() algorithm in MATLAB was used to find the circular circumferences of the droplets as viewed from below and the corresponding tangents determined the DIB's contact angle. Unfortunately, the same cannot be done from the side view images as it is not as accurate nor as straight-forward. Droplets' pendant shape, insufficient image resolution and changeable electrodes wetting behavior are all reasons prohibiting accurate contact angle measurements form the side images. However, given the principle of emulsion equilibrium, and given constant monolayer and bilayer surface tensions, the contact angle is expected to remain constant all over the monolayer/bilayer annulus, leading to sufficient bottom view measurements.

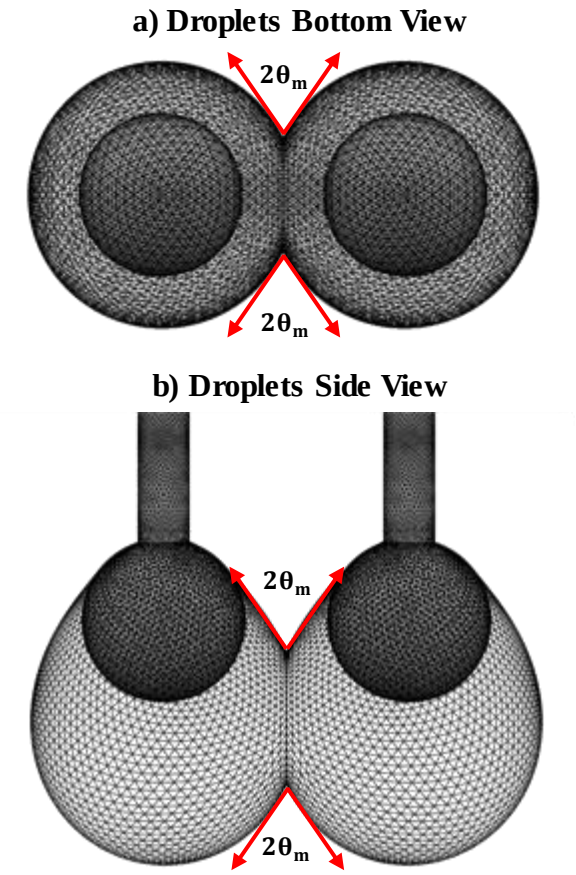


Figure A. 5: Surface Evolver bottom and side view images of a DIB at steady state. Values for the monolayer and bilayer surface tensions as well as for the specific density were obtained assuming hexadecane oil and only DPhPC lipids – no cholesterol. Comparing the bottom and side view, one can see how the contact angle at the annulus is consistent all over the ring. The angle between the two red arrows is the same as measured geometrically.

To further support our argument, surface evolver was used to generate the predicted steady state dimensions for the DPhPC and Hexadecane case – no cholesterol. As seen in Figure A. 5, the upper and lower contact angles from the side and bottom views are exactly the same. The angle between the two red arrows in the same measured angle. The principle of least total energy requires the droplets to be separated by the same contact angle all over the elliptical circumference of the symmetric bilayer.

## Lipids-in-oil monolayer surface tension measurements

In the early stages of the study, tensiometry measurements were conducted with lipids dispersed in the oil phase rather than in the aqueous solution. These results are not included in the study, but it is of interest to show the dissimilar way cholesterol affects the monolayer surface tension depending on the phase it is dispersed in.

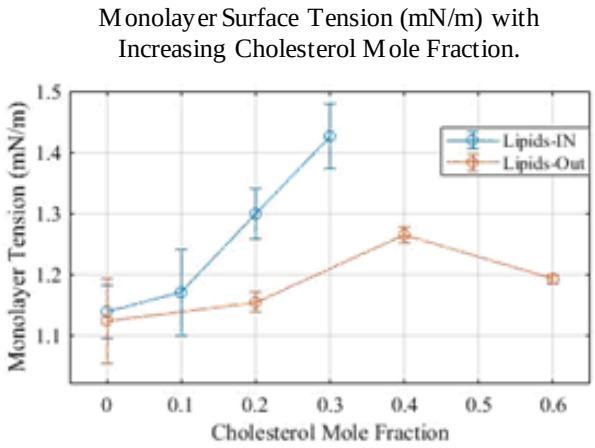


Figure A. 6: Monolayer surface tension (mN/m) with varying cholesterol mole fraction. In both cases, cholesterol is mixed with DPhPC phospholipids. In the lipids-in scenario, hexadecane oil was used. Whereas in the lipids-out scenario a 1:1 mixture of hexadecane and silicone oil was used.

Figure A. 6 shows the monolayer surface tension with varying cholesterol mole fractions with respect to DPhPC. In this case, the value is compared between lipids-in scenario – lipids are dispersed in the aqueous phase – and lipids-out scenario – lipids are dispersed in the oil phase. Note that the oil phase is not the same in these two cases (hexadecane for lipids-in; 1:1 Hexadecane:AR20 for lipids-out), but we are more interested in comparing the intensity of the effect of cholesterol addition. As observed in this figure, cholesterol's effect on the surface tension is much more significant when lipids are dispersed in the aqueous phase. In fact, going from 0% to 20% cholesterol increases the tension by 2.6% when dispersed in the oil phase compared to 14.1% in the aqueous phase.

This behavior can be explained by cholesterol's favorability to dissolve in oil as its hydrophobic part is substantial enough to favor forming reverse micelles in oil rather than liposomes as it would in the aqueous phase. Thus, the mole fractions mixed and dispersed in the oil might not mirror the same fraction at the monolayer surface. This explains the smaller increase in surface tension as cholesterol is not integrating itself at the monolayer as it would in the lipids-in case.

## References


1. Venkatesan, G.A., et al., *Adsorption Kinetics Dictate Monolayer Self-Assembly for Both Lipid-In and Lipid-Out Approaches to Droplet Interface Bilayer Formation.* Langmuir, 2015. **31**(47): p. 12883-93.
2. Taylor, G.J., et al., *Direct in situ measurement of specific capacitance, monolayer tension, and bilayer tension in a droplet interface bilayer.* Soft Matter, 2015.
3. Huang, J., J.T. Buboltz, and G.W. Feigenson, *Maximum solubility of cholesterol in phosphatidylcholine and phosphatidylethanolamine bilayers.* Biochimica et Biophysica Acta (BBA)-Biomembranes, 1999. **1417**(1): p. 89-100.
4. Hung, W.-C., et al., *The condensing effect of cholesterol in lipid bilayers.* Biophysical journal, 2007. **92**(11): p. 3960-3967.
5. Parker, A., et al., *Lateral distribution of cholesterol in dioleoylphosphatidylcholine lipid bilayers: cholesterol-phospholipid interactions at high cholesterol limit.* Biophysical journal, 2004. **86**(3): p. 1532-1544.
6. Gross, L.C., et al., *Determining membrane capacitance by dynamic control of droplet interface bilayer area.* Langmuir, 2011. **27**(23): p. 14335-14342.
7. Tarun, O.B., M.Y. Eremchev, and S. Roke, *Interaction of Oil and Lipids in Freestanding Lipid Bilayer Membranes Studied with Label-Free High-Throughput Wide-Field Second-Harmonic Microscopy.* Langmuir, 2018. **34**(38): p. 11305-11310.
8. Berry, J.D., et al., *Measurement of surface and interfacial tension using pendant drop tensiometry.* Journal of Colloid and Interface Science, 2015.
9. Lin, S.-Y., et al., *An examination on the accuracy of interfacial tension measurement from pendant drop profiles.* Langmuir, 1995. **11**(10): p. 4159-4166.

# APPENDIX B

# STUDYING THE MECHANICS OF MEMBRANE PERMEABILIZATION THROUGH MECHANOELECTRICITY

## SUPPLEMENTARY INFORMATION [3]

[3] El-Beyrouthy, J., Makhoul-Mansour, M. M., & Freeman, E. C. (2022). Studying the Mechanics of Membrane Permeabilization through Mechanoelectricity. *ACS Applied Materials & Interfaces*.


.

## Lipids and agents' solutions preparation

Phospholipids were dispersed in the aqueous phase as the lipids-in-water approach allows for the convenient and repeatable formation of asymmetric membranes [1, 2]. A buffer solution was prepared by dissolving 250 mM of potassium chloride (KCl, ≥99.1%—Sigma-Aldrich) with 10 mM of 3-(N-Morpholino) propane sulfonic acid (MOPS, ≥ 99.5%—Sigma-Aldrich) in DI water. Then, the desired lipids, detergents or peptide were dispersed in this buffer solution at their desired concentrations.

3 different lipid solutions were regularly prepared and refreshed as needed. (1) Zwitterionic ester DPhPC (1,2-diphytanoyl-sn-glycero-3-phosphocholine) was purchased in its powder form from Avanti Polar Lipids. DPhPC powder was directly mixed with the buffer solution leading to micelle formation in the aqueous environment. This solution was recognized as the reference or control case as these lipids form electrically neutral monolayers. (2) Anionic ester DPhPG (1,2-diphytanoyl-sn-glycero-3-phospho-(1'-rac-glycerol) (sodium salt)) was purchased from Avanti Polar Lipids and dispersed with DPhPC at a 1:4 DPhPG:DPhPC mass ratio [3, 4]. Initially in powder form, DPhPG was dissolved in chloroform at a concentration of 10 mg/mL. Similar chloroform solutions were formed with DPhPC, then appropriate volumes of each solution were mixed in a new vial according to the desired mass ratio. Dissolving phospholipids in chloroform allows for a homogeneous mixture of lipids in the micelles. Chloroform was then evaporated in a two-step process: via argon gas flow, then via placement in a vacuum chamber for several hours. The dry lipids film was then hydrated with the buffer solution forming the anionic lipid solution. (3) Zwitterionic ether DOPhPC (1,2-di-O-phytanyl-sn-glycero-3-phosphocholine) was purchased dissolved in chloroform and the needed volume was

extracted and evaporated as described earlier. All lipid mixtures had a final concentration of 2 mg/mL.

After dispersal of the lipids in the buffer solutions, at least 4 freeze-thaw cycles were performed. Freezing was ensured by placing the vials in a -20℃ freezer and thawing was performed at room temperature ~ 21℃. The day of the experiment, a partial volume is extracted from the bulk solution, then extruded and sonicated ensuring proper and homogeneous dispersion of the lipids. Extrusion is based on passing the solution across 0.1μm pores back and forth for at least 10 cycles, breaking the large lipid micelles using the block extrusion element (Avanti Polar Lipids) and gas-tight syringes (Hamilton), whereas sonication was done using the probe tip sonicator (Q55 QSONICA, LLC) further breaking down the micelles. Sonication was performed via 2 minute on-off cycles to avoid overheating the solution, until the solution is rendered clear and transparent.

CTAB (Hexadecyltrimethylammonium bromide, ≥98%, Sigma-Aldrich) and SDS (Sodium Dodecyl Sulfate, > 99.9%, Research Products International) were purchased in their powder form and mixed with the same buffer solution as the lipids to avoid salt concentration imbalance during experiments. Detergent concentrations were calculated to reach an in-droplet concentration comparable to previously published work [5]. Detergent solutions were stored at room temperature. Melittin from honeybee venom (≥85% HPLC) was ordered from Sigma-Aldrich as a powder. Dissolved in methanol at a concentration of 10 mg/mL, the desired volumes were extracted and mixed with the buffer solution to form the bulk melittin solution concentrations. Fresh melittin solution was prepared every day for maintaining the activity of the peptide. Finally, the solvent used in this work was hexadecane oil (Sigma-Aldrich). Hexadecane was chosen for its ability to form long-

lasting, stable, and relatively solvent-free membranes compared to other alkanes [6-8]. Having a solvent-free membrane increases the model membrane physiological relevance and leads to low membrane elasticity validating the assumption of constant membrane thickness.

**Suspended DIBs and the minimum capacitance technique**

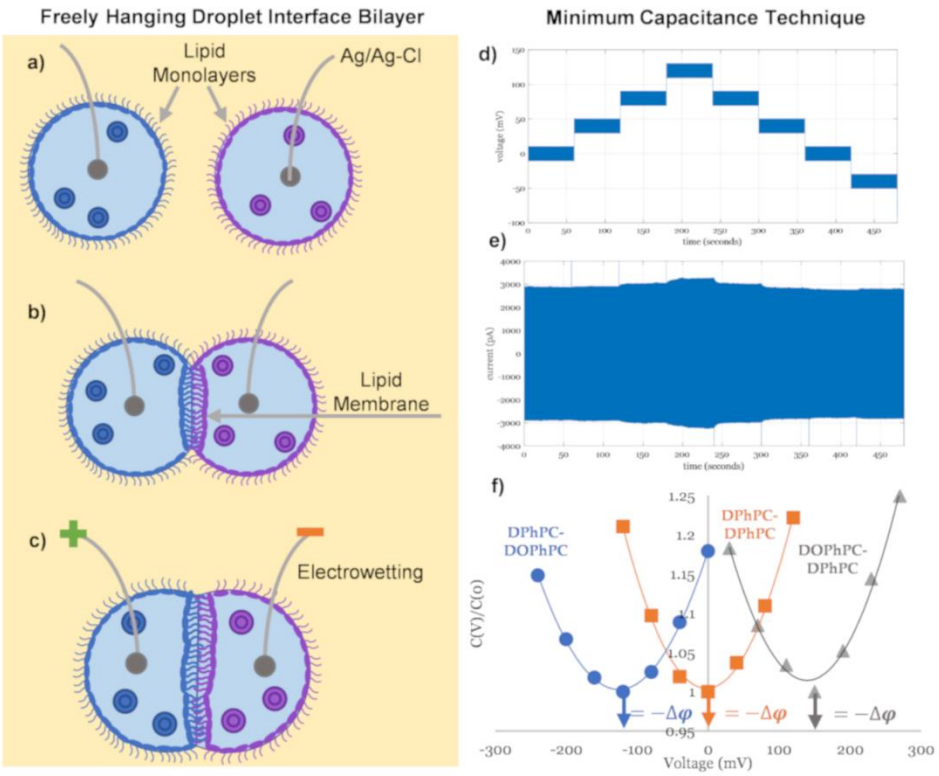


Figure B. 1: Suspended DIBs were used in this work to measure the potential offset using the traditional minimum capacitance technique. a) DIBs are formed by first having the droplets suspended from silver/silver-chloride electrodes in an oil medium, where monolayer formation occurs. b) Approaching the two lipid-coated droplets together, the membrane forms at their adhered interface. c) Under an applied electrical field, DIB responds according to the electrowetting effect where membrane tension reduction is visualized as an increase in the membrane area, and thus membrane capacitance. d) The minimum capacitance technique relies on varying the electric field across the double layer and waiting for the new membrane equilibrium. e) Membrane-generated current under the new equilibrium is used to calculated membrane capacitance. f) Plotting membrane capacitance at equilibrium versus the applied voltage, the membrane potential offset can be calculated as the one that provides the least capacitance. Examples here are given for

symmetric DPhPC and asymmetric DPhPC-DOPhPC membranes. Flipping the monolayers with respect to the electrical input provides an opposite offset.

Suspended DIBs were used to validate our mechanoelectricity approach by measuring fixed membrane asymmetric potential offsets. As illustrated in Figure B. 1, suspended DIBs are formed by first submerging silver/silver-chloride (Ag/Ag-Cl) electrodes into a hexadecane reservoir (1 cm x 1 cm base, 1 mm thick walls acrylic glass cube). These electrodes allow for electrophysiological characterization of the resulting membrane and are tipped in 2.5% agarose solution to aid in droplet adhesion (low EEO, Sigma-Aldrich). Droplets of the desired lipid solutions are deposited directly on the electrode tips by means of a micropipette controlled through a microinjector attached to a micro manipulator. In the case of symmetric membranes, the same solution was used to form both droplets. However, when asymmetric membranes were desired, different lipid solutions were deposited on either electrode. Once the aqueous droplets are placed in the hydrophobic bath, the dispersed phospholipids align at the water-oil interface driven by their self-assembly property forming the monolayer, as shown in Figure B. 1 (a). Once the monolayer is stabilized, placing the two water droplets in contact the membrane favorably forms at their adhered interface, Figure B. 1 (b). A few minutes are provided for the membrane to reach its equilibrium dimension as measured by a steady current amplitude through an alternating voltage signal.

As seen in Figure B. 1 (c), the application of an electric field across the membrane leads to an increase in membrane area and thus, membrane capacitance. This technique is based on the equilibrium capacitance of the membrane under a steady electric field, producing a minimum dimension where the internal field is compensated. Figure B. 1(d) and (e) show an example of varying the DC voltage and the recorded membrane-generated

current to calculate membrane equilibrium capacitance. Figure B. 1 (f) shows the plot of capacitance with respect to the applied voltage. This parabola is theoretically centered at 0 mV for symmetric membranes, however asymmetric membranes shift the center to the DC voltage that compensates for its asymmetric potential, i.e., $\Delta\varphi = -V_{DC}$. The latter opposites in sign and equals in magnitude to the voltage leading to the minimum membrane capacitance. What has been discussed can be described by the following equations:

$$\|C_V\| = \|I\|/\|dV/dt\| \qquad (B.1)$$

$$C(V) = C_0(1 + \alpha(V_{DC} + \Delta\varphi)^2) \qquad (B.2)$$

Using an automated MATLAB code, Equation B. 1 calculates membrane equilibrium capacitance at each voltage and Equation B. 2 calculates the potential offset by fitting the obtained data points to the equation.

Electrophysiology measurements are enabled in our lab using the membrane Axopatch 200B patch-clamp amplifier and a Digidata 1440 data acquisition system (Molecular Devices). The minimum capacitance technique was performed by applying a sinusoidal voltage of 40 Hz frequency and 10 mV amplitude. Each 60 seconds, this AC signal is combined with DC voltage steps of ± 40 mV with a maximum voltage range of ±160 mV. When a relatively high membrane potential offset is expected, like the case of DPhPC/DOPhPC, the voltage steps are not centered at zero, but at a higher voltage to be able to catch the minimum capacitance value. In the examples provided in Figure B. 1 (f), the voltage was centered at -120 mV for the case of DOPhPC on the ground electrode – blue line – and 150 mV for the case of DOPhPC on the electrical input – grey line. Centering the voltage steps around an approximate value (120 mV and 150 mV instead of 0 mV) avoids over compressing the membrane which might lead to membrane failure.

Changing the center for various cases ensures that centering the voltage steps around a certain value does not affect the results. Equilibrium time depends on the solvent used, and for hexadecane, 60 seconds allow for steady state capacitance, as seen in Figure B. 1 (e).

**Surface charge calculations**

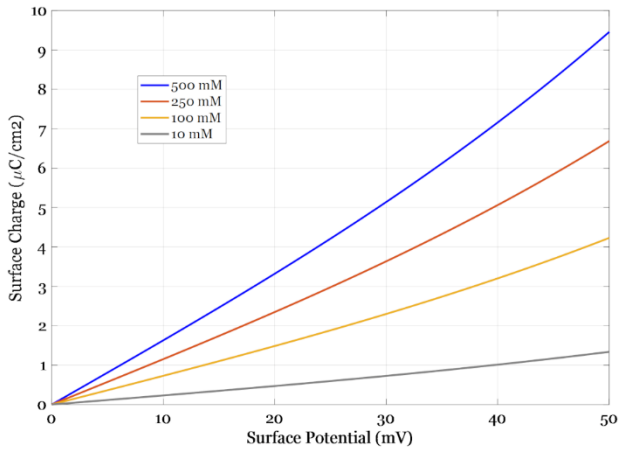


Figure B. 2: Surface charge and surface potential relationship according to Grahame equation [9] for various salt concentrations. This equation was used in our work to calculate the change in membrane surface charge from the applied potential. For the range of our values, this relationship is almost linear.

The change in membrane surface charge was calculated based on membrane potential and salt concentration according to the Grahame equation [9], which relies on the Gouy-Chapman-stern theory to correlate between surface charge and surface potential, as follows:

$$\sigma = \sqrt{8C_0\varepsilon\varepsilon_0 K_B N_A T}\ sinh(\frac{ze\Delta\varphi}{2K_B T}) \qquad \text{(B. 3).}$$

Figure B. 2 shows the charge-potential relationship for various monovalent salt concentrations focusing on the range of our experiments. The use of Grahame equation for DIBs was validated through the case of asymmetric anionic membranes. In the case of one-

sided negatively charged membrane DPhPC/1:4 DPhPG:DPhPC, the experimentally measured and the calculated surface charge were compared. First, the average of membrane potential offset for DPhPG asymmetric membranes, was considered: $\varphi_{s,DPhPG} = -29.2$ mV. According to Equation B. 3 and considering the monovalent salt concentration of $C_0$=250 mM, the surface charge of 1:4 DPhPG:DPhPC monolayer is $\sigma_{s,DPhPG} = -3.57\ \mu C/cm^2$. Then, estimating this surface charge was calculated by considering an equal area per lipid of 81.2 $A^2$ for both phospholipids [10], and assuming a perfect 1:4 lipids distribution, the monolayer surface charge is calculated as: $\sigma_{s,DPhPG} = -3.95\ \mu C/cm^2$. This supports the use of the Grahame equation for our system; however the electrostatics model may not perfectly align with experimental conditions and the values produced should be treated as estimates.

## Mechanoelectricity setup and characterization

### Experimental setup

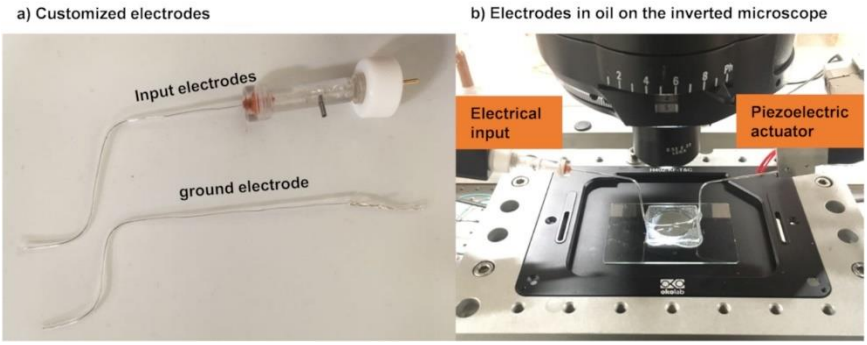


Figure B. 3: Experimental setup used for the generation of mechanoelectricity. a) Two S-shaped glass pipettes contain silver/silver-chloride electrodes are used for the support of the droplets, for providing the mechanical displacement, as well as for electrophysiology measurements. These wires are fixed in the pipettes through solidified hydrogels. b) The input electrode is connected to the headstage for electrical signaling. The ground electrode is connected back to the piezoelectric actuator providing the displacement. Both electrodes are placed parallelly in the oil dish on the inverted microscope.

Figure B. 3 shows the customized electrodes adopted for the generation of the mechanoelectric current. Two S-shaped customized glass pipette electrodes are first prepared to hold the hemispherical droplets allowing for electrical measurements. First, 125µm thick silver wires are submerged in a sodium hypochlorite solution forming the silver/silver-chloride electrodes for electrical measurements. These electrodes are then inserted into a hallow 1mm wide cylinder glass pipettes, which have been bent twice at 90$^{o}$ angles making an S-shape, to ensure the parallel adjustments of the droplets with respect to each other and to the piezoelectric actuator. The electrodes are fixed into the glass pipettes by filling the hallow cylinder with hydrogels. In fact, our experiments showed that it is best to use UV curable Peg-DMA hydrogel (0.4 w:v of Poly(ethylene glycol) 1000 dimethacrylate, Polysciences, Inc, with 0.025 w:v of curable agent (2-Hydroxy-2-methylpropiophenon, TGI)) for most of the pipette except for its tip where the droplets are placed, which was filled with agarose gel (0.013 w:v Low melting point agarose, Benchmark scientific). After solidifying the hydrogels, the pipettes are submerged into a 2.5 cm wide, and 0.3 cm deep circular oil dish, while ensuring their parallel alignment. One of the pipettes is connected to the headstage of the Axoaptch amplifier indicating the electrical input and the structurally fixed side. The facing pipette is mobile as it is connected to the piezoelectric actuator, and it corresponds to the electrical ground.

**Mechanoelectricity with displacement amplitude**

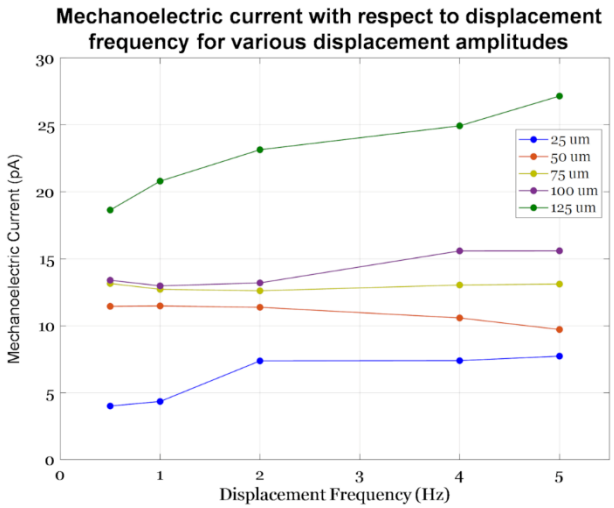


Figure B. 4: Amplitude of the mechanoelectric current with respect to the displacement frequency for various displacement amplitudes. The displacement amplitudes shown herein correspond to half the total distance traveled by the droplet. This experiment was conducted for a symmetric DPhPC membrane in hexadecane.

Figure B. 4 shows the calculated mechanoelectric current with respect to displacement frequency for various amplitudes. This experiment was done on a symmetric and electrically neutral DPhPC membrane formed in hexadecane oil. A constant $V_{DC}$=50 mV was applied during the entire experiment to generate the mechanoelectric current. Since the membrane is symmetric, there will be no mechanoelectric current without an external electric field. Observing the trend of the plot shows that the displacement amplitude has a bigger effect on the current compared to the frequency. Generally, a higher displacement leads to a higher current for the same frequency. As for the change in frequency, for $D_p$ = 25,100 and 125 µm, a higher frequency led to a higher current amplitude, but for $D_p$ = 50 and 75 µm, the increase in displacement frequency led to an irregular and slight reduction in the generated current. It can be concluded that the displacement amplitude has the strongest effect on the mechanoelectricity amplitude. A

large mechanoelectric current is desired in our studies as it will provide a better detection and control from the PID. However, care must be taken when increasing the displacement amplitude as if pushed too close together, the change in the droplet area may be too great, which leads to droplets collapsing and membrane failing. Thus, an optimized value of 75µm was adopted. In this case, the droplet travels a total distance of $D_{PP} = 150\mu m$ leading to a significant current amplitude without risking membrane failure.

**Mechanoelectricity with displacement frequency**

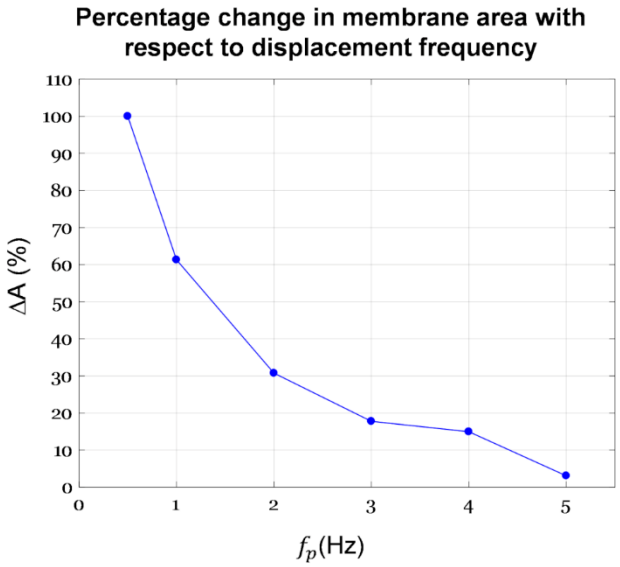


Figure B. 5: Effect of the displacement frequency on the change in membrane area. For the same membrane and same displacement frequency, the percentage change in membrane area is calculated with respect to $f_p$=0.5 Hz as the frequency of reference. As the displacement frequency increases, a reduction in the change in membrane area is observed. This is explained by the viscoelastic forces present due to the surrounding oil.

The effect of the displacement frequency on the droplet's behavior and thus the membrane response was analyzed and displayed in Figure B. 5.A symmetric DPhPC membrane in hexadecane oil was formed using the adjusted DIB setup. The displacement amplitude adopted in these measurements was $D_{PP}$ =250 µm. Note that this is not the value adopted in the main experiments of this research, but it is utilized here to generate the

maximum exaggeration of the current amplitude as well as the highest resolution to be able to differentiate between mechanical and electrical current. Simultaneously to the harmonic displacement performed on the ground droplet, a sinusoidal voltage is applied of the form: $V(t) = 50\ mV + 5\ mV\ sin(2\pi * 50Hz * t)$. The constant $V_{DC}$=50 mV was applied to ensure the presence of a mechanoelectric current across this symmetric membrane, whereas the sinusoidal voltage was used to calculate membrane capacitance, and thus membrane area. For these fixed parameters, the displacement frequency was the only variable, we have considered values from $f_p$ = 0.5 to 5 Hz.

For each oscillation frequency, two membrane capacitances were calculated: $C_{min}$ corresponds to the minimum membrane capacitance when the droplets are the furthest apart, and $C_{max}$ corresponds to the maximum membrane capacitance that happens when the droplets are the closest together. These values were then used to calculate the change in membrane area taking into consideration the fixed specific capacitance of a DPhPC membrane in hexadecane, $C_s$ = 0.63μF/cm$^2$ [8], and the parallel plate capacitor equation: $\Delta A = (C_{max} - C_{min})/C_s$. Additionally, and for the sake of better data analysis, the change in area at $f_p$ = 0.5 Hz was set as the maximum possible change so it was given a 100% value and the rest was compared to this reference point. As observed in Figure B. 5, the change in membrane area reduces significantly as the displacement frequency increases, until it reaches a minimal value of 3% at $f_p$ = 5Hz. These results agree with previously published work [11] and they can be explained by the presence of the surrounding oil reservoir. Each time the droplet is displaced, the surrounding oil acts as a viscous obstacle that the membrane must overcome to form new surface area. This force that resists additional membrane formation leads to this decrease in change in area with the frequency. The faster

the droplet is moving, the less time the membrane has to expel the solvent. An optimum frequency of $f_p$ = 3 Hz was adopted in all the main experiments of this technique as the frequency that is far enough from 0 Hz allowing for proper sampling and data analysis through a distinct mechanoelectric peak in the FFT, while limiting complications from higher frequency oscillations.

## Control algorithm

A proportional-integrative-derivative (PID) controller was used to attenuate the mechanoelectric current through LabVIEW. First, input parameters had to be defined depending on the frequency adopted, including the sampling frequency, $f_n$, and the sampling number, $N$. The ratio of these two variables dictates the frequency window of data acquisition. In our experiments, a value of $f_n$ = 2000 Hz and $N$ = 2000 samples lead to $dt$ = 1 second. Additionally, the user has to provide the signal frequency, the set value for the PID – set to zero – and the PID gains and output range. PID gains were tuned according to the trial-and-error method. An initially symmetric membrane was formed, and a 50 mV DC voltage was applied to simulate the mechanoelectric current. Varying the PID gains and observing the system response, coefficients were optimized as follows: $K_p$ = 10; $T_i$ = 0.002; and $T_d$ = 0.001. Note that the model membrane system is fluidic and the membrane size, response to compression, and electrical properties are anticipated to slightly vary between experiments leading to differences in the system response under the same PID coefficients.

Two adjustments were made to the input signal. First, the current-voltage relationship was linearized to assist with PID performance. This was accomplished using the phase angle difference between the displacement and mechanoelectricity. Using FFT,

the phase angles of displacement and current were obtained. Based on control cases, it was observed that when $\|\Delta\theta\| > \pi/2$, the voltage has a negative relationship with the current, and when $\|\Delta\theta\| < \pi/2$, this relationship is positive. This permitted linearizing the voltage-current relationship through a condition statement. Second, the mechanoelectricity amplitude considers the first two harmonics while eliminating surrounding noise. It is not sufficient to consider the first harmonic solely as a significant peak at $2f_p$ was observed. Furthermore, to remove surrounding noise a one cell averaging constant false alarm rate (CFAR) algorithm was applied, leading to the following equation used to calculate mechanoelectricity amplitude separate from the noise floor: $I_{mech} = A_{f_p} + A_{f_{2p}} - A_{f_{(p-1)}} - A_{f_{(p+1)}} - A_{f_{(2p-1)}} - A_{f_{(2p+1)}}$.

**Fixed membrane potential offset measurement**

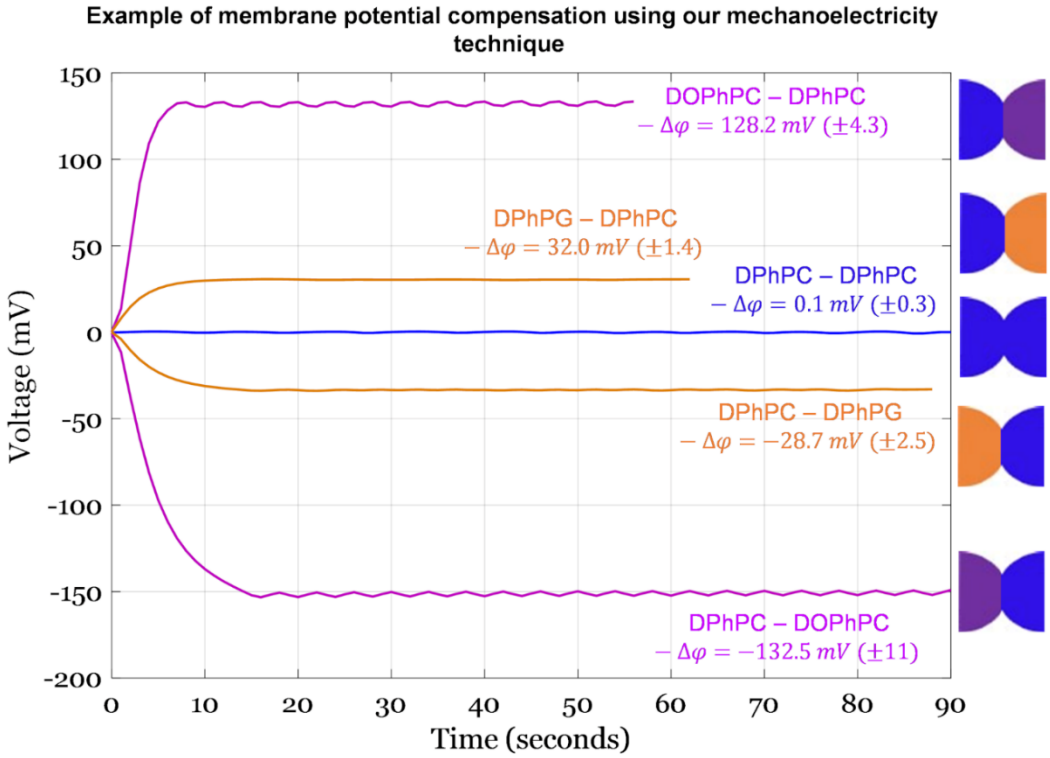


Figure B. 6: Compensating voltage with respect to time for symmetric and asymmetric membranes, presenting a fixed potential offset. Blue droplets indicate those where DPhPC phospholipids are dispersed; orange droplets indicate those where 1:4 DPhPG:DPhPC lipids mixture is dispersed; and purple droplets indicate those with DOPhPC. One example of each membrane is shown herein to illustrate the control system's ability to measure the potential offset rapidly and accurately.

Figure B. 6 shows the controller's provided voltage with time for various symmetric and asymmetric membranes. These membranes were chosen as they present a fixed and steady potential offset which was later compared to the ones obtained from the minimum capacitance technique. Blue, orange and purple droplets indicate DPhPC, 1:4 DPhPG:DPhPC and DOPhPC, respectively. In these experiments, $t$ = 0 seconds corresponds to the moment the control algorithm was initiated. The control system successfully kept the potential offset for symmetric membrane close to 0 mV and reached the potential offset for the other cases within a few seconds and remained constant. Even

though the same PID gains were used for all the experiments, a difference in the rise and settling time is observed. This can be explained by the fact that these membranes are of a fluidic nature, slight changes in droplets size, membrane capacitance or membrane innate conductivity affects the system's response to the same controller.

**Resolving lipid flip-flop in static membranes**

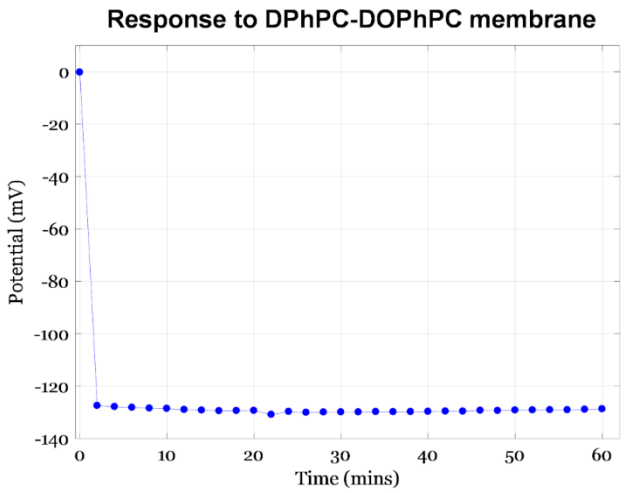


Figure B. 7: Potential offset as measured by mechanoelectricity for a DPhPC/DOPhPC membrane with respect to time over one hour observation. The membrane potential offset was tracked for over 60 minutes to detect if the continuous droplet movement and membrane disruption leads to any flip-flop events or lipids mixing or otherwise. Results show that even after 60 minutes, the membrane asymmetry remains constant.

Mechanoelectricity fundamentally relies on the constant harmonic movement of one of the droplets forming the model membrane leading to a constant disturbance of the membrane and a continuous cycle of formation/separation of the membrane leaflets. Thus, it is critical to check if this continuous membrane disruption leads to any undesired lipids mixing or lipid flip-flop events as this technique main goal herein is to measure membrane asymmetry. Results in the literature indicate that in the absence of pores these asymmetric membranes exhibit minimal flip-flop [12]; however this must also be confirmed for cases with cyclical compression. For that, a DOPhPC-DPhPC membrane of an average

asymmetric potential of $\Delta\varphi$ = -128.2 mV (±4.3 mV), was formed and the system response was observed. As seen in Figure B. 7, the membrane potential was tracked continuously for one hour and remained at a near constant value. This ensures that the detected changes in membrane asymmetry correspond to surface activity and not random lipid flip-flop events when working with asymmetric membranes.

**Membrane-agent dynamic studies**

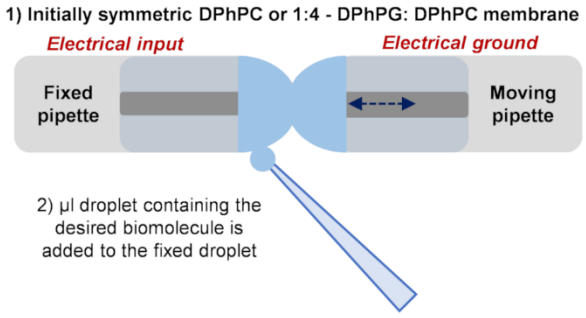


Figure B. 8: The experimental approach for the study of membrane-solubilizing detergents used to validate the transient response of our novel design is shown herein. An initially symmetric membrane is formed – electrically neutral or negatively charged – and the actuation of the piezoelectric enables the detection of a mechanoelectric current when a membrane asymmetry is present. Once the piezoelectric and the control algorithm are initiated and the system is stabilized, a nanoliters agent-full droplet is added to the fixed/electrical input droplet. This injection corresponds to $t$ = 0 seconds and the membrane surface charge is tracked afterwards. The agent's concentration is calculated as the one inside the fixed droplet, taking into consideration the droplet initial volume, the volume added, and the solution's initial concentration.

The last set of experiments performed in this work test its ability to detect transient membrane activity. Initially, a symmetric membrane built from identical monolayers was formed using the adjusted DIB setup described in Section B.2. Two membranes were adopted in these experiments, electrically neutral DPhPC membranes and negatively charged DPhPG membranes. The latter has a mass ratio of 1:4 DPhPG:DPhPC as this is the ideal ratio for replicating the negative surface charge of exoplasmic bacterial leaflets

[3, 4] while maintaining a stable lipids mixture. Once the membrane is stabilized, the displacement is provided and the amplitude of the mechanoelectric current is observed. Since the membranes are initially symmetric, there is no initial current, $I_{mech}$ ~ 0 pA, and the voltage applied by the control system stays close to 0 mV. A nanoliter droplet of the desired nanoparticle is suspended from the tip of the glass pipette and remains stable. At *t* = 0 seconds, this nanoliters droplet is added to the electrical input droplet and promptly removed, while making sure to not disturb the established membrane. The system response is then recorded, and the surface charge is calculated according to Grahame equation, as explained in Section B.3. The agents in-droplet concentrations are calculated, taking into consideration the volumes of the membrane-forming droplet and the added droplet. For each membrane, agent-free buffer solution was added as a control case, as shown in Figure 4. 8 (a).

**Diffusion in the droplet observed through calcine**

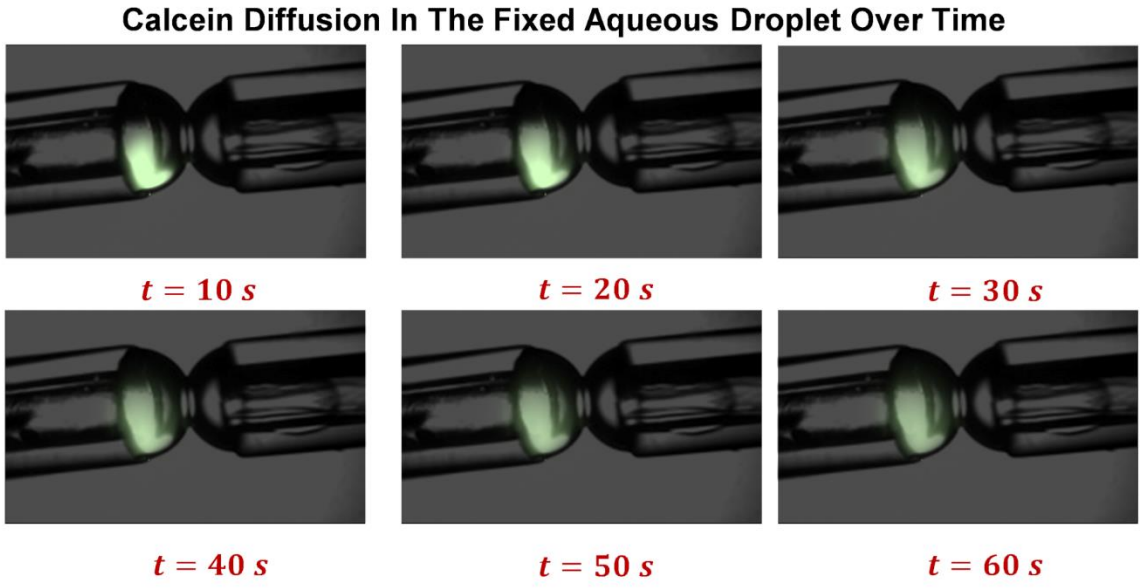


Figure B. 9: Diffusion of calcein within the fixed membrane-forming droplet. Green shows the diffusion of these particles in the aqueous droplet reflected by light microscopy. A

droplet containing 0.2 mg/mL of calcein was added to the input droplet mimicking the membrane-active agents and the experimental approach described in Section SI.7.

Calcein diffusion image analysis was performed using the mechanoelectricity setup to demonstrate the propagation and diffusion of the disruptive solution in the droplet upon injection. First, a symmetric DPhPC membrane was formed. Once membrane stabilization was ensured, displacement was initiated and at $t$ = 0 seconds, and a microliter droplet with $C$=0.2mg/mL of calcein was added into the input fixed droplet, exactly as described for the membrane permeabilizing agents experiments in section B.7. The motion of the droplets generates convective flows which accelerates mixing. Figure B. 9 shows the diffusion of calcein indicated by the green shadow within the droplet over time. Images ensure the dissipation of the nanoparticles in the fixed droplets within a few seconds. Please note that in the membrane-permeabilizing agents analysis, the time needed to initiate membrane permeabilization was measured but not mentioned as it was not a main outcome. Focus was placed on the change in membrane surface charge right before membrane permeabilization, regardless of the time it took to initiate this membrane destruction.

**Full detergent results**

This section shows the detailed results of mechanoelectricity studies with membrane-solubilizing detergents. Every trial is shown herein even those that did not lead to membrane solubilization. These are shown in italic and were not considered in the calculations of the averages. Note that for the case of 1:4 DPhPG:DPhPC membranes and anionic SDS detergent, only two cases were conducted, both with concentrations well above those expected to initiate membrane permeabilization. However, due to the expected

electrostatic repulsion, no significant interaction between the membrane and the detergent was observed for over 10 minutes, and thus no further trials were performed.

Table B.1: Critical surface charge for electrically neural and anionic membranes permeabilized by cationic CTAB and anionic SDS detergents. All experiments are shown herein. Cases where membrane permeabilization was not initiated within 10 minutes of observations are shown in italic and were not considered in the calculations of the average surface charge.

| DPhPC Membrane | | | 20% DPhPG Membrane | | |
|---|---|---|---|---|---|
| Permeabilization? | $C_{CTAB}(mg/mL)$ | $\sigma_{cr}(\mu C/cm^2)$ | Permeabilization? | $C_{CTAB}(mg/mL)$ | $\sigma_{cr}(\mu C/cm^2)$ |
| YES | 0.02 | 4.7 | YES | 0.02 | 2 |
| YES | 0.1 | 5.6 | YES | 0.06 | 3.4 |
| YES | 0.18 | 2.2 | YES | 0.13 | 5.3 |
| YES | 0.2 | 4.3 | *NO* | *0.001* | *0.6* |
| YES | 0.23 | 5 | *NO* | *0.007* | *0.5* |
| *NO* | *0.01* | *1.9* | | | |
| | **Average** | **4.4** | | **Average** | **3.6** |
| | **STDEV** | **1.2** | | **STDEV** | **1.4** |
| | **N** | **5** | | **N** | **3** |
| DPhPC Membrane | | | 20% DPhPG Membrane | | |
| Permeabilization? | $C_{SDS}(mg/mL)$ | $\sigma_{cr}(\mu C/cm^2)$ | Permeabilization? | $C_{SDS}(mg/mL)$ | $\sigma_{cr}^{*}\ (\mu C/cm^2)$ |
| YES | 0.48 | -5.7 | *NO* | *0.51* | *-0.4* |
| YES | 1.33 | -2.3 | *NO* | *2.46* | *-0.2* |
| YES | 1.43 | -5.1 | | | |
| YES | 1.9 | -3.9 | | | |
| *NO* | *0.16* | *-0.6* | | | |
| | **Average** | **-4.3** | | **Average** | **NA** |
| | **STDEV** | **1.3** | | **STDEV** | **NA** |
| | **N** | **4** | | **N** | **NA** |

**Full melittin results**

The table below presents all experiments of melittin with neutral and anionic membranes. Each column represents membrane composition and was divided in two sections: the top section includes the cases were membrane permeabilization was observed, and the bottom section presents those where no permeabilization was observed within the 10 minutes of observation.

Table B.1: Results of melittin experiments with zwitterionic and anionic membranes. Results show all conducted experiments including those who did not lead to membrane permeabilization within 10 minutes.

| **DPhPC Membrane** | | | **20% DPhPC Membrane** | | |
|---|---|---|---|---|---|
| $C_{melittin}(\mu g/mL)$ | $\sigma_{cr}(\mu C/cm^2)$ | $t_{cr}(sec)$ | $C_{melittin}(\mu g/mL)$ | $\sigma_{cr}(\mu C/cm^2)$ | $t_{cr}(sec)$ |
| 57 | 2.04 | 142 | 22 | 3.03 | 39 |
| 44 | 1.81 | 119 | 23 | 2.95 | 257 |
| 42 | 1.78 | 28 | 9 | 2.26 | 129 |
| 30 | 1.49 | 184 | 45 | 2.05 | 96 |
| 41 | 1.27 | 151 | 14 | 1.99 | 88 |
| 4 | 1.05 | 187 | 31 | 1.67 | 100 |
| 81 | 1 | 102 | 57 | 1.35 | 257 |
| 13 | 0.85 | 305 | 63 | 1.15 | 117 |
| 7 | 0.8 | 232 | 9 | 1.09 | 394 |
| 12 | 0.71 | 238 | 4 | 1.07 | 186 |
| 97 | 0.71 | 47 | 98 | 0.91 | 319 |
| 15 | 0.65 | 305 | 28 | 0.89 | 62 |
| 24 | 0.63 | 261 | 74 | 0.63 | 373 |
| 26 | 0.35 | 248 | 54 | 0.58 | 52 |
| 52 | 0.23 | 325 | 30 | 0.49 | 130 |
| 31 | -0.29 | 29 | **Average** | **1.47** | **173** |
| 21 | -0.8 | 235 | **STDEV** | **0.79** | **114** |
| **Average** | **0.84** | **185** | **N** | **15** | **15** |
| **STDEV** | **0.71** | **93** | *Below cases showed no permeabilization within 10 minutes* | | |
| **N** | **17** | **17** | $C_{melittin}(\mu g/mL)$ | $\sigma^*_{cr}$ $(\mu C/cm^2)$ | $t^*_{cr}(sec)$ |
| *Below cases showed no permeabilization within 10 minutes* | | | 30 | 0.93 | 51 |
| $C_{melittin}(\mu g/mL)$ | $\sigma^*_{cr}$ $(\mu C/cm^2)$ | $t^*_{cr}(sec)$ | 35 | 0.67 | 60 |
| 12 | 1.19 | 143 | 43 | 0.8 | 147 |
| 14 | 0.58 | 170 | 14 | 1.11 | 166 |
| 11 | 0.35 | 135 | 13 | 0.94 | 71 |
| 31 | 0.44 | 363 | 22 | 0.8 | 95 |
| **Average** | **0.64** | **203** | 39 | 0.88 | 45 |
| **STDEV** | **0.33** | **93** | 53 | 1.07 | 47 |
| **N** | **4** | **4** | **Average** | **0.9** | **85** |
| | | | **STDEV** | **0.14** | **44** |
| | | | **N** | **8** | **8** |

## References


1. Makhoul-Mansour, M.M., et al., *Photopolymerized microdomains in both lipid leaflets establish diffusive transport pathways across biomimetic membranes.* Soft matter, 2019. **15**(43): p. 8718-8727.
2. Taylor, G., et al., *Electrophysiological interrogation of asymmetric droplet interface bilayers reveals surface-bound alamethicin induces lipid flip-flop.* 2019. **1861**(1): p. 335-343.
3. Wu, M., et al., *Mechanism of interaction of different classes of cationic antimicrobial peptides with planar bilayers and with the cytoplasmic membrane of Escherichia coli.* Biochemistry, 1999. **38**(22): p. 7235-7242.
4. Ashrafuzzaman, M., O. Andersen, and R.J.B.e.B.A.-B. McElhaney, *The antimicrobial peptide gramicidin S permeabilizes phospholipid bilayer membranes without forming discrete ion channels.* 2008. **1778**(12): p. 2814-2822.
5. Vaidyanathan, S., B.G. Orr, and M.M.J.T.J.o.P.C.B. Banaszak Holl, *Detergent induction of HEK 293A cell membrane permeability measured under quiescent and superfusion conditions using whole cell patch clamp.* 2014. **118**(8): p. 2112-2123.
6. Gross, L.C., et al., *Determining membrane capacitance by dynamic control of droplet interface bilayer area.* Langmuir, 2011. **27**(23): p. 14335-42.
7. Tarun, O.B., M.Y. Eremchev, and S. Roke, *Interaction of Oil and Lipids in Freestanding Lipid Bilayer Membranes Studied with Label-Free High-Throughput Wide-Field Second-Harmonic Microscopy.* Langmuir, 2018. **34**(38): p. 11305-11310.
8. El-Beyrouthy, J., et al., *A new approach for investigating the response of lipid membranes to electrocompression by coupling droplet mechanics and membrane biophysics.* Journal of the Royal Society Interface, 2019. **16**(161): p. 20190652.
9. Grahame, D.C.J.C.r., *The electrical double layer and the theory of electrocapillarity.* 1947. **41**(3): p. 441-501.
10. Yasmann, A. and S. Sukharev, *Properties of diphytanoyl phospholipids at the air–water interface.* Langmuir, 2014. **31**(1): p. 350-357.
11. Najem, J.S., et al., *Activation of bacterial channel MscL in mechanically stimulated droplet interface bilayers.* Sci Rep, 2015. **5**: p. 13726.
12. Taylor, G., et al., *Electrophysiological interrogation of asymmetric droplet interface bilayers reveals surface-bound alamethicin induces lipid flip-flop.* Biochimica et Biophysica Acta (BBA)-Biomembranes, 2018.

# APPENDIX C

# MODEL AND EXPERIMENTAL OBSERVATIONS OF VOLTAGE-MANIPULATED MEMBRANE NETWORKS

## SUPPLEMENTARY INFORMATION [4]

[4] El-Beyrouthy J., Makhoul-Mansour M., Gulle J., Choe J., Wang X., Freeman E. "Model and experimental observations of voltage-manipulated membrane networks"
To be submitted to Soft Matter (2021).

**Resolving droplet geometries**

The droplets forming the model membranes are approximated as spherical caps. Their adhered configuration is resolved through an iterative process as outlined below. Each droplet is assigned an initial volume that remains fixed for all simulated cases in this manuscript; however, cases with osmotic behaviors may be readily implemented in the model. The apparent radius of each droplet is initially defined as the spherical radius based on the droplets volume.

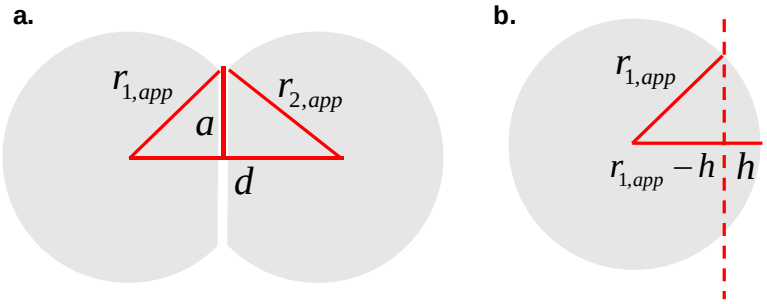


Figure C. 1: a) The dimensions of the membrane formed between two adjacent droplets is determined by their apparent radius and the distance between the two droplets centers. b) At each iteration, the volume of the truncated cap must be added to the apparent droplet volume to recalculate the apparent radii in an iterative fashion until a balanced configuration is reached.

Each droplet retains a set of coordinates for their spherical center. The distance between each center is calculated ($d$) and this value is compared to the sum of the apparent radii ($r_{app}$) for the two droplets. If the droplets overlap as detected by Equation C.1:

$$r_{1,app} + r_{2,app} \geq d \qquad \text{(C.1)},$$

then a membrane is assumed to exist as shown Figure C. 1 (a). The radius of the membrane ($a$) is simply calculated using Pythagorean theorem and the value for the height of the spherical cap ($h$) is isolated as shown in Equation C.2:

$$h = r_{app} - \left( r_{app}^2 - a^2 \right)^{\frac{1}{2}} \tag{C.2}$$

The distance between two droplets ($d$) is then replaced by a summation of the apparent radii and spherical caps for the adhered droplet pair as shown in Equation C.3:

$$d = \left( r_{1,app} - h_1 \right) + \left( r_{2,app} - h_2 \right) \tag{C.3}$$

Equation C.3 and Equation C.2 are combined to produce a solution for the membrane radius ($a$) in Equation (C.4):

$$a = \frac{\left( d + r_{1,app} - r_{2,app} \right)\left( d - r_{1,app} + r_{2,app} \right)\left( -d + r_{1,app} + r_{2,app} \right)\left( d + r_{1,app} + r_{2,app} \right)}{2d} \tag{C.4}$$

However, this is not the final solution. As the droplets overlap, the volume of the spherical cap must be added back into the volume of the main droplet, as shown in Figure C. 1 (b), producing an apparent volume term ($Vol_{app}$) that is the base volume of the droplet plus the summed volume of every spherical cap produced by adhered neighbors.

$$Vol_{app} = Vol + \sum_{i=1}^{\#_{neighbor}} \frac{\pi h_i}{6}\left( 3a_i^2 + h_i^2 \right) \tag{C.5}$$

From this term, the apparent radius ($r_{app}$) must be recalculated, which then influences all previous equations. This is solved in an iterative process by looping over the entire network until the predicted new apparent volumes (Equation C.5) changes by a negligible amount from the previous iteration as defined by the error tolerance (*EPS*) in Equation C.6:

$$\frac{\sum_{i=1}^{\#_{droplet}} Vol_{i,app}^{n+1} - \sum_{i=1}^{\#_{droplet}} Vol_{i,app}^{n}}{\sum_{i=1}^{\#_{droplet}} Vol_{i,app}^{n+1}} \leq EPS \qquad \text{(C.6)}$$

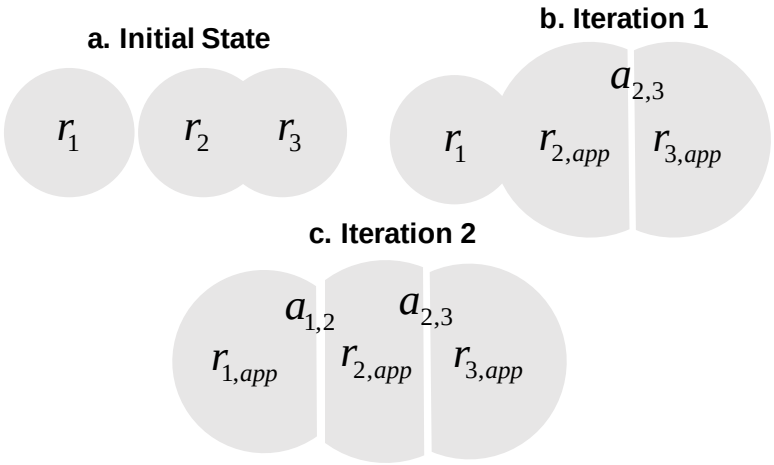


Figure C. 2: a) Droplets are originally printed with overlaps which are detected by comparing the distance between the droplet centers and their summed radii. The formation of membranes generates swelling in the droplets which inflates their apparent radii as exaggerated in (b). b) This leads to the formation of new membranes, which leads to further adjustments in the geometry of the adhered droplet network. c) This is handled through multiple iterations until convergence is reached.

This process is illustrated in 3 steps in Figure C. 2. Droplets are originally placed with overlaps. These overlaps are converted into membrane areas and new apparent radii as summarized in Equations C.1 – C.5. These new apparent radii then produce new overlaps as illustrated Figure C. 2 (b), which has been exaggerated for clarity. This new overlap is then converted into a second adhered interface in the second iteration, which then further influences the apparent volume and radius of the central droplet, and so on. This process is repeated until the geometry converges to a single adhered architecture. The surface for each of the monolayer and bilayer area of each droplet are then adjusted

accordingly, subtracting the area of the spherical caps from the monolayer area and adding the adhered interface to the bilayer area.

### Integration of the solution

Each droplet produces seven differential equations for their position ($x$,$y$,$z$), velocities ($v_x$,$v_y$,$v_z$), and voltage ($V$). However, these differential equations are highly coupled, stiff, and estimated through perturbations. As a result, the differential equations may not be easily expressed, and explicit methods are necessary for the solution. This is handled through an adaptive Dormand-Prince scheme. While this is a conventional approach that is described in detail elsewhere [1], the basics are presented here for convenience. In summary, the integration is handled by a 4$^{th}$ and 5$^{th}$ order approximation of the solution $\left(y_{n+1}, y_{n+1}^{alt}\right)$ [1, 2]:

$$\begin{aligned} y_{n+1} &= y_n + \Delta t \sum_{i=1}^{7} b_{1i} k_i \\ y_{n+1}^{alt} &= y_n + \Delta t \sum_{i=1}^{7} b_{2i} k_i \end{aligned} \tag{C.7}$$

where:

$$
\begin{aligned}
k_1 &= \frac{dy}{dt}\left(t_n, y_n\right) \\
k_2 &= \frac{dy}{dt}\left(t_n + c_2\Delta t, y_n + \Delta t\left(a_{21}k_1\right)\right) \\
k_3 &= \frac{dy}{dt}\left(t_n + c_3\Delta t, y_n + \Delta t\left(a_{31}k_1 + a_{32}k_2\right)\right) \\
k_4 &= \frac{dy}{dt}\left(t_n + c_4\Delta t, y_n + \Delta t\left(a_{41}k_1 + a_{42}k_2 + a_{43}k_3\right)\right) \\
k_5 &= \frac{dy}{dt}\left(t_n + c_5\Delta t, y_n + \Delta t\left(a_{51}k_1 + a_{52}k_2 + a_{53}k_3 + a_{54}k_4\right)\right) \\
k_6 &= \frac{dy}{dt}\left(t_n + c_6\Delta t, y_n + \Delta t\left(a_{61}k_1 + a_{62}k_2 + a_{63}k_3 + a_{64}k_4 + a_{65}k_5\right)\right) \\
k_7 &= \frac{dy}{dt}\left(t_n + c_7\Delta t, y_n + \Delta t\left(a_{71}k_1 + a_{72}k_2 + a_{73}k_3 + a_{74}k_4 + a_{75}k_5 + a_{76}k_6\right)\right)
\end{aligned}
\tag{C.8}
$$

Values for *a*, *b*, and *c* are provided in the Butcher tableau in Equation C.9. Conveniently the solution and alternative solution $\left(y_{n+1}, y_{n+1}^{alt}\right)$ use the same values for $k_{1\text{-}7}$, so the computational penalty for calculating the alternative solution is minimized and only involves varying the coefficients in *b*.

| **c** | **a** | | | | | | |
|---|---|---|---|---|---|---|---|
| 0 | | | | | | | |
| 1/5 | 1/5 | | | | | | |
| 3/10 | 3/40 | 9/40 | | | | | |
| 4/5 | 44/45 | −56/15 | 32/9 | | | | |
| 8/9 | 19372/6561 | −25360/2187 | 64448/6561 | −212/79 | | | |
| 1 | 9017/3168 | −355/33 | 46732/5247 | 49/176 | −5103/18656 | | |
| 1 | 35/384 | 0 | 500/1113 | 125/192 | −2187/6784 | 11/84 | |
| **b** | 35/384 | 0 | 500/1113 | 125/192 | −2187/6784 | 11/84 | 0 |
| | 5179/57600 | 0 | 7571/16695 | 393/640 | −92097/339200 | 187/2100 | 1/40 |

(C.9)

The error is estimated using the difference between the two solutions, where:

$$
Err = \sqrt{\frac{1}{n_{\text{var}}}\sum_{i=1}^{n_{\text{var}}}\left(\frac{y_{n+1} - y_{n+1}^{alt}}{\max\left(\left|\max\left(y_{n+1}, y_n\right)\right|, 10^{-5}\right)}\right)^2}
\tag{C.10}
$$

The timestep for the next solution $\Delta t_{n+1}$ is provided by Equation C.11.

$$\Delta t_{n+1} = \Delta t_n \cdot \min\left(2, \max\left(0.5, 0.85\left(\frac{EPS}{Err}\right)^{\frac{1}{5}}\right)\right) \tag{C.11}$$

This caps the change in the attempted next time step between 0.5 – 2 times the previous timestep dependent on the ratio of the acceptable error *EPS* and measured error *Err*. The integration is then either accepted or rejected before moving to the next interval.

**Executing the script**

The script for simulating the droplet behavior is written in MATLAB. The code is executed from ***mainf.m*** and requires several text files for determining simulation conditions. Text files for each figure presented in the literature are provided in a .zip archive.

The script is designed for execution in a parallel environment and will require the Parallel Computing Toolbox. However, if you do not wish to use this, simply change the `parfor` command when perturbing the droplets to `for`. We've found that the most computationally intensive step is repeatedly calculating the droplet arrangement for estimating the forces, and this approach distributes this task to multiple processors in an attempt to expedite the process where possible. However, this is only recommended when larger collections of droplets are in use since the added communication time between the cores may slow down smaller droplet clusters.

Upon completion, the script will produce a text file ("output.txt") in the same folder. This is a comma-delimited file containing information for the voltage, coordinates, and apparent radius for each droplet at each recorded frame as determined by the input files. If a video is produced, the script will also create a folder (images) with images for

each frame, and subsequently create an avi file ("video.avi") in the same folder as the script from these images.

The most common error observed is when the capacitance matrix [C] becomes singular, often when a droplet is disconnected from the rest. Make sure that the droplets are all properly connected, and that there are no forces present which result in complete separation of the source and ground droplets. Common culprits include excessive voltages or droplets that do not properly overlap initially for establishing membranes.

Values for each of the text file inputs are summarized below. Files include Siminfo, Globalinfo, Dropinfo, and Vinfo.

*Siminfo.txt*

This contains the general information for executing the simulation in the following list: `[tstart, tstop, DT, DTmax perturb nframe EPS writevid]`

| Variable | Description | Units |
|---|---|---|
| tstart | Simulation start time | Seconds |
| tstop | Simulation stop time | Seconds |
| DT | Initial timestep (Equation S11) | seconds |
| Dtmax | Maximum timestep allowed | seconds |
| Perturb | Droplet perturbation value for estimating forces (Equation 6) | meters |
| Nframe | Number of equally spaced points in time for creating videos and plots | #frames |
| EPS | Acceptable error (Equation S11) | NA |
| writevid | 1 to create a video, 0 to omit | NA |

*Globalinfo.txt*

Globalinfo contains the parameters for the simulation that are not droplet-specific in the following list: `[Cspec Gspec mtens btens density density2 damp gamma]`

| Variable | Description | Units |
|---|---|---|
| Cspec | Base membrane capacitance per area ($C_s$, Equation 4, 5) | $F/m^2$ |
| Gspec | Base membrane conductance per area ($G_s$, Equation 4) | S/m |
| mtens | Monolayer tension ($\gamma_m$, Equation 1) | N/m |
| btens | Base bilayer tension ($\gamma_{b,0}$, Equation 1, 5) | N/m |
| Density | Density of the droplet phase | $kg/m^3$ |
| Density2 | Density of the oil phase | $kg/m^3$ |
| damp | Viscous damping term for droplet motion ($\beta$, Equation 7) | Nm/s |
| gamma | Electrocompression coefficient for the membrane ($\gamma$, Equation 2) | $V^{-2}$ |

*Dropinfo.txt*

Dropinfo contains a line of parameters for each droplet in the following format:

[xlocs ylocs zlocs rapps Ks Cls lipid anchors]

Each droplet is assigned a line in this text file. Note that $\mu m$ are used here for droplet positions rather than *m* to expedite entry.

| Variable | Description | Units |
|---|---|---|
| xlocs | Initial x coordinate for the droplet | μm |
| ylocs | Initial y coordinate for the droplet | μm |
| zlocs | Initial z coordinate for the droplet | μm |
| rapps | Initial apparent radius of the droplet (derived from volume, droplets must overlap to establish membranes) | μm |
| Ks | $K^+$ concentration | mM |
| Cls | $Cl^-$ concentration | mM |
| lipid | Offset voltage (relative to DPhPC) due to lipid type | mV |
| anchors | 1 to fix the droplet in space, 0 to allow free motion | NA |

By convention, the first droplet (first line) corresponds to the source voltage, the last droplet corresponds to the ground. This may be modified in the script if desired.

*Vinfo.txt*

This file contains information for the voltage signal stimulating electrowetting between the source and the ground. It contains a line of parameters in the following format: `[Vamp, Vf, Vi]`

| Variable | Description | Units |
|---|---|---|
| Vamp | Amplitude of the voltage signal. | V |
| Vf | Frequency of the voltage signal. | Hz |
| Vi | Flag for the waveform. 1 is sinusoidal, 2 is triangular, and 3 is step. Additional waveforms may be seen/added in the function itself as needed, including experimental traces for comparison purposes. | NA |

## References


1. Dormand, J.R. and P.J. Prince, *A family of embedded Runge-Kutta formulae.* Journal of computational and applied mathematics, 1980. **6**(1): p. 19-26.
2. Butcher, J.C., *Numerical methods for ordinary differential equations*. 2016: John Wiley & Sons.